

**Imaging and Nonlinear Spectroscopy at X-Ray
Wavelengths**

Aviad Schori

Department of Physics

Ph.D. Thesis

Submitted to the Senate of Bar-Ilan University

Ramat-Gan, Israel

April 2018

This work was carried under the supervision of

Dr. Sharon Shwartz

Department of Physics

Bar-Ilan University

Acknowledgments

First, I would like to thank my family for their continued support during my studies.

Second, I would like to thank my supervisor Dr. Sharon Shwartz for his guidance in the frame of this research.

Third, I would like to thank Mr. Denis Borodin for his participation in the synchrotron experiments.

Fourth, I would like to thank Mr. Shimon Filo and Mr. Maxim Isouch from the mechanical workshop and Mr. Valery Jouravsky from the physics department from their help and support with the various technical issues that arose during this research.

Finally, I would like to thank Mrs. Hila Schwartz for her assistance with the many logistic issues that arose during this research.

Abstract

In this Ph.D thesis I present novel approaches in the fields of imaging and nonlinear spectroscopy with X-rays. 1) I describe the first demonstrations of parametrically down-converted X-ray into optical wavelengths. This method can be applied for probing valence charges at the atomic-scale resolution. 2) I describe the first observations of incoherent X-ray ghost imaging with a laboratory source, which advance the possibilities that the high-resolution method of ghost diffraction will be utilized with tabletop X-ray sources. 3) I describe the first observations of incoherent X-ray ghost diffraction with a laboratory source. The extension of the procedure can lead to nanoscale-resolution imaging with laboratory sources and it is therefore useful for a variety of fields of research and industry. 4) I describe the first the experimental observations of ghost imaging with paired X-ray photons, which are generated by parametric down-conversion. The extension of the procedure I present, can be used for the observations of various quantum phenomena at X-ray wavelengths and for damage free imaging.

The first part of my work details my experimental work for the application of ghost imaging and ghost diffraction to the X-ray regime. Ghost imaging and ghost diffraction are imaging techniques, in which the reconstruction of objects is achieved by using the spatial intensity correlations between two beams. One of the beams propagates through the object and it is collected by a single-pixel detector while the second beam does not interact with the object and it is collected by a multi-pixel detector. There are two main types of sources for the spatial correlations. The first type is known as incoherent (or classical) ghost imaging and it relies on introducing spatial intensity fluctuations into the input beam, which is split into two beams with identical intensity fluctuations. The second source is known as quantum ghost imaging and it relies on correlated photon pairs. The ghost imaging technique relies on detection in the near field and reconstruction of the image of the object from the spatial correlations. The detection of ghost diffraction is performed in the far field and the diffraction pattern of the object is measured.

The use of X-ray lenses for imaging is very limited because of their small magnification and aperture size, and hence lensless techniques are widely used in this regime [25-28]. However, despite that nanometer scale resolution has been achieved with coherent X-ray radiation, which is generated by X-ray

free-electron lasers and synchrotron facilities [25], X-ray imaging with low brightness incoherent sources utilize mainly direct absorption measurements and no magnification or small magnification is used. Consequently, although the phase information of objects could enhance the contrast of images, this quantity is almost never measured in systems based on incoherent sources, and the resolution of those systems is not smaller than the pixel size of the camera. Both ghost imaging and ghost diffraction are promising for X-ray imaging since they require neither coherent bright sources nor lenses and can lead to high-resolution and high-contrast imaging techniques that can be implemented with low-cost X-ray sources [29].

Since the source of incoherent ghost imaging and ghost diffraction relies on spatial intensity fluctuations, the image is reconstructed from the instantaneous spatial-second-order intensity correlation function that is measured for various realizations of the intensity fluctuations at the input [1]. The techniques have been studied extensively in the optical regime [1-23] and recently ghost imaging with atoms [24] and temporal ghost imaging [2] have been demonstrated.

Incoherent X-ray ghost imaging and ghost diffraction have been demonstrated experimentally with synchrotron radiation generated by large accelerators [30, 31]. While those important demonstrations advance significantly the extension of ghost imaging and ghost diffraction into the X-ray regime, the effects were not demonstrated with tabletop sources.

In **chapter 4**, I report the first observation of thermal ghost imaging with an X-ray tube laboratory source. I describe experiments that show the possibility to reconstruct the images of slits by using incoherent X-ray sources with very high contrast. These results advance the possibilities that the high-resolution method of ghost diffraction will be utilized with tabletop X-ray sources.

As the detection of ghost diffraction is done in the far field [3,4,10,20,29,31] this method has a clear advantage that the imaging resolution is not limited by the spatial resolution of the detector. The demonstration of this method with a low brilliance X-ray source therefore has significant potential as a method for high resolution imaging with X-ray laboratory sources.

In **chapter 6**, I report the first observation of thermal ghost diffraction with an X-ray tube laboratory source. I present preliminary results of experiments that show the possibility to reconstruct high-resolution images by using incoherent X-ray sources.

Another important source of ghost imaging is correlated photon pairs. This source is implemented in many schemes in the optical regime by utilizing the nonlinear effect of parametric down-conversion. This effect is one of the major sources for the generation of non-classical states of light and has been used to study fundamental quantum phenomena in the optical regime [32-37]. The availability of commercial X-ray detectors with the photon-number-resolving capabilities and with near unity quantum efficiency is appealing for testing concepts of quantum physics and to overcome many of the fundamental challenges of conventional quantum optics at optical wavelengths. Since no other applications of paired X-ray photons of parametric down-conversion have been demonstrated to-date and since many quantum optics schemes are similar to the scheme of ghost imaging with photon pairs its demonstration can greatly advance the field of X-ray quantum optics. Of importance, the properties of the correlations of the paired photons and of X-ray detectors can lead to imaging of objects with very few photons as demonstrated in the optical regime and hence reduce the radiation dose of X-rays.

In **chapter 5**, I present the first observation of X-ray ghost imaging with photon pairs. The results represent the first demonstrated application of photon pairs with parametric down-conversion of X-rays. The results utilize the one-to-one relation between the photon energies and the emission angles and the anti-correlation between the k-vectors of the signal and the idler photons to reconstruct the images of slits with nominally zero background levels. The extension of this procedure can be used for the observation of various quantum phenomena at X-ray wavelengths.

The second part of my work describes the application of the nonlinear process parametric down-conversion of X-rays as a spectroscopy method for valence electrons at the atomic scale. Due to the development of X-ray experimental facilities, namely synchrotrons and X-ray free electron lasers, with high brightness, collimation, and peak intensity, as well as laboratory systems, such as the X-ray diffractometer system, several nonlinear experiments in the X-ray regime have been performed over the last few years [41-49]. Some of these experiments demonstrated the effect of X-ray into extreme ultraviolet parametric down-conversion and its potential as a probe for the optical properties of crystals [41-45]. Despite the potential of probing valence charges at the atomic scale resolution by utilizing X-ray into optical parametric down-conversion, this effect has never been demonstrated before.

In **chapter 7**, I describe the first observation of parametrically down converted X-ray signal photons at photon energies that correspond to idler photons at optical wavelengths. The results of the

presented work advance the development of a spectroscopy method for probing valence-electron charges and the microscopic optical response of crystals at the atomic-scale.

Table of Contents

Contents

Abstract.....	i
1. Introduction	1
1.1 Thesis structure	1
1.2 Motivation and goals	1
1.2.1 Imaging.....	2
1.2.2 Nonlinear spectroscopy	2
1.2.3 Research goals.....	3
1.3 Background.....	4
1.3.1 Thermal Ghost imaging and ghost diffraction.....	4
1.3.2 Quantum Ghost imaging.....	5
1.3.3 Parametric down-conversion.....	6
2. Theoretical models.....	9
2.1 Parametric down conversion.....	10
2.1.1 Parametric down conversion description.....	10
2.1.2 Phase matching	11
2.1.3 The nonlinear current density	12
2.1.4 The coupled wave equations	15
2.1.5 Detector and coincidence counts	17
2.2 Ghost imaging and ghost diffraction	19
2.2.1 General description	19
2.2.2 Coincidence count rates	22
2.2.3 Spatial and temporal properties of incoherent imaging	24
2.2.3.1 Spatial and temporal properties of the source.....	24
2.2.3.2 Spatial and temporal properties of the system.....	24
3. Research methods.....	27
3.1 The experimental system	27
3.1.1 Detection system design.....	27
3.1.2 Positioning system and mechanical design.....	29
3.2 Control and data analysis software.....	30

4. Article: X-ray Thermal Ghost Imaging with a Laboratory Source.....	31
5. Ghost Imaging with Paired X-ray Photons	41
6. X-ray Thermal Ghost Diffraction with a Laboratory Source	61
7. Article: Parametric Down-Conversion of X rays into the Optical Regime.....	73
8. Conclusions and outlook	85
9. Appendixes	89
Appendix A – Coincidence circuit.....	89
Appendix B – Mechanical schematics – Sample holders	91
Appendix C – Software description	93
Appendix C1 – Experiment control software.....	93
Appendix C2 – Analysis software.....	95
Bibliography	97
Hebrew abstract	8

List of Figures

<i>Figure 2.1 - Parametric down conversion energy conservation diagram.</i>	10
<i>Figure 2.2 - Parametric down conversion phase-matching scheme.</i>	12
<i>Figure 2.3 – Ghost imaging general scheme.</i>	20
<i>Figure 2.4 – Ghost diffraction general scheme.</i>	21
<i>Figure 6.1 - Schematic of the ghost diffraction experimental setup.</i>	65
<i>Figure 6.2 – Ghost diffraction results.</i>	69
<i>Figure 6.3 - Normalized spatial correlation of the intensity fluctuations as introduced by the Fe₂O₃ and copy paper diffuser.</i>	70
<i>Figure 6.4 - Spatial properties of the far-field intensity fluctuations as introduced by the diffuser and the beam splitter.</i>	72

List of Acronyms & Abbreviations

APD – Avalanche photo-diode.

BS – Beam splitter.

CCD – Charge-coupled device.

CDI – Coherent diffraction imaging.

CGI – Computational ghost imaging.

DAQ – Data acquisition.

DFG – Difference frequency generation.

EMF – Electromagnetic field.

EUV – Extreme ultraviolet.

F.S. – Full scale.

FWHM – Full width at the half maximum.

GI – Ghost imaging.

GD – Ghost diffraction.

HOPG - Highly ordered pyrolytic graphite.

SDD – Silicon drift detector.

SEM – Scanning electron microscope.

SFG – Sum-frequency generation.

SHG – Second-harmonic generation.

SNR – Signal-to-noise ratio.

PDC – Parametric-down conversion.

SVEA - Slowly variable envelope approximation.

UV – Ultraviolet.

XFEL - X-ray free electron laser.

XRD - X-ray diffractometer.

List of Publications

1. A. Schori and S. Shwartz, "*X-ray ghost imaging with a laboratory source*", Opt. Express **25**, 14822 (2017).
2. A. Schori, C. Bömer, D. Borodin, S. P. Collins, B. Detlefs, M. Moretti Sala, S. Yudovich, and S. Shwartz, "*Parametric Down-Conversion of X Rays into the Optical Regime*", Phys. Rev. Lett. **119**, 253902 (2017).
3. A. Schori, D. Borodin, K. Tamasaku, and S. Shwartz, "*Ghost Imaging with Paired X-ray Photons*", Phys. Rev. Lett., submitted (2018).
4. A. Schori and S. Shwartz, "*A system and method for high-resolution high-contrast X-ray ghost diffraction*", patent application, provisional (2018).

List of conference proceedings

1. S. Shwartz, "*Ghost imaging and ghost diffraction in the X-ray regime*", (FNP-2016, St. Petersburg, 2016).
2. S. Shwartz, "*X-ray ghost imaging and ghost diffraction with a laboratory source*" (PQE-2017, Snowbird, 2017).
3. A. Schori and S. Shwartz, "*Ghost imaging and ghost diffraction with an x-ray tube source*" (Frisno-14, Ein Gedi, 2017).
4. S. Shwartz, "*Parametric Down-Conversion of X Rays into the Optical Regime*" (PQE-2018, Snowbird, 2018).
5. A. Schori, D. Borodin, K. Tamasaku, and S. Shwartz, "*Ghost Imaging with Paired X-ray Photons*" (XOPT 2018, Yokohoma, 2018).
6. A. Schori, C. Bömer, D. Borodin, S. P. Collins, B. Detlefs, M. Moretti Sala, S. Yudovich, and S. Shwartz, "*Parametric-Down Conversion of X-rays into the Optical Regime*" (XOPT 2018, Yokohoma, 2018).
7. A. Schori, C. Bömer, D. Borodin, S. P. Collins, B. Detlefs, M. Moretti Sala, S. Yudovich, and S. Shwartz, "*Parametric-Down Conversion of X-rays into the Optical Regime*" (CLEO 2018, San-Jose, 2018).
8. A. Schori, D. Borodin, K. Tamasaku, and S. Shwartz, "*Ghost Imaging with Paired X-ray Photons*" (CLEO 2018, San-Jose, 2018).

1. Introduction

1.1 Thesis structure

This Ph.D. thesis is divided into nine chapters. **Chapter 2** describes the theoretical models pertinent to the experiments carried out in the research described in the text. The research methods are described in **Chapter 3**. **Chapter 4** describes the first observation of X-ray thermal ghost imaging with a laboratory source. **Chapter 5** describes the first observation of X-ray thermal ghost diffraction with a laboratory source. **Chapter 6** describes the first observation of ghost imaging with paired X-ray photons. **Chapter 7** describes the first observation of parametric-down conversion of X-rays into the optical regime. The conclusions and recommendations for future research are presented in **Chapter 8**. The supplementary description of the electronic, mechanical, and software design, performed in order to achieve the experimental results is shown in **Chapter 9**.

1.2 Motivation and goals

This Ph.D thesis consists the description of experiments that I performed in the fields of imaging and of nonlinear spectroscopy with X-rays. The experiments I describe are thermal ghost imaging a with a laboratory source, thermal ghost diffraction a with a laboratory source, quantum ghost imaging, and parametric-down conversion of X-rays into the optical regime.

1.2.1 Imaging

The main inherent advantages of the X-ray regime are the extremely high spatial resolution (approximately 3 orders of magnitude in comparison to the optical regime) and the high penetration depth of X-rays. The implementation of imaging with a lens system is challenging at X-ray wavelengths, due to the difficulty in the development of optical elements suitable for the X-ray regime, especially lenses. The main imaging techniques that are used in the X-ray regime are therefore lensless imaging techniques [25-27]. The techniques require the use of a high brightness X-ray source and therefore their application is confined to X-ray free electron Lasers and to third generation synchrotron facilities.

The main challenge I chose to address in **chapters 4 and 6** is to overcome one of the fundamental limitations of high resolution imaging with low brilliance X-ray sources. I therefore chose to demonstrate thermal ghost imaging and ghost diffraction, since these are incoherent lensless imaging techniques and are therefore suitable candidates for high-contrast and high-resolution imaging with low brilliance X-ray sources.

The main challenges I chose to address in **chapter 5** are the extension of quantum optics to the X-ray regime and of X-ray imaging with low radiation damage. The extension of the quantum ghost imaging method to the X-ray regime is appealing for testing concepts of quantum physics due to the availability of commercial photon-number-resolving X-ray detectors with near unity quantum efficiency. The extension of the method is advantageous for X-ray imaging with low radiation damage, since it has been demonstrated with optical radiation that is possible to image objects with a small number of photons [7] and due to the low dark noise properties of commercial X-ray detectors.

1.2.2 Nonlinear spectroscopy

The microscopic study of the optical responses of valence electrons can contribute to the study of a variety of fields, such as compounds, chemical bonds, biological samples, and light-matter interactions.

The main methods that are used for the study of the properties of materials rely on either optical radiation sources or on X-ray Bragg diffraction. Methods that rely on sources at optical wavelengths can

provide insight into the interactions of valence electrons. However, since the wavelength of optical radiation is much larger than the interatomic distances of materials, these methods are not suitable for microscopic studies. Resonant inelastic X-ray scattering (RIXS) is another method used to probe the electronic structure of molecules and materials. While this method provides spectral information regarding the valence binding energies it does not provide any spectral information regarding a specific atomic plane. Therefore the Fourier component of the nonlinear susceptibility is not measured and it is not possible to calculate the electron density with the RIXS method. X-ray Bragg diffraction is often used to probe materials at the atomic scale. However, the energy of X-rays is much higher than the binding energies of valence electrons and therefore the X-rays interact mostly with the core electrons. The development of a new spectroscopy tool for the study of valence electrons at the atomic scale is therefore necessary to advance the understanding of materials and fundamental science.

Nonlinear interactions of X-rays and optical radiation can be a powerful tool for the study of chemical bonds and the valence electron density of crystals at the microscopic level and of light-matter interactions with atomic-scale resolution [38-46,48,50]. The atomic-scale resolution is a consequence of the short wavelengths of X-rays, whereas the optical fields interact with the valence electrons.

The development of this spectroscopy tool can be instrumental in the study of the optical properties of materials at the atomic scale resolution and can contribute to the study of molecular processes, electronic components, and solid state physics.

1.2.3 Research goals

The goals of this part of the Ph.D. thesis are therefore to demonstrate experimentally:

- 1) X-ray Thermal ghost imaging with a laboratory source
- 2) X-ray Thermal ghost diffraction with a laboratory source
- 3) X-ray Ghost imaging with photon pairs.
- 4) X-ray into optical parametric down-conversion process with synchrotron radiation.

In the paragraphs below I elaborate on the motivation and background of each of my projects.

1.3 Background

1.3.1 Thermal Ghost imaging and ghost diffraction

An important area of my research, ghost imaging (GI), has been investigated thoroughly at optical wavelengths [1-23]. Ghost imaging utilizes the correlation between two spatially separated beams to retrieve information about an unknown object. In a typical scheme of ghost imaging one of the beams is scattered through the object and it is collected by a single-pixel detector that is positioned close to the object. The second beam does not interact with the object and it is collected by a multi-pixel detector that provides the spatial resolution. The two detectors are positioned equidistant from the source of the spatial correlations. Since the data collected by each detector is insufficient for the imaging of the object, the reconstruction of the image of the object requires the measurement of the correlation between the two detectors.

There are two main schemes that are used for ghost imaging measurements, namely incoherent GI (alternatively thermal GI or classical GI) and quantum GI (or GI with photon pairs).

A second incoherent imaging technique, named ghost diffraction (GD), utilizes the same experimental setup, with the exception that the detection is in the far field. The main difference from the GI technique is that the measured physical quantity is the diffraction pattern. The advantage of this technique is therefore that the imaging resolution is not limited by the spatial resolution of the detector. Since thermal ghost diffraction requires neither coherence nor magnification, it is a promising scheme for the implementation of high-resolution and high-contrast imaging techniques that can be implemented with low-cost X-ray sources. This is in contrast to the two main existing lensless imaging techniques that are used in the X-ray regime, namely Coherent lensless imaging [25] and interferometric based imaging [27] that require the use of a high brightness X-ray source, which is only available using X-ray free electron

Lasers (XFEL's) and 3rd generation Synchrotron facilities, and are therefore not suitable for laboratory sources.

Incoherent GI and GD rely on intensity fluctuations that are introduced into the beam by a moving diffuser [1]. The reconstruction of the object is obtained from statistical measurements of the spatial-second-order intensity correlation function. The methods require neither coherence nor magnification and are therefore promising schemes for the implementation of high-contrast imaging techniques that can be implemented with low-cost X-ray sources. The demonstration of the techniques suggests the possibility to develop high-contrast and high-resolution imaging with tabletop X-ray sources and thus overcome one of the fundamental challenges of X-ray imaging.

Incoherent X-ray ghost imaging and ghost diffraction have been demonstrated experimentally with synchrotron radiation generated by large accelerators [30, 31]. While those important demonstrations advance significantly the extension of ghost imaging and ghost diffraction into the X-ray regime, the effects were not demonstrated with tabletop sources.

1.3.2 Quantum Ghost imaging

The source of quantum GI is different from that of incoherent GI, since it relies on the process of parametric down-conversion (PDC) as a source of correlated (or anti-correlated) photon pairs. This scheme has been used extensively for quantum imaging at optical wavelengths [6,7,21-23]. The correlation between the photon pairs is a consequence of the spatial correlations between the photons and the anti-correlations between their k-vectors.

Since the source of the correlations of thermal GI are classical in nature, they are not suitable for quantum optics measurements. Another important consequence of the statistical nature of thermal sources is that the imaging of objects requires high-photon statistics and they are therefore unsuitable for objects with low radiation damage thresholds.

In contrast to classical GI, the quantum GI scheme has been widely applied at optical wavelengths to study numerous quantum effects [32-37], such as interaction free measurements [32] and sub-shot noise measurements [33], due to the inherent differences between a quantum source and a classical field. Despite

the availability of commercial photon-number-resolving X-ray detectors with near unity quantum efficiency that are appealing for testing concepts of quantum physics and can remedy many fundamental challenges of conventional quantum optics this effect has never been demonstrated at X-ray wavelengths. Moreover, since its observation half a century ago [51] no application of X-ray photon pairs of parametric down-conversion has been reported to date. Since this method has not been demonstrated before with X-rays it is still early to predict its future applications. It seems likely, however, that this method may be useful for imaging of large biological samples, such as insects, where the radiation dose plays an important role.

1.3.3 Parametric down-conversion

Nonlinear processes at optical frequencies, such as parametric down-conversion, sum-frequency generation (SFG), difference-frequency generation (DFG), and second-harmonic generation (SHG), are fundamental nonlinear processes. These processes have been applied at optical wavelengths for scientific research as well as technological applications. In particular, these processes are valuable for the study of the optical responses of materials to electromagnetic fields. The extension of these processes into the X-ray regime offers great potential for material spectroscopy due to the extremely high spatial resolution and the high penetration depth of X-rays as well as the low-noise properties of commercial X-ray detectors.

In processes, such as X-ray/optical sum-frequency generation (SFG) and difference-frequency generation (DFG), X-rays and optical waves are mixed to generate an X-ray wave at a frequency that is equal to the sum or to the difference of the two input frequencies, respectively. The physical mechanism that supports the wave mixing effect can be viewed as an inelastic scattering of the input X-rays from an optically modulated charge density. In typical measurements, the reciprocal lattice vectors of crystals are used to comply with the requirement for phase matching (momentum conservation). Consequently, the measured efficiency is proportional to the absolute square of the Fourier component of the nonlinear susceptibility corresponding to the selected reciprocal lattice vector. This susceptibility is proportional to the Fourier component of the charge density of the valence electrons. Hence the measurements of the

efficiencies for various reciprocal lattice vectors can be used for the reconstruction of the charge density of the valence electrons [41], as is described in detail in **chapter 7** of my work.

Glover et al. reported the first observation of X-ray and optical wave mixing in a diamond crystal by using an X-ray free-electron laser and a Ti-Sapphire laser [46]. However, since the efficiency of SFG scales linearly with the intensity of the optical laser, the observation of the effect requires high optical intensities and it is therefore unsuitable for many materials with a low radiation damage threshold. The requirement for an optical input further prevents the observation of the effect in a variety of opaque materials, such as metals and superconductors.

Another nonlinear effect is parametric down-conversion (PDC). PDC is a second-order nonlinear process, where an incident photon is converted into two photons with lower energies. The process generates a source of entangled photons, with demonstrated applications at optical wavelengths in the fields of quantum optics [34-36] and quantum imaging [6,7,21-23,32,33]. The process is also useful for the microscopic study of the optical properties of materials [40-45].

Parametric down-conversion (PDC) of X-rays into optical wavelengths is based on X-ray and optical nonlinear interactions and can therefore be used to probe the microscopic response of valence electrons with atomic-scale resolution. This process is similar to X-ray/optical difference frequency generation (DFG), but in X-ray into optical PDC the pump photons interact with vacuum fluctuations to generate correlated X-ray and optical photon pairs [38].

The effect has been applied with X-ray and ultraviolet (UV) photon pairs of PDC to study the properties of several crystals [40-45]. Since the efficiency of the effect depends on the properties of the material at all three pertinent wavelengths, the measurements of the X-ray photons emerging from the nonlinear crystal provide information on the UV properties of the sample. It has been further shown that the microscopic linear susceptibility can be evaluated from the measurements of the X-ray PDC intensities for several atomic planes [41].

The observation of PDC of X-rays into optical wavelengths is more challenging and has never been reported. This is because the photon energies of the generated X-ray signal differ by only a few eV from the photon energies of the input beam, and because the Bragg condition is very close to the phase-matching requirement of the PDC process.

2. Theoretical models

This chapter describes the theoretical models applicable to the experiments described in this Ph.D thesis and is comprised of 2 main subjects:

1. The nonlinear process effect of parametric down-conversion is described here, with an emphasis on the X-ray regime. The description includes the coupling between the electromagnetic field (EMF), described by the Maxwell equations and the Newton electrical charge equation of motion, the nonlinear current density, and the coupled wave equations. The process investigated in this work is parametric down-conversion. The theoretical model for this topic is given in **Para 2.1**. Two specific regimes are described here, namely the highly non-degenerate regime with idler photons at optical wavelengths and the weakly non-degenerate regime with signal and idler photon pairs at hard X-ray energies. The theoretical background described in **Para 2.1** is later applied to the experiments of **ghost imaging with paired X-ray photons (Chapter 5)** and **Parametric Down-Conversion of X rays into the Optical Regime (Chapter 7)** of this work.
2. Incoherent (classical) imaging of spatially incoherent light in the X-ray regime. The 2 processes investigated in this work are ghost imaging, where the measurements are done in the near field, and ghost diffraction, where the measurements are done in the far field. The correlations of these processes and the spatial resolution are discussed. The theoretical model for this topic is given in **Para. 2.2** and is later applied to the experiments of **X-ray Thermal Ghost Imaging with a Laboratory Source (Chapter 4)** and **X-ray Ghost Diffraction with a Laboratory Source (Chapter 6)** of this work.

2.1 Parametric down conversion

2.1.1 Parametric down conversion description

Parametric down-conversion (PDC) is a second-order nonlinear process, where an incident photon is converted into two photons with lower energies. The process generates a source of entangled photons, with demonstrated applications at optical wavelengths in the fields of quantum optics [34-36] and quantum imaging [6,7,21-23,32,33,37]. The process is also useful for the microscopic study of the properties of materials [40-45].

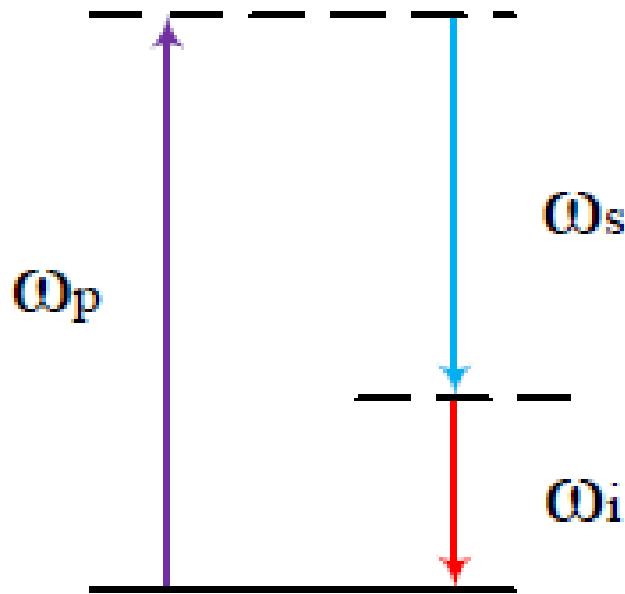


Figure 2.1 - Parametric down conversion energy conservation diagram. The angular frequencies of the pump, the signal, and the idler are denoted as ω_p , ω_s , and ω_i , respectively.

I refer to the incident photon as the pump photon and the two down-converted photons are denoted as the signal and idler photons. Within the frame of this work only X-ray pump and signal photons are taken into consideration. The process preserves energy and momentum (see the **phase matching** description of **Para 2.1.2** for further details). The energy diagram of the PDC process is shown in **Fig. 2.1**. The process is based on the interactions between the incident photon and the vacuum fluctuations in

the nonlinear crystal. Since the vacuum field exists at all the energies in the material all the photon pairs that satisfy energy and momentum (phase matching) conservation can be generated. In the highly non-degenerate regime, we select the idler down-converted photons to be the photons with the lower energy.

2.1.2 Phase matching

Generally speaking, the phase matching condition is achieved when the waves in a nonlinear process interfere constructively, i.e. the efficiency of the process is maximized. This condition for phase matching is achieved when the momentum of the three pertinent waves in the second-order nonlinear process, namely the pump, signal, and idler, is conserved.

I consider the conditions for phase matching of PDC in the X-ray regime. Since X-ray wavelengths are comparable to the distance between the atomic planes, I use the reciprocal lattice vector for phase matching [49,55] as I depict in **Fig 2.2**. I denote θ_p , θ_s , and θ_i as the angles with respect to the atomic planes of the pump, the signal, and the idler, respectively. The k-vectors of the pump, the signal, and the idler are \vec{k}_p , \vec{k}_s , and \vec{k}_i . \vec{G} is the reciprocal lattice vector orthogonal to the atomic planes. The energy conservation implies that $\omega_p = \omega_s + \omega_i$, where I denote ω_p , ω_s , and ω_i as the angular frequencies of the pump, the signal, and the idler, respectively. The phase-matching-condition can be written as $\vec{k}_p + \vec{G} = \vec{k}_s + \vec{k}_i$.

For the case of idler photons at optical wavelengths, the idler k-vector is much smaller than the k-vectors of the pump and the signal. Hence, the phase matching angles of the PDC X-ray signal are very close to the Bragg angle. Consequently, the tail of the elastic scattering is not negligible and the separation of the PDC X-ray signal from the elastic requires narrow filters for energy resolution (namely analyzer crystals) and slits for angular resolution.

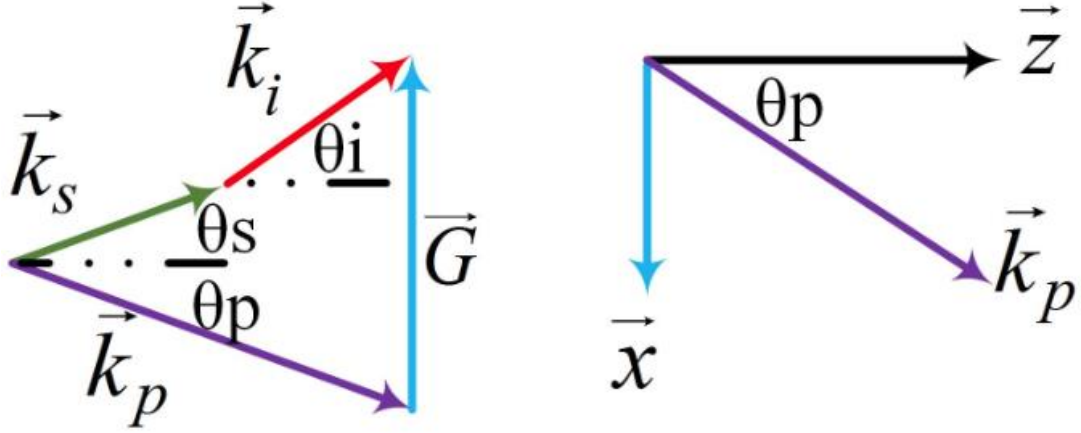


Figure 2.2 - Parametric down conversion phase-matching scheme. The indices p , s , and i represent the pump, signal, and idler, respectively, \vec{G} is the reciprocal lattice vector, and the angles θ_p , θ_s , and θ_i are the angles of the pump, the signal, and the idler, respectively, with respect to the atomic planes.

2.1.3 The nonlinear current density

I start the discussion of the nonlinear current density and of the coupled wave equations of PDC from the equations of motion and continuity for a classical model of a cold collisionless plasma fluid [56], defined as follows:

$$(2.1) \quad \begin{aligned} \frac{\partial \vec{v}}{\partial t} + (\vec{v} \cdot \nabla) \vec{v} + \omega_0^2 \vec{r} &= -\frac{e}{m_e} (\vec{E} + \vec{v} \times \vec{B}) && \text{Equation of motion} \\ \frac{\partial \rho(\vec{r}, t)}{\partial t} + \nabla \cdot (\rho(\vec{r}, t) \vec{v}) &= 0 && \text{Continuity equation} \end{aligned}$$

where \vec{E} , \vec{B} are the electric and magnetic fields, respectively and ω_0 is the plasma resonant frequency; Here, $\vec{v}(\vec{r}, t)$, e , m_e , $\rho(\vec{r}, t)$, and \vec{r} are the field velocity, charge mass, electron density, and position vector of the electrons, respectively. It should be noted that the term $\omega_0^2 \vec{r}$ can be neglected when the energies of both of the generated photons are in the X-ray regime and are therefore far above the plasma resonant frequency of the material.

From the equation of motion and continuity it can be seen that there three terms that contribute to the nonlinearity; The term $e\vec{v} \times \vec{B}$ corresponds to Lorentz force, which is the driving mechanism for the

nonlinearity; The spatial variation of the electron velocity $\nabla\vec{v}$; and the spatial modulation of the charge density that is result of the term $\nabla\cdot(\rho(\vec{r},t)\vec{v})$. Since the photon energies of the incident photons are much larger than the binding energies of material with low-Z atoms such as diamond^a the electrons can be regarded as free particles [54].

A monochromatic plane wave electric field is defined as follows:

$$(2.2) \quad \vec{E}_i(\vec{r},t) = \frac{E_i}{2} \hat{e}_i e^{i(\vec{k}_i \cdot \vec{r} - \omega_i t)} + \frac{E_i^*}{2} \hat{e}_i e^{-i(\vec{k}_i \cdot \vec{r} - \omega_i t)},$$

where \vec{k}_i , ω_i , and \hat{e}_i are the wave vector, angular frequency, and polarization vector of the electric field, respectively.

Using an expansion of $\rho(\vec{r},t)$ and $\vec{v}(\vec{r},t)$ according to the perturbation theory and an expansion of $\rho(\vec{r})$ in a Fourier series^b the Fourier component of the charge density is defined as $\rho_G = \int \rho(\vec{r}) e^{-i\vec{G}\cdot\vec{r}} d\vec{r}$, where $\rho^{(0)}(\vec{r}) = \rho_G e^{i\vec{G}\cdot\vec{r}}$ is the unperturbed charge density.

The general term for the second order nonlinear current density can be described by using the perturbation theory [56]

$$(2.3) \quad \vec{J}_{NL}(\omega_s = \omega_p - \omega_i) = \rho_0 \vec{v}^{(2)}(\omega_p - \omega_i) + \rho^{(1)}(\omega_p) \vec{v}^{*(1)}(\omega_i) + \rho^{*(1)}(\omega_i) \vec{v}^{(1)}(\omega_p),$$

since $r(t) = r^{(0)} + \lambda \cdot r^{(1)}(t) + \lambda^2 \cdot r^{(2)}(t) + \dots$ and therefore $v(r,t) = \lambda v^{(1)}(r,t) + \lambda^2 v^{(2)}(r,t) + \dots$ and since $\rho(r,t) = \rho^{(0)} + \lambda \rho^{(1)}(r,t) + \lambda^2 \rho^{(2)}(r,t) + \dots$ by using the perturbation theory. It is clear from the expression that the nonlinearity can be viewed as scattering of X-rays by the optically induced charge $\rho^{*(1)}(\omega_i)$.

^a Which is used as the nonlinear medium for the experiments I describe later in the text.

^b Valid for ordered crystals such as the diamond sample used in the PDC into optical wavelengths and GI with correlated photon pairs experiments.

The second-order nonlinear current density that we get for PDC^c by approximating the electron velocity \mathbf{v} according to the perturbation theory then becomes:

$$(2.4) \quad \mathbf{J}_s^{NL}(\omega_s = \omega_p - \omega_i) = -E_p E_i^* \left(\frac{\mathbf{e}}{2m_e \omega_p \omega_i} \right)^2 \rho_G e^{i([\vec{k}_p - \vec{k}_i + \vec{G}] \vec{r}^{(0)} - [\omega_p - \omega_i]t)} \times \\ \times \left(\frac{\omega_p \omega_i [\hat{\mathbf{e}}_i \times \vec{k}_i \times \hat{\mathbf{e}}_p - \hat{\mathbf{e}}_p \times \vec{k}_i \times \hat{\mathbf{e}}_i^*]}{\omega_p - \omega_i} + \left[\frac{\omega_p \times \{\hat{\mathbf{e}}_i \times \vec{G}\}}{1 - \beta_i} \hat{\mathbf{e}}_p - \frac{\omega_i \times \{\hat{\mathbf{e}}_p \times \vec{G}\}}{1 - \beta_p} \hat{\mathbf{e}}_i^* \right] \right), \\ \beta_i \triangleq -\frac{e\rho^{(0)}}{\epsilon_0 m_e (\omega_i^2 - \omega_0^2)}$$

where ω_0 is the plasma resonant frequency, ϵ_0 is the free space permittivity, E_p and E_i are the electric field amplitudes of the pump and the idler, respectively, and the polarization vectors of the pump and the idler photons are denoted as $\hat{\mathbf{e}}^{E_p}$ and $\hat{\mathbf{e}}^{E_i}$, respectively. It should be noted that the term ω_0^2 of the expression β_i can be neglected when the resonant frequency ω_i is in the X-ray regime and is therefore far above the plasma resonant frequency of the material.

For the specific case of an X-ray signal photon and an optical idler photon, the nonlinear current density, which is later used in the numerical simulations presented in **Chapter 7**, can be expressed as follows^d [41]:

$$(2.5) \quad \mathbf{J}_s^{NL}(\omega_s = \omega_p + \omega_i) = \frac{E_p E_i^* i e \chi_G^{(1)}(\omega_i) G \epsilon_0 \sin \theta_B \cos 2\theta_B}{2m_e \omega_s},$$

where $\chi_G^{(1)}$ is the linear susceptibility and θ_B is the Bragg angle.

^c Although at this point this is still the general form of a difference frequency generation (DFG).

^d Where we assume that there are no two or more resonances that are in close proximity.

For the specific case of X-ray signal and idler photons^e at a scattering angle near 90°, the nonlinear current density envelope, which is later used in the numerical simulations presented in **Chapter 5**, can be expressed as follows [48]:

$$(2.6) \quad J_s^{\text{NL}}(\omega_p = \omega_s + \omega_i) = \frac{e\rho_G E_p E_i^*}{2m_e^2 \omega_p^2 \omega_i} (\vec{G} \cdot \hat{e}_i) (\hat{e}_p \cdot \hat{e}_s),$$

where \hat{e}^E is the polarization vector of the signal.

2.1.4 The coupled wave equations

The PDC process can be described by the coupled wave equations. I describe the coupled wave equations in a Laue geometry. Under the assumptions of the undepleted pump approximation, a lossless medium, and the slowly varying envelope approximation (SVEA), the coupled wave equations in the frequency domain can be described as [48, 49]

$$(2.7) \quad \begin{aligned} \frac{\partial a_s}{\partial z} + \frac{\alpha_s}{\cos \theta_s} a_s &= \kappa a_i^+ \exp[i\Delta k_z z] + \sqrt{\frac{2\alpha_s}{\cos \theta_s}} f_s \\ \frac{\partial a_i^+}{\partial z} + \frac{\alpha_s}{\cos \theta_i} a_i^+ &= \kappa^* a_s \exp[-i\Delta k_z z] + \sqrt{\frac{2\alpha_i}{\cos \theta_i}} f_i^+ \end{aligned},$$

where a_s and a_i are the signal and idler annihilation operators, respectively,

$\Delta k_z = k_p \cos \theta_p - k_s \cos \theta_s - k_i \cos \theta_i$ is the phase mismatch, and $\kappa = \frac{(2\hbar \eta_p \eta_s \eta_i \omega_p \omega_s \omega_i)^{\frac{1}{2}} J_s^{\text{NL}}}{2\omega_s E_i^* \sqrt{\cos \theta_s \cos \theta_i}}$ is the nonlinear

interaction coefficient. We denote η_p , η_s , and η_i as the impedances at the pump, the signal, and the idler frequencies, \hbar is the reduced Planck constant, and J_s^{NL} is the nonlinear current density. Here α_s and α_i represent the signal and idler absorption coefficients, respectively, and f_s and f_i are the signal and idler Langevin noise operators, respectively. The Langevin method is used to describe quantum systems with inherent losses [68]. As a consequence of the inclusion of the Langevin operators on the signal, idler, and

^e Where both photons are far from resonance.

coincidence count rate depend on the absorption length rather than the crystal length for a sufficiently long crystal.

The time-space signal and idler operators are related to their frequency domain counterparts by

$$(2.8) \quad \begin{aligned} a_s(z, \mathbf{r}, t) &= \int_0^\infty \int_{-\infty}^\infty a_s(z, \mathbf{q}, \omega) [-i(\mathbf{q} \cdot \mathbf{r} - \omega t)] d\mathbf{q} d\omega \\ a_i(z, \mathbf{r}, t) &= \int_0^\infty \int_{-\infty}^\infty a_i(z, \mathbf{q}, \omega) [-i(\mathbf{q} \cdot \mathbf{r} - \omega t)] d\mathbf{q} d\omega \end{aligned} ,$$

where $\mathbf{r} = (x, y)$.

The commutation relations for the signal and idler operators are

$$(2.9) \quad [a_j(z_1, \mathbf{q}_1, \omega_1), a_k^\dagger(z_2, \mathbf{q}_2, \omega_2)] = \frac{1}{(2\pi)^3} \delta(z_1 - z_2) \delta(\mathbf{q}_1 - \mathbf{q}_2) \delta(\omega_1 - \omega_2),$$

here $\mathbf{q}_j = (k_{jx}, k_{jy})$, where k_{jx} and k_{jy} represent the k wave-vector components parallel to the surfaces of the crystal. Of importance, the requirement of these operators to preserve the commutation relations for the signal and idler operators is a consequence of the interaction with the vacuum fluctuations in the crystal.

The commutation relations for the signal and idler Langevin noise operators are

$$(2.10) \quad [f_j(z_1, \mathbf{q}_1, \omega_1), f_k^\dagger(z_2, \mathbf{q}_2, \omega_2)] = \frac{1}{(2\pi)^3} \delta_{j,k} \delta(z_1 - z_2) \delta(\mathbf{q}_1 - \mathbf{q}_2) \delta(\omega_1 - \omega_2),$$

Since the Langevin terms are introduced to describe losses in quantum systems, they can be neglected in special cases where the absorption is negligible. Therefore, for the specific case of idler photons at optical wavelengths, under the assumption of a lossless medium, the absorption and Langevin terms of **Eq. 2.7** can be neglected, and the coupled wave equations are reduced to the following form [49]

$$(2.11) \quad \begin{aligned} \frac{\partial a_s}{\partial z} &= -\kappa a_i^+ \exp[j\Delta k_z z] \\ \frac{\partial a_i^+}{\partial z} &= -\kappa^* a_s \exp[-j\Delta k_z z] \end{aligned} .$$

2.1.5 Detector and coincidence counts

For single photon counting detectors, the counts of a detector are defined as follows:

$$(2.12) \quad R_i = A \langle a_i^\dagger(t_i) a_i(t_i) \rangle,$$

where A is the effective area of the nonlinear media that is illuminated by the pump beam.

The signal count rate, for the specific case of idler photons at optical wavelengths, where the coupled wave equations of **Eq. 2.11** can be solved analytically, is given by:

$$(2.13) \quad R_s = \iint \kappa^2 \frac{\cos\theta_s}{(2\pi)^3} \frac{\omega_s^2}{c^2} \frac{\sin^2\left(\frac{1}{2}\Delta k_z z\right)}{\left(\frac{1}{2}\Delta k_z z\right)^2} d\Omega d\omega_s,$$

where c is the speed of light in vacuum. The signal count rate is calculated numerically, where the integration is taken over the solid angle of the detector and the bandwidth of the detection system. We note that the acceptance angle of the detector restricts the bandwidth due to the one to one relation between the angle of propagation and the wavelength of the generated X-ray signal, which is imposed by the requirement for exact phase matching in the directions parallel to the surface of the crystal.

For single photon counting detectors, the coincidence count rate is defined as follows:

$$(2.14) \quad R_c = A \langle a_s^\dagger(t_s) a_i^\dagger(t_i) a_i(t_i) a_s(t_s) \rangle,$$

where t_s and t_i are the respective photon arrival times at the signal and idler detectors and A is the effective spot size of the pump at the nonlinear media plane. The coincidence count rate is calculated numerically, where the integration is taken over the solid angle of the detectors and the bandwidth of the detection system.

The physical meaning of each coincidence count is the detection of a photon pair within a small time window, thus drastically reducing the experimental noise. The time window length, which we denote as τ , ranges from a few nsec to a few hundreds of nsec, due to the different optical paths of the experimental

setup and the limitations of the detection system. These limitations are influenced mainly by the uncertainty in the ionization time of the charge carriers in the detector. For an input pump with a uniform time structure^f and uniformly distributed noise signals, which are denoted as $R_{s\text{-noise}}$ and $R_{i\text{-noise}}$ and are detected by the signal and idler detectors, respectively, the accidental coincidence count rate can be estimated as $R_{s\text{-noise}}R_{i\text{-noise}}\tau$. The PDC coincidence count rate, however, remains unchanged provided that the selected time window is larger than the overall time resolution of the detection system, and that the degree of saturation of the detectors (i.e. the rates of events, where two or more photons are detected in a time scale that is smaller than the pulse duration that is generated by a detector after a single detection event) in either of the detectors is well below the PDC coincidence count rate.

The coincidence count rate in the presence of an aperture (for the ghost imaging measurements that are described in **Chapter 5**. The concept of ghost imaging is described in **Para. 2.2**) can be considered as follows:

$$(2.15) \quad R_c = A(2\pi)^6 \iiint \langle a_i^+(\omega_1, k_{x1}, k_{y1}) a_s^+(\omega_2, k_{x2}, k_{y2}) a_s(\omega_2, k_{x2}, k_{y2}) a_i(\omega_1, k_{x1}, k_{y1}) \rangle x \\ x |H(\omega_1)|^2 |H(\omega_2)|^2 |H(k_{x1})|^2 |H(k_{x2})|^2 |H(k_{y1})|^2 |H(k_{y2})|^2 d\omega_1 d\omega_2 dk_{x1} dk_{x2} dk_{y1} dk_{y2},$$

where 1 and 2 are the indices the two detectors, respectively, and H is the window function of the object.

Of importance, in the experiments described in **Chapter 5** an energy filter is also used by rejecting coincidence events where the sum of the energies of the photon pairs does not equal the pump energy within the bandwidth of the detection system. As a consequence the majority of the accidental coincidence counts are filtered out. This filter is essential since the majority of the accidental coincidence counts are originated from residual elastic scattering (the tail of the Bragg diffraction) and Compton scattering and their photon energies are therefore mostly above the photon energies of PDC that we expect to measure in the experiments described in **Chapter 5**.

^f E.g. a quasi-DC source such as an XRD or a synchrotron\XFEL with a uniform pulse period.

2.2 Ghost imaging and ghost diffraction

2.2.1 General description

Ghost imaging (GI) is a technique for obtaining an image of an object by measuring the intensity distribution of the object. The main imaging technique utilizes the correlation (or coincidences of signal-idler photon pairs) between a single-pixel test detector in view of the object and a multi-pixel detector reference detector with spatial resolution as shown in **Fig. 2.3**. It is important to note that the reference detector is blind to the object^g, i.e. it does not measure the intensity projected from the object.

The two main ghost imaging techniques are:

1. Quantum GI – Entangled photon pairs, e.g. photons that created from the PDC process (as described in the PDC background in **Para. 2.1**).
2. Thermal GI – A classical incoherent source. The source is implemented by introducing intensity fluctuations into the beam by utilizing a moving diffuser. The incoherent output of the diffuser is then split into two beams with identical intensity fluctuations.

Due to the low nonlinear susceptibility in the X-ray regime, the lack of coherent laboratory X-ray sources, and the experimental noises in the former technique (Bragg diffraction, Compton, and Thomson scattering), it is preferable to employ the latter technique with laboratory sources. In order to optimize the performance, we will therefore work in the high-photon-flux regime [6]. The ghost imaging technique is only able to reconstruct the image of the object directly, without the need for phase reconstruction. In addition, measurements are performed in near-field conditions, and are therefore limited by the spatial resolution of the reference detector.

^g This technique is therefore useful, where it not easy to act on the test arm, or when stealthy detection is necessary.

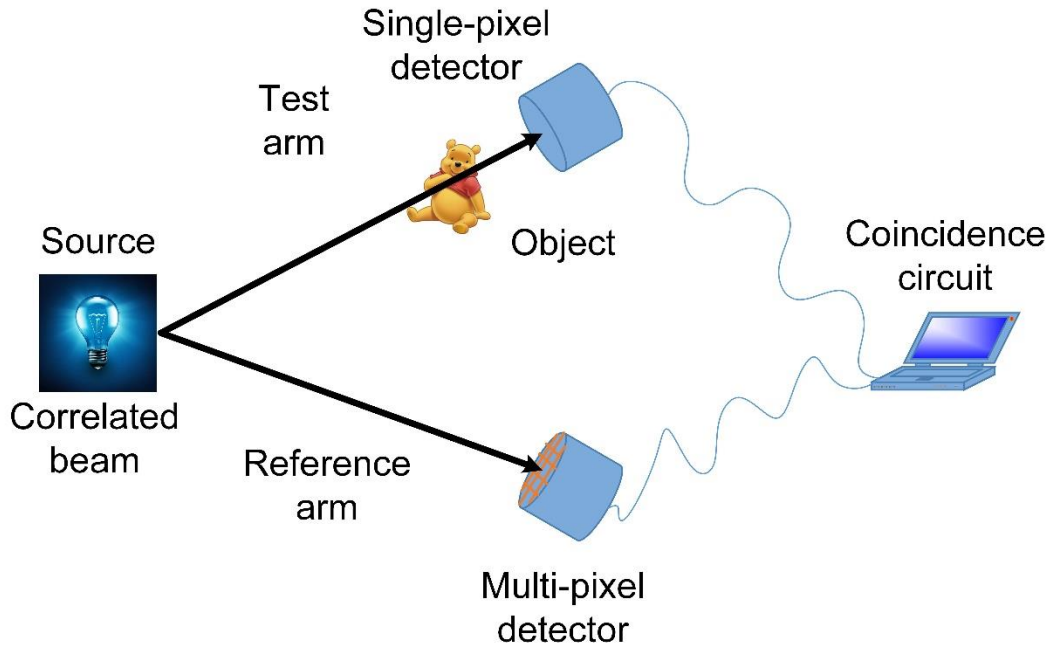


Figure 2.3 – Ghost imaging general scheme.

Incoherent GI relies on intensity fluctuations that are introduced into the beam by a moving diffuser [1]. The reconstruction of the object is obtained from statistical measurements of the spatial-second-order intensity correlation function. Since this scheme does not require neither coherence nor lenses it has the potential to enhance the imaging capabilities of laboratory sources and hence advance scientific fields such as biology, physics, and engineering, as well as high spatial resolution applications for industrial, medical, and military purposes.

The source of quantum GI is different from that of incoherent GI since it relies on the process of parametric down-conversion (PDC) as a source of correlated (or anti-correlated) photon pairs. The correlation between the photon pairs is a consequence of the spatial correlations between the photons and the anti-correlations between their k-vectors. Due to the availability of commercial photon-number-resolving X-ray detectors with near unity quantum efficiency this scheme is appealing for testing concepts of quantum physics and can remedy many fundamental challenges of conventional quantum optics.

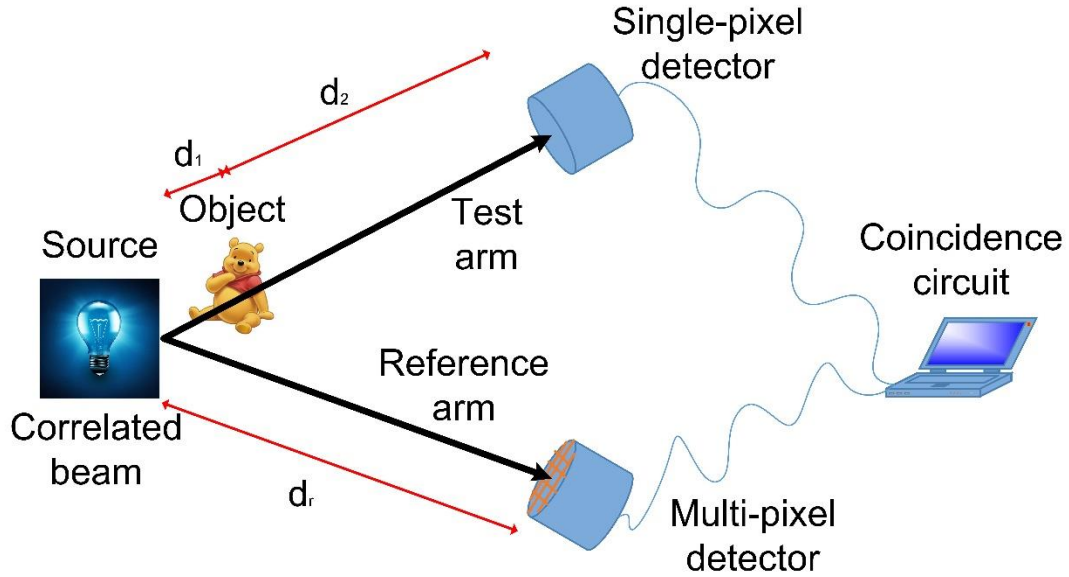


Figure 2.4 – Ghost diffraction general scheme.

Ghost diffraction (GD), however, reconstructs the image from far-field measurements, and is therefore not limited by spatial resolution of the reference detector. This is possible since each spot of the interference pattern at the detector plane in the far field matches a smaller spot at the object plane. The detector is therefore positioned close to the beam splitter as shown in the ghost diffraction scheme in **Fig. 2.4**.

The application of incoherent GI to X-ray wavelengths has several inherent differences compared to the optical regime. The first difference is the X-ray source. The majority of X-ray sources are either laboratory sources or synchrotrons that are partially coherent sources. While it is possible to increase coherence length by closing the slits at the input for widths of a few microns with synchrotrons this is not possible for laboratory sources due to the low flux. This is in contrast to the optical regime where the input source is usually a coherent laser. Other differences are a consequence of the extremely short wavelengths of X-rays that result in a refractive index that is very close to unity. The use of fundamental optical components, namely lenses, refractive-index based beam splitters, and spatial light modulators, is therefore either very limited or not possible at X-ray wavelengths. In the absence of lenses, the magnification of the GD diffraction pattern is therefore determined only by the distance between the object

and the multi-pixel detector. The X-ray beam splitter is realized by using Bragg diffraction from a wideband crystal.

Of importance, it is assumed for simplicity that the input source before the diffuser is coherent throughout the text. While this assumption is not strictly accurate for X-ray laboratory and synchrotron sources (these sources are partially coherent with a coherence length on the order of a few microns) the model we describe in **Para. 2.2.2** can provide a rough estimate to the diffraction patterns we expect to measure and is sufficient for the purpose of a proof of concept. This assumption is valid, since the diffuser introduces amplitude fluctuations and not phase fluctuations and since the diffraction angle is small.

2.2.2 Coincidence count rates

The coincidence count rate for a reference (which is denoted as ref in the equations) and a test detector is [29]^h:

$$(2.16) \quad \begin{aligned} \text{Coincidence count rate} &= \langle E_{\text{ref}}^*(\mathbf{r}_{\text{ref}}) E_{\text{test}}^*(\mathbf{r}_{\text{test}}) E_{\text{ref}}(\mathbf{r}_{\text{ref}}) E_{\text{test}}(\mathbf{r}_{\text{test}}) \rangle = \\ &= \langle I_{\text{test}}(\mathbf{r}_{\text{test}}) \rangle \langle I_{\text{ref}}(\mathbf{r}_{\text{ref}}) \rangle + |rt| \left| \iint G^{(1,1)}(\mathbf{r}_1, \mathbf{r}_2') h_{\text{ref}}(\mathbf{r}_1, \mathbf{r}_{\text{ref}}) h_{\text{test}}^*(\mathbf{r}_2', \mathbf{r}_{\text{test}}) d\mathbf{r}_1 d\mathbf{r}_2' \right|^2, \end{aligned}$$

where $\langle \dots \rangle$ represents a time average, $I_{\text{ref, test}}$, $E_{\text{ref, test}}$, and $h_{\text{ref, test}}$ are respectively the intensities, the field amplitudes, and the impulse responses at the reference and test detectors, and r and t are the respective reflection and transmission amplitudes of the beam splitter. $G^{(1,1)}(\mathbf{r}_1, \mathbf{r}_2')$ is the first-order spatial correlation function between the reference and test beams, which I defineⁱ as $G^{(1,1)}(\mathbf{r}_1, \mathbf{r}_2') = I(\mathbf{r}_1) e^{-0.5 \left(\frac{\mathbf{r}_1 - \mathbf{r}_2'}{r_{\text{coh}}} \right)^2}$.

Here, r_{coh} denotes the spatial correlation of the source.

^h Valid under the following assumptions:

- a. The source is monochromatic and therefore there is no time dependency.
- b. The cross-section of the source is much larger than the object and all the optical elements and therefore there is translational invariance in the transverse plane.

ⁱ For a fully spatially incoherent beam the correlation can be described as a delta function. We assume that the input beam is uniform.

The correlation function for ghost imaging and ghost diffraction is known to be [97]:

$$(2.17) \quad G^{(2,2)}(\mathbf{r}_{\text{ref}}, \mathbf{r}_{\text{test}}) = \frac{\langle I_{\text{ref}}(\mathbf{r}_{\text{ref}}) I_{\text{test}}(\mathbf{r}_{\text{test}}) \rangle - \langle I_{\text{ref}}(\mathbf{r}_{\text{ref}}) \rangle \langle I_{\text{test}}(\mathbf{r}_{\text{test}}) \rangle}{\langle I_{\text{ref}}(\mathbf{r}_{\text{ref}}) \rangle \langle I_{\text{test}}(\mathbf{r}_{\text{test}}) \rangle},$$

where $\langle I_{\text{ref}}(\mathbf{r}_{\text{ref}}) I_{\text{test}}(\mathbf{r}_{\text{test}}) \rangle$ is equivalent to the coincidence counts expression of **Eq. 2.16**.

The term $\langle I_{\text{ref}}(\mathbf{r}_{\text{ref}}) \rangle \langle I_{\text{test}}(\mathbf{r}_{\text{test}}) \rangle$ is subtracted from the coincidence counts, since it contains no information regarding the image.

The impulse responses at the reference and test detectors can be described by taking into account Fresnel free space propagation and the transmission of the object [29]:

$$(2.18) \quad \begin{aligned} h_{\text{ref}}(\mathbf{r}_1, \mathbf{r}_{\text{ref}}) &= \frac{e^{-ikd_r}}{i\lambda d_r} e^{-\frac{i\pi}{\lambda d_r}(\mathbf{r}_1 - \mathbf{r}_{\text{ref}})^2} \\ h_{\text{test}}(\mathbf{r}_2, \mathbf{r}_{\text{test}}) &= \int d\mathbf{r}' \frac{e^{-ikd_1}}{i\lambda d_1} e^{-\frac{i\pi}{\lambda d_1}(\mathbf{r}_2 - \mathbf{r}')^2} t(\mathbf{r}') \frac{e^{-ikd_2}}{i\lambda d_2} e^{-\frac{i\pi}{\lambda d_2}(\mathbf{r}_{\text{test}} - \mathbf{r}')^2}, \end{aligned}$$

where k and λ are the wave vector and the wavelength of the source, respectively, and $t(\mathbf{r}')$ is the transmission of the object. The distances d_1 , d_2 , and d_r , are the distance of the object from the beam splitter, the distance of the object from the test detector, and the distance of the reference detector from the beam splitter, as shown in **Fig. 2.4**. We assume that the reference and test detectors are equidistant from the beam splitter so that $d_1 + d_2 = d_r$ and that in the ghost imaging case $d_2 \approx 0$.

In the specific case of a fully spatially incoherent source at the output of the diffuser, the correlation function of a **ghost diffraction** measurement as shown by J. Cheng and S. Han [29,31] is:

$$(2.19) \quad G^{(2,2)}(\mathbf{r}_{\text{ref}}, \mathbf{r}_{\text{test}}) = \frac{I^2(\mathbf{r}_1)}{\lambda^4 d_2^4} \left| \mathcal{T} \left(\frac{2\pi(\mathbf{r}_{\text{test}} - \mathbf{r}_{\text{ref}})}{\lambda d_2} \right) \right|,$$

where $\mathcal{T}(q)$ is the Fourier transform of $t(\mathbf{r}')$. It is therefore necessary that the test detector area is sufficiently small so that only a single diffraction pattern corresponding to a position of \mathbf{r}_{test} is recorded. Moreover, if the test detector used has spatial resolution than multiple diffraction patterns can be recorded simultaneously, thus reducing the required measurement time and improving the resolution of the image.

It should be noted that while each such measurement corresponds to the correlation function of a ghost diffraction measurement the sum of these diffraction patterns cannot be regarded as "ghost" diffraction, since the spatial information of the test detector is used.

2.2.3 Spatial and temporal properties of incoherent imaging

2.2.3.1 Spatial and temporal properties of the source

The main properties of the incoherent source can be described by the spatial and temporal coherence of the source and the angular acceptance (bandwidth) of the beam splitter. The spatial coherence of the source limits the spatial resolution that can be achieved with the system. The temporal coherence of the source determines the necessary time resolution of the detection system.

The spatial resolution, or coherence length, of the source (after the diffuser) is defined as the inverse of the bandwidth of the correlation function. Thus, lowering the coherence length improves the spatial resolution of the image, although it reduces the visibility of the image.

2.2.3.2 Spatial and temporal properties of the system

In GI the resolution is not only limited by the spatial resolution of the diffuser but also by the spatial resolution of the reference detector. In GD the spatial resolution of the detector does not limit the resolution of the diffraction pattern. The GD resolution is determined by the size of the diffraction pattern, which I denote as F.S. (full scale), and is known to be [75] $\frac{\lambda z}{\text{F.S.}}$.

There are three major parameters that influence the GD spatial resolution: 1) The size of the diffraction pattern described above. 2) The spatial resolution of the multi-pixel detector. 3) The field of view of the multi-pixel detector. The spatial resolution of the multi-pixel detector is required to be sufficiently small to resolve the features on the diffraction pattern (i.e. Nyquist sampling conditions). The

field of view of the multi-pixel detector limits the effective size of the recorded diffraction pattern (although in principle the multi-pixel detector can be moved and the GD measurements repeated for the different positions of the detector). Since the GD resolution is proportional to the distance of the object from the multi-pixel detector, the GD resolution can be improved by positioning the multi-pixel detector closer to the object (under the assumption that the diffraction pattern is limited by the field of view of the multi-pixel detector). This assumption, however, is only valid provided that the features on the diffraction pattern are still resolvable by the multi-pixel detector. If the multi-pixel detector, however, is positioned further from the object additional features can be resolved on the diffraction pattern, but since the diffraction pattern is wider the necessary field of view to measure the diffraction pattern and the photon statistics (neglecting absorption) required to achieve the same contrast will increase linearly.

It should be noted that the ghost imaging and ghost diffraction formalisms are only valid as long as the detector integration time t_{det} is shorter than the temporal diffuser coherence $t_{\text{coh_diff}}$. The X-ray diffractometer (XRD) source without a diffuser has a coherence time of^j:

$$(2.20) \quad t_{\text{coh}_s} = \frac{\lambda^2}{c\Delta\lambda} = \frac{\lambda}{c\Delta E/E} = \frac{1.54056 \times 10^{-10}}{(299,792,458) \times 1 \times 10^{-4}} = 5.1388 \times 10^{-15} \text{ sec}.$$

Here c and $\Delta\lambda$ are the speed of light in vacuum and the spectral linewidth of the source, respectively. It should be noted that the coherence time is much shorter than t_{det} for existing detectors (at least 10^{-9} sec). Therefore, the fluctuations of the source are averaged out and the detector is only sensitive to fluctuations introduced by the diffuser for sufficiently long averaging times, when the intensity fluctuations of the diffuser become dominant.

Since the acceptance angle of the beam splitter can limit the resolution of the system by filtering out intensity fluctuations the main requirement is that it is much larger than the angular spread of the intensity fluctuations that the diffuser introduces. This is because the beam splitter that I use is based on Bragg diffraction, which is angular dependent. Thus, if the acceptance angle of the beam splitter is not sufficiently large, the reflected beam contains only intensity fluctuations that are within the angular acceptance of the beam splitter, while the transmitted beam contains the entire range of the fluctuations.

^j Using a monochromator.

Consequently, the intensity fluctuations of the two beams are not identical and the visibility is highly reduced.

3. Research methods

This chapter describes the experimental design. The design I developed and present is not limited to the experiments described in this Ph.D thesis but also to the various experiments performed by other members of our group [43, 48, 57-60]. The scope of this chapter includes the electronics, mechanics, and software. The specific experimental systems of the experiments that are included in this Ph.D thesis are described in the proceeding chapters.

The experiments described in the Ph.D. thesis were performed either with synchrotron radiation or with an X-ray tube. In contrast to standard synchrotron experiments that rely on the existing design of the beamline, the synchrotron experiments that are described in this Ph.D thesis required special modification of the synchrotron beam line and the design of the detection system and software. The experiments that were performed with an X-ray tube required the use of detection system properties and of positioning control capabilities that are not included in the design of the X-ray tube. These requirements, as well as the strict space considerations due to the compact size of the X-ray tube enclosure, necessitated the characterization of a positioning and detection system with software control and the mechanical design of the experiments.

3.1 The experimental system

3.1.1 Detection system design

All the detectors that were used in the experiments I describe are single-photon counters due to the low-noise requirements of the experiments. The selections of X-ray detectors and of the data acquisition system depend on the specific requirements of each experiment. Three specific types of detectors were used for the experiments described in the Ph.D. thesis.

The first detector type is an avalanche photo-diode (APD) detector chosen due to its low dark count rate (~1 count per minute according to experimental measurements) and its short response time. In an APD the free electrons that are generated by the photoelectric effect are accelerated due to a high voltage

bias. As a result of the high electron velocities bound electrons are freed. Each electron frees additional electrons and consequently avalanche multiplication occurs. The short response times result in a time resolution on the order of a nanosecond and in a capability to perform single-photon measurements at rates of^k up to 10^7 counts/sec. Hence, these detectors are suitable for single-photon measurements at high count rates and for time coincidence measurements. This detector type was therefore used in the experiments presented in the "X-ray Thermal Ghost Imaging with a Laboratory Source", the "X-ray Thermal Ghost Diffraction with a Laboratory Source", and the "Parametric Down-Conversion of X rays into the Optical Regime" experiments in **Chapters 4, 6, and 7**.

The second detector type is a silicon drift detector (SDD) that relies on the ionization of electrons by the incoming photons. Since the binding energy of Si valence electrons is on the order of 1 eV and since the photon energies of X-rays are on the order of several keV to tens of keV the dark count rate of this detector is extremely low (~3 counts per hour according to experimental measurements) and it is possible to determine the incoming photon energies from the electron current (125 eV resolution @ 6 keV according to the vendor specifications). Hence, these detectors are suitable for single-photon measurements at very low count rates and for coincidence measurements that require the use of the incoming photon energies. This detector type was therefore used in the "Ghost Imaging with Paired X-ray Photons" experiment in **Chapter 5**.

The third detector type is a charge-coupled device (CCD). This detector is composed of a scintillator screen that converts the incident X-ray beam into optical wavelengths by means of fluorescence and of a CCD array that detects the optical photons that are generated by the fluorescence process. Since the photon energy of X-rays is larger by three orders of magnitude than the photon energy of the optical photons, each X-ray photon is converted into many optical photons and hence the detector is able to resolve single X-ray photons (the average standard deviation of the dark count rate is ~1/3 ph/pixel/frame according to experimental measurements). This detector is therefore a suitable candidate for thermal ghost imaging and ghost diffraction experiments. The images are read from the device via an Ethernet card. This detector type was therefore used in the "X-ray Thermal Ghost Diffraction with a Laboratory Source" experiments presented in **Chapter 6**.

^k According to the vendor specification.

Since the electrical outputs of APD and SDD devices are pulses, data acquisition is performed for most applications by counting the pulses by use of a NI DAQ board (for example the experiments described in the "X-ray Thermal Ghost Imaging with a Laboratory Source" experiment in **Chapter 4** and in the "X-ray Thermal Ghost Diffraction with a Laboratory Source" experiment in **Chapter 6**). In instances where time coincidence measurements are required a time coincidence card (see **Appendix A** for details) or a time correlation card are used. Since the analog signals of X-ray detectors are proportional to the detected photon energies, it is also possible to resolve the photon energies by recording these signals with a digitizer, as described in the "Ghost Imaging with Paired X-ray Photons" experiment in **Chapter 5** of this work.

Since the dark count rates of all the detectors I describe above is small, the experimental error is dominated by the statistical nature of the measurements (Poisson statistics is assumed, i.e. that the error of the count rate measurement is \sqrt{N}/T_{acq} , where N is the number of detector counts and T_{acq} is the acquisition time in seconds). Hence, averaging over the detector measurements and over the coincidence counts is necessary to reduce the experimental errors in the measurements.

Pulse amplifiers, attenuators, high bandwidth transformers, and cables suitable for nano-second pulse signals were applied to minimize distortion and attenuation of the signals due to the long distances between the detectors and the data acquisition systems at synchrotron facilities (up to 20 meters) and due to the time resolution requirements for the coincidence measurements.

The spatial and frequency filters that were necessary for reducing the experimental noises (Bragg diffraction, Thomson scattering, Compton Scattering, and X-ray fluorescence) for measurements of the PDC effect are described in the "Ghost Imaging with Paired X-ray Photons" experiment in **Chapter 5** and in the "Parametric Down-Conversion of X rays into the Optical Regime" experiment in **Chapter 7**.

3.1.2 Positioning system and mechanical design

The experimental setups for the ghost imaging and ghost diffraction experiments (see **Chapter 4-6**) required the use motorized stages for alignment purposes and for the experimental measurements. Specifically, the thermal ghost imaging and ghost diffraction experiments described in **Chapter 4** and

Chapter 6 required control of the position of the diffuser via a rotation stage, alignment of the detectors and of the objects with translation stages and with rotation stages, and the control of the position of the reference slit (to achieve spatial resolution) of the ghost imaging and ghost diffraction measurements required translation stages. Mechanical adaptors of the crystals used in the synchrotron and the laboratory experiments are shown in **Appendix B**.

The ghost diffraction experiments (see **Chapter 6**) required the use of custom slits with apertures on the micron scale. The slits were composed of Si, since the highest energy of X-ray fluorescence is on the order of 1.8 keV, which has a high absorption in air. The slits were manufactured by Mr. Mark Oxman from the Bar-Ilan institute for nanotechnology and advanced materials.

3.2 Control and data analysis software

The experiments described in this Ph.D thesis required custom software for the control of the various positioning systems, i.e. translation and rotation stages, and of the recording devices, including a data acquisition device, a digitizer, a time correlation card, a coincidence card (see **Appendix A** for details), a multi-channel analyzer (MCA), and a CCD. A control program was therefore written (see further description for the hardware and software design in **Appendix C1** [61]). The analysis of the experimental measurements was done with a data analysis program (see further description for software design in **Appendix C2** [62]). The programs were both written with MATLAB software.

4. Article: X-ray Thermal Ghost Imaging with a Laboratory Source

Aviad Schori and Sharon Shwartz,

Optics Express

Volume 25, page 14822, June 2017



X-ray ghost imaging with a laboratory source

A. SCHORI AND S. SHWARTZ*

Physics Department and Institute of Nanotechnology and advanced Materials, Bar Ilan University, Ramat Gan, 52900 Israel.

*sharon.shwartz@biu.ac.il

Abstract: We describe an experiment demonstrating ghost imaging with an incoherent low brightness X-ray tube source. We reconstruct the images of 10 μm and 100 μm slits with very high contrast. Our results advance the possibilities that the high-resolution method of ghost diffraction will be utilized with tabletop X-ray sources.

© 2017 Optical Society of America

OCIS codes: (110.4980) Partial coherence in imaging; (030.1640) Coherence; (110.7440) X-ray imaging; (340.0340) X-ray optics.

References and links

1. F. Ferri, D. Magatti, V. G. Sala, and A. Gatti, "Longitudinal coherence in thermal ghost imaging," *Appl. Phys. Lett.* **92**(26), 261109 (2008).
2. M. I. Kolobov, *Quantum Imaging* (Springer Science + Business Media, 2007).
3. F. Ferri, D. Magatti, A. Gatti, M. Bache, E. Brambilla, and L. A. Lugiato, "High-resolution ghost image and ghost diffraction experiments with thermal light," *Phys. Rev. Lett.* **94**(18), 183602 (2005).
4. X. F. Liu, X. H. Chen, X. R. Yao, W. K. Yu, G. J. Zhai, and L. A. Wu, "Lensless ghost imaging with sunlight," *Opt. Lett.* **39**(8), 2314–2317 (2014).
5. P. Ryczkowski, M. Barbier, A. T. Friberg, J. M. Dudley, and G. Genty, "Ghost imaging in the time domain," *Nat. Photonics* **10**(3), 167–170 (2016).
6. T. B. Pittman, Y. H. Shih, D. V. Strekalov, and A. V. Sergienko, "Optical imaging by means of two-photon quantum entanglement," *Phys. Rev. A* **52**(5), R3429–R3432 (1995).
7. P. A. Morris, R. S. Aspden, J. E. Bell, R. W. Boyd, and M. J. Padgett, "Imaging with a small number of photons," *Nat. Commun.* **6**, 5913 (2015).
8. R. S. Bennink, S. J. Bentley, and R. W. Boyd, "Two-Photon coincidence imaging with a classical source," *Phys. Rev. Lett.* **89**(11), 113601 (2002).
9. B. Sun, M. P. Edgar, R. Bowman, L. E. Vittert, S. Welsh, A. Bowman, and M. J. Padgett, "3D computational imaging with single-pixel detectors," *Science* **340**(6134), 844–847 (2013).
10. W. Gong and S. Han, "High-resolution far-field ghost imaging via sparsity constraint," *Sci. Rep.* **5**(1), 9280 (2015).
11. F. Ferri, D. Magatti, L. A. Lugiato, and A. Gatti, "Differential ghost imaging," *Phys. Rev. Lett.* **104**(25), 253603 (2010).
12. K. W. C. Chan, M. N. O'Sullivan, and R. W. Boyd, "High-order thermal ghost imaging," *Opt. Lett.* **34**(21), 3343–3345 (2009).
13. M. Bina, D. Magatti, M. Molteni, A. Gatti, L. A. Lugiato, and F. Ferri, "Backscattering differential ghost imaging in turbid media," *Phys. Rev. Lett.* **110**(8), 083901 (2013).
14. P. Zerom, Z. Shi, M. N. O'Sullivan, K. W. C. Chan, M. Krogstad, J. H. Shapiro, and R. W. Boyd, "Thermal ghost imaging with averaged speckle patterns," *Phys. Rev. A* **86**(6), 063817 (2012).
15. J. H. Shapiro, "Computational ghost imaging," *Phys. Rev. A* **78**(6), 061802 (2008).
16. S. Oppel, R. Wiegner, G. S. Agarwal, and J. von Zanthier, "Directional superradiant emission from statistically independent incoherent nonclassical and classical sources," *Phys. Rev. Lett.* **113**(26), 263606 (2014).
17. C. Thiel, T. Bastin, J. Martin, E. Solano, J. von Zanthier, and G. S. Agarwal, "Quantum imaging with incoherent photons," *Phys. Rev. Lett.* **99**(13), 133603 (2007).
18. L. Basano and P. Ottonello, "Ghost imaging: open secrets and puzzles for undergraduates," *Am. J. Phys.* **75**(4), 343–351 (2007).
19. Y. Bromberg, O. Katz, and Y. Silberberg, "Ghost imaging with a single detector," *Phys. Rev. A* **79**(5), 053840 (2009).
20. H. Liu, X. Shen, D. Zhu, and S. Han, "Fourier-transform ghost imaging with pure far-field correlated thermal light," *Phys. Rev. A* **76**(5), 053808 (2007).
21. R. I. Khakimov, B. M. Henson, D. K. Shin, S. S. Hodgman, R. G. Dall, K. G. H. Baldwin, and A. G. Truscott, "Ghost imaging with atoms," *Nature* **540**(7631), 100–103 (2016).
22. H. N. Chapman and K. A. Nugent, "Coherent lensless X-ray imaging," *Nat. Photonics* **4**(12), 833–839 (2010).
23. J. Miao, P. Charalambous, J. Kirz, and D. Sayre, "Extending the methodology of X-ray crystallography to allow imaging of micrometre-sized non-crystalline specimens," *Nature* **400**(6742), 342–344 (1999).

24. I. McNulty, J. Kirz, C. Jacobsen, E. H. Anderson, M. R. Howells, and D. P. Kern, "High-resolution imaging by Fourier transform X-ray holography," *Science* **256**(5059), 1009–1012 (1992).
25. F. Pfeiffer, T. Weitkamp, O. Bunk, and C. David, "Phase retrieval and differential phase-contrast imaging with low-brilliance X-ray sources," *Nat. Phys.* **2**(4), 258–261 (2006).
26. J. Cheng and S. Han, "Incoherent coincidence imaging and its applicability in X-ray diffraction," *Phys. Rev. Lett.* **92**(9), 093903 (2004).
27. D. Pelliccia, A. Rack, M. Scheel, V. Cantelli, and D. M. Paganin, "Experimental X-Ray ghost imaging," *Phys. Rev. Lett.* **117**(11), 113902 (2016).
28. H. Yu, R. Lu, S. Han, H. Xie, G. Du, T. Xiao, and D. Zhu, "Fourier-transform ghost imaging with hard X rays," *Phys. Rev. Lett.* **117**(11), 113901 (2016).
29. D. Borodin, A. Schori, F. Zontone, and S. Shwartz, "X-ray photon pairs with highly suppressed background," *Phys. Rev. A* **94**(1), 013843 (2016).
30. S. Shwartz, R. N. Coffee, J. M. Feldkamp, Y. Feng, J. B. Hastings, G. Y. Yin, and S. E. Harris, "X-ray parametric down-conversion in the Langevin regime," *Phys. Rev. Lett.* **109**(1), 013602 (2012).

1. Introduction

Ghost imaging (GI) and Ghost diffraction (GD) are imaging techniques, in which the reconstruction of objects is achieved by using the spatial intensity correlations between two beams. In many schemes, this is done by introducing spatial intensity fluctuations into the input beam, which is split into two beams with identical intensity fluctuations. One of the beams propagates through the object and it is collected by a single-pixel detector while the second beam does not interact with the object and it is collected by a multi-pixel detector. The image is reconstructed from the instantaneous spatial-second-order intensity correlation function that is measured for various realizations of the intensity fluctuations at the input [1].

The thermal light sources are implemented either by using a coherent source together with optical components with a small speckle size such as a rotating glass [1–3] or a spatial light modulator, or by using true thermal light sources [4]. The advantage of the former approach is the ability to control the resolution and the contrast of the apparatus by choosing the speckle size and their variation rate [2, 3]. The techniques have been studied extensively in the optical regime [1–20] and recently GI with atoms [21] and temporal GI [5] have been demonstrated.

Since the use of X-ray lenses for imaging is very limited because of their small magnification and aperture size, lensless techniques are widely used in this regime [22–25]. However, despite that nanometer scale resolution has been achieved with coherent X-ray radiation, which is generated by X-ray free-electron lasers [22], X-ray imaging with low brightness incoherent sources utilize mainly direct absorption measurements and no magnification or small magnification is used. Consequently, although the phase information of objects could enhance the contrast of images, this quantity is almost never measured in systems based on incoherent sources, and the resolution of those systems is not smaller than the pixel size of the camera. Both GI and GD are promising for X-ray imaging since they require neither coherent bright sources nor lenses and can lead to high-resolution and high-contrast imaging techniques that can be implemented with low-cost X-ray sources [26].

X-ray GI and GD have been demonstrated experimentally with synchrotron radiation generated by large accelerators [27, 28]. In the GI experiment the intensity fluctuations of the synchrotron were used, while in the GD experiment, the authors used spatially coherent radiation and a diffuser with a moving porous gold film. While those important demonstrations advance significantly the extension of GI and GD into the X-ray regime, the sources that were used are not tabletop sources.

We note that GI and GD techniques can be implemented also by using photon pairs that are created by using parametric down conversion [2, 6, 7]. However, X-ray parametric down-conversion with reasonable signal-to-noise ratio has been reported only with synchrotron sources [29, 30].

Here we make another step in the direction of utilizing tabletop sources for high-resolution X-ray imaging and demonstrate experimentally thermal GI with an X-ray tube

source. We describe experiments that show the possibility to reconstruct images by using incoherent X-ray sources. Although the source is incoherent, we implement the thermal source by using a rotating copy paper. This is because the intensity fluctuations of the source are weak and fast. We note that this scheme works since the divergence of X-ray beams is much weaker than the divergence of optical beams due to the very short wavelength.

2. Experimental system and procedure

The experiments are conducted by using the Rigaku Smartlab X-ray diffraction system with a 9 kW rotating Cu anode system, which radiates at 8.05 keV (1.54 \AA). The schematic of the experimental setup of the GI experiments is shown in Fig. 1. The beam is collimated and monochromatized by parabolic multilayer mirror and a Gc(220) channel-cut monochromator. The estimated divergence angle is about 0.1 mrad. The relative spectral bandwidth $\Delta E/E$ is about 10^{-4} .

We introduce the intensity fluctuations by using a diffuser made from a copy paper, where the average speckle size is about $1 \mu\text{m}$. We split the beam into two beams by using a highly oriented pyrolytic graphite (HOPG) crystal in Bragg geometry, where we choose the (004) reflection and the corresponding Bragg angle is 27.5° . We choose to implement the beam splitter with the HOPG because, as we show below, its rocking curve is much broader than the width of the angular distribution of the intensity fluctuations and because its reflection efficiency is nearly 50%. The HOPG is mounted 100 mm from the diffuser.

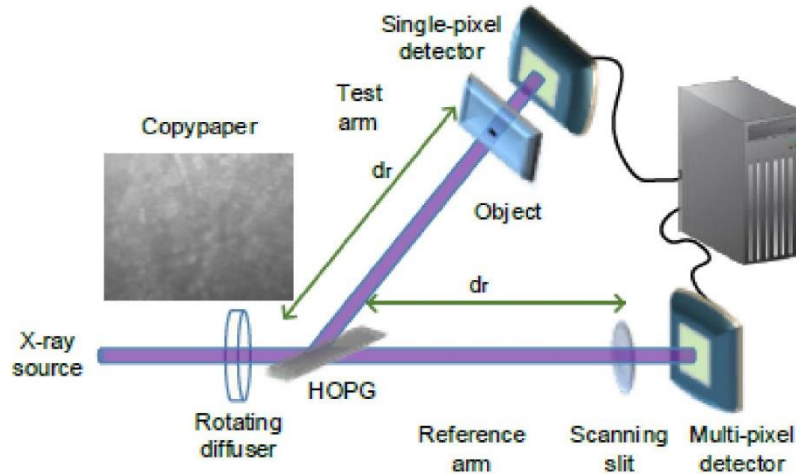


Fig. 1. Schematic of the ghost imaging experimental setup. A copy paper diffuser is mounted on a rotation stage. A highly oriented pyrolytic graphite crystal splits the beam into a transmitted beam (reference arm) and a reflected beam (test arm). The spatial resolution of the reference arm is realized via a scanning slit. The object is mounted very close to the single-pixel detector and the distances between the two detectors and the highly oriented pyrolytic graphite are equal.

For detectors, we use a fast silicon drift detector (SDD) and an avalanche photo-diode (APD). The reflected beam propagates through the object and it is collected by one of the detectors, which we denote as the test detector. The transmitted beam propagates directly into the detection system, which includes a scanning slit and a second detector that we denote as the reference detector. The input average flux before the diffuser is 2×10^8 photons/s. The diffracted average flux and the transmitted average flux are $\sim 1 \times 10^7$ photons/s and $\sim 2 \times 10^7$

photons/s, respectively (about 6×10^7 photons/s are absorbed in the HOPG crystal). The scanning slits and the objects are mounted very close to the detectors and centered with respect to the centers of the beams.

The objects we test in this work are one-dimensional 10 μm and 100 μm slits. The resolution of the scans is 2 μm and 10 μm , for 10 μm and 100 μm slits, respectively. The properties of the objects and the scanning slits are summarized in Table 1. We summarize the parameters of the measurements in Table 2. We denote the distances between the detectors and the beam splitter as d_r .

Table 1. Properties of GI objects and scanning slits

Slit type	Slit size [μm]	Material	Thickness [μm]	Transmission
Object	10	Tungsten	20	1.77×10^{-3}
Object	100	Stainless steel	1000	0
Scanning slit	2	Tungsten	20	1.77×10^{-3}
Scanning slit	5	Gold and stainless steel	25.4, 12.7	2.12×10^{-6}

Table 2. Parameters of GI measurements

Object size [μm]	d_r [mm]	Diffuser rotation speed [deg/sec]	Reference counts [C.P.S.]	Test counts [C.P.S.]	Coincidence photons per realization	Number of realizations
10	150	5	37,500	21,800	1.066×10^8	3.6×10^3
100	550	1.5	8,000	10,000	6.125×10^7	2.4×10^3

Denoting x_{ref} and x_{test} as the coordinates across the reference and the test detectors, respectively, we write the normalized second-order intensity correlation function as [2]:

$$G^{(2,2)}(x_{\text{ref}}, x_{\text{test}}) = \frac{\langle I_{\text{ref}}(x_{\text{ref}}) I_{\text{test}}(x_{\text{test}}) \rangle - \langle I_{\text{ref}}(x_{\text{ref}}) \rangle \langle I_{\text{test}}(x_{\text{test}}) \rangle}{\langle I_{\text{ref}}(x_{\text{ref}}) \rangle \langle I_{\text{test}}(x_{\text{test}}) \rangle}. \quad (1)$$

where the indices I_{ref} , I_{test} are the average intensities (the count rate divided by the effective area of the detector) at the reference and test detectors, respectively. The $\langle \cdot \rangle$ indicates an ensemble average over the realizations, where each of the realizations refers to a different position on the copy paper and therefore represents different intensity fluctuations.

To reconstruct the images of the objects we calculate the normalized second-order intensity correlation function from the measurements of the intensities of both detectors at various positions of the scanning slit before the reference detector. For each position of the scanning slit we rotate the diffuser continuously at a constant velocity. The parameters for each of the measurements are summarized in Table 2. We apply a minimal threshold to the coincidence counts of each realization to enhance the visibility of the image [18]. We obtain the average intensities of the two detectors by averaging over the intensities of all the realizations.

3. Results and discussions

Figure 2 shows the results for GI and the comparison with scanning electron microscopy (SEM) measurements. The SEM curves are obtained by integrating over two dimensional data from the SEM measurements in Fig. 3. GI and SEM measurements of the 10 μm slit are shown in panel (a) and of the 100 μm slit are shown in panel (b). The respective GI measured widths of the slits in panels (a) and (b) are $10 \pm 1 \mu\text{m}$ and $100 \pm 5 \mu\text{m}$. The respective SEM measured widths of the slits in panels (a) and (b) are $10.662 \pm 0.078 \mu\text{m}$ and $101.24 \pm 1.25 \mu\text{m}$. The measured slit widths of the GI and the SEM measurements are in agreement. The contrast between the edges of the slits and the slit centers in the GI measurements are much higher than in the SEM measurements.

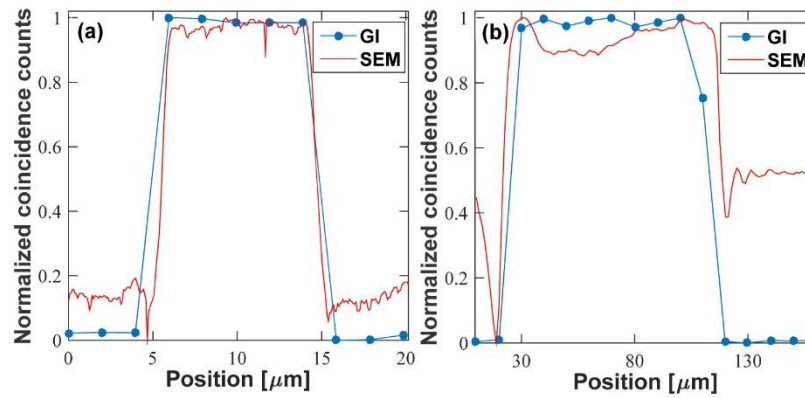


Fig. 2. GI results. (a). GI (blue dots) and scanning electron microscopy (solid red line) measurements of a 10 μm slit at a scanning resolution of 2 μm . (b). GI (blue dots) and scanning electron microscopy measurements (solid red line) of a 100 μm slit at a scanning resolution of 10 μm .

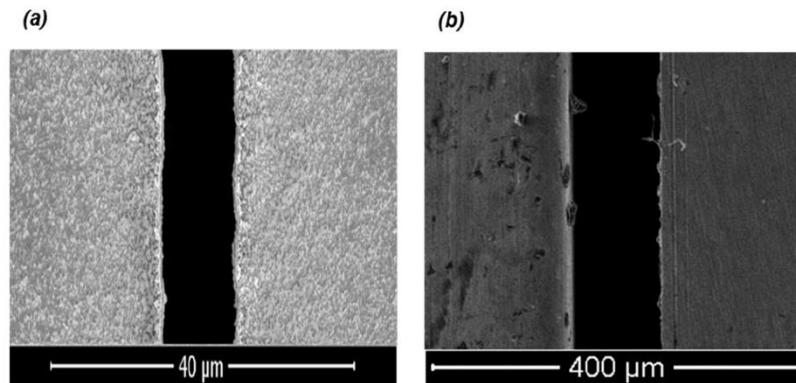


Fig. 3. Scanning electron microscopy images. (a). 10 μm slit. (b). 100 μm slit.

To get a deeper insight on our technique including its limitations and future opportunities, we discuss the parameters of the diffuser and of the beam splitter. The first parameter that affects the quality of the image is the magnitude of the intensity fluctuations that are introduced by the diffuser. Unlike the optical regime, X-ray scattering is weak in general, thus we need to verify that the scattering by the diffuser is strong enough to introduce intensity fluctuations, which are higher than the background noise. Furthermore, since we use a low brightness source, the measurement time of each realization should be such that the statistical error is smaller than the intensity fluctuations that we introduce with the diffuser. Another important parameter is the temporal rate of the variation of the intensity fluctuations. It has been shown that this rate should be slower than the response time of the detector [2, 3, 18]. However, since in this work we use fast detectors with a time resolution below 1 μsec , we overcome this challenge very easily.

A typical trace of the normalized intensity fluctuations is shown in Fig. 4(a). Each realization represents a different position on the surface of the diffuser. A 2- μm tungsten slit

is mounted in front of the detector at a distance of 350 mm from the diffuser. The integration time at each realization is 10 sec. The measured standard deviation of the intensity fluctuations introduced by the diffuser is 0.97%. The measured standard deviation of the source without a diffuser is 0.22%. The conclusion is that for sufficiently long averaging times the intensity fluctuations of the diffuser become dominant, which allows its use for GI with X-rays.

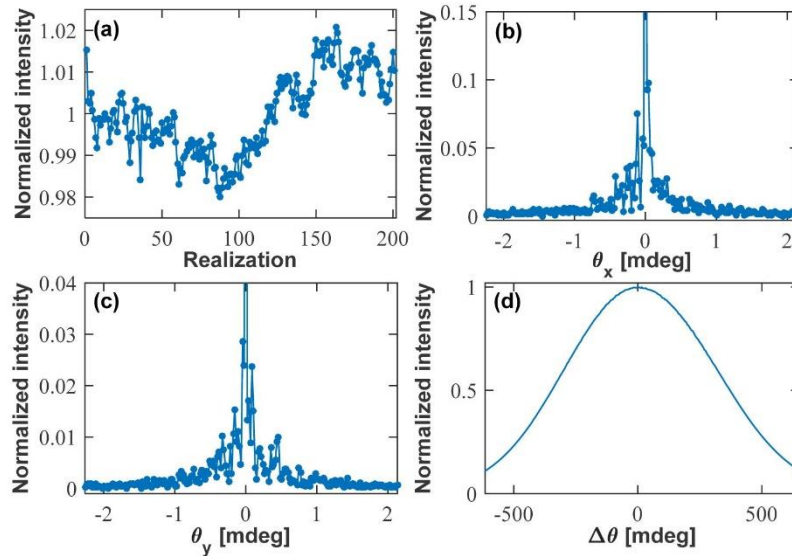


Fig. 4. Temporal and spatial properties of intensity fluctuations as introduced by the diffuser. (a). Typical intensity fluctuations for different realizations. (b). Angular distribution of the intensity fluctuations in the x direction. (c). Angular distribution of the intensity fluctuations in the y direction. (d). Rocking curve of the highly ordered pyrolytic graphite. The indices x and y are two orthogonal directions across the copy paper. The zero order in panels (b) and (c) is cut vertically.

The next important requirement is that the acceptance angle of the beam splitter is much larger than the angular spread of the intensity fluctuations that the diffuser introduces. This is because the beam splitter is based on Bragg diffraction, which is angular dependent. Thus, if the acceptance angle of the beam splitter is not wide enough, the reflected beam contains only intensity fluctuations that are within the angular acceptance of the beam splitter, while the transmitted beam contains the entire range of the fluctuations. Consequently, the intensity fluctuations of the two beams are not identical and the contrast is highly reduced.

The angular acceptance angles of the copy paper diffuser in the horizontal and vertical directions are shown in Figs. 4(b) and 4(c), respectively. The results are obtained by Fourier transforming the visible microscope image of the paper. The axes are scaled to reflect the angular acceptance of the copy paper diffuser by using the relation for small angles $\theta_i = k_i / k$, where k_i is the coordinate along the x and y axes of the Fourier transform of the microscope image, and $k = 4.078 \times 10^{10}$ 1/m is the wave vector of the X-ray source. We find that the full-width at half-maximum (FWHM) of the angular distribution of the fluctuations introduced by the copy paper diffuser is smaller than 0.002° . The rocking curve of the HOPG beam splitter is shown in Fig. 4(d). The HOPG angular acceptance angle at the FWHM is

0.72°. It is clear from Fig. 4 that the HOPG complies with the requirement that the rocking curve will be much larger than the angular spread of the intensity fluctuations.

We note that the horizontal and vertical directions in Figs. 4(b) and 4(c) exhibit different shapes and widths. The effective speckle size at the object plane can be estimated as $\theta_z z$, where z is the distance between the diffuser and the object. The calculated effective speckle sizes for the GI measurements in Figs. 2(a) and 2(b) are then approximately 4.4 μm and 9.6 μm , respectively. We note that the actual effective speckle size may be smaller due to resolution limitations of the optical microscope. Since the resolution of GI is limited by the speckle size, which has to be smaller than the object [2, 3, 13], we expect that the reconstruction of the 100 μm slit in Fig. 2(b) would be better than the reconstruction of the 10 μm slit in Fig. 2(a), where most of the speckles are larger than the imaging resolution. The results shown in Fig. 2(a) are not influenced due to the large number of realizations taken to obtain this image.

4. Conclusion

We report the observation of ghost imaging in the X-ray regime with an incoherent low-brightness laboratory system. We demonstrated the ghost imaging effect with 10 μm and 100 μm slits at scanning resolutions of 2 μm and 10 μm , respectively.

It is most likely that by mounting the object far from the test detector it will be possible to measure ghost diffraction with laboratory X-ray sources. In this scheme, the diffraction pattern of the object is reconstructed from the measurements of the correlation function [26]. In this case the resolution of the image is limited by the largest k-vector of the beam and by the near field speckle size and not by the pixel size of the multi-pixel detector [20].

We therefore expect that the resolution of ghost diffraction will be much better than the pixel size of the state-of-the-art cameras. Hence, this approach can lead to the development of high-resolution incoherent X-ray imaging techniques. Moreover, since in ghost diffraction, the diffraction pattern depends on variations of the refractive index of the object and not just on its absorption, the approach can lead also to high-contrast imaging techniques. This is because the phase inhomogeneity that is introduced by objects is in many cases much stronger than the amplitude variations [25].

Funding

Israel Science Foundation (ISF) (1038/13).

Acknowledgments

We thank Netanel Shpigel for performing the SEM measurements. We thank Moshe Lindner for performing the microscope measurement.

5. Ghost Imaging with Paired X-ray Photons

Aviad Schori, Denis Borodin, Kenji Tamasaku, and Sharon Shwartz,

Physical Review Letters

Submitted, December 2017

Ghost Imaging with Paired X-ray Photons

A. Schori^{1,2}, D. Borodin^{1,2}, K. Tamasaku², S. Shwartz^{1,2}*

¹*Physics Department and Institute of Nanotechnology, Bar Ilan University, Ramat Gan, 52900 Israel*

²*RIKEN SPring-8 Center, 1-1-1 Koto, Sayo-cho, Sayo-gun, Hyogo 679-5148 Japan*

We report the experimental observation of ghost imaging with paired x-ray photons, which are generated by parametric down-conversion. We use the one-to-one relation between the photon energies and the emission angles and the anti-correlation between the k-vectors of the signal and the idler photons to reconstruct the images of slits with nominally zero background levels. Further extension of our procedure can be used for the observation of various quantum phenomena at x-ray wavelengths.

*Sharon.shwartz@biu.ac.il

Parametric down conversion (PDC) is one of the major sources for the generation of non-classical states of light [1-4]. This type of radiation can be used to study fundamental quantum phenomena and lead to many fascinating applications [1-4]. Indeed, numerous quantum optics effects have been demonstrated by using visible and infrared radiation. In contrast, while several papers described the observation of x-ray PDC [5-9] and a scheme for its application as a source for polarization-entangled states has been proposed [10], the use of the x-ray photon pairs that are generated by PDC has never been reported. Implementation of concepts of quantum optics such as interaction free measurements [11] and sub-shot noise measurements [12] could be very advantageous for measurements at x-ray wavelengths since they can be used to reduce the dose of x-rays that interact with samples while enhancing the resolution and contrast of the measurements and even for radiation damage free measurements [11]. The existence of commercially available x-ray detectors with the capability to resolve the number of photons and with near unity quantum efficiency is appealing for testing concepts of quantum physics since these properties can be used to remedy many of the fundamental challenges of conventional quantum optics with optical radiation.

One of the well-studied applications of PDC in the optical regime is as a generator of correlated (or anti-correlated) photon pairs for quantum ghost imaging (GI) experiments [13-17]. It should be noted that while GI has been observed also with classical sources [18-25], the classical experiments do not show the important properties of quantum states of light such as the violation of the Heisenberg uncertainty principle with regards to position and momentum [26] and sub-shot noise imaging [12]. The latter can lead to damage free imaging, which is one of the greatest challenges of x-ray imaging.

In a typical scheme of GI, one of the photons is scattered from the object and is collected by a single-pixel detector, which does not provide sufficient information to reconstruct the image. The second photon, which does not interact with the object, is collected by a multi-pixel detector, which provides the spatial resolution. However, this detector does not provide any direct information on the object, and hence the reconstruction of the image is done by correlating the data from the two detectors. GI with photon pairs can be observed by using either the spatial correlations between the photons or the anti-correlations between their k-vectors.

Similar to the optical regime, the photon pairs that are generated by x-ray PDC are correlated in space and their k-vectors are anti-correlated and therefore can be used for the demonstration of GI. PDC in the x-ray regime is supported by the plasma-like nonlinearity, which is a second-order nonlinear process that is non-zero even in centro-symmetric materials [10]. This nonlinearity is orders of magnitude weaker than typical nonlinearities in the optical regime. However, the number of modes of the quantum fluctuations, which are the driving mechanism for PDC, scale as the cube of the frequencies of the pertinent waves, thus leading to measurable coincidence count rates. Since those wavelengths are on the order of one Angstrom, which is on the order of the distance between atomic planes in crystals, phase matching is achieved by using a reciprocal lattice vector as described in Fig. 1(a). These very small wavelengths imply also that the diffraction limit resolution of x-rays is on the order of the atomic scale.

In this Letter, we describe measurements of GI, which are based on x-ray PDC. We use the anti-correlations between the k-vectors of x-ray photon pairs to reconstruct images of 2 mm and 4 mm slits with nominally zero background levels. This is the first demonstration of an application for x-ray photon pairs that are generated by PDC, which can hence advance the possibilities of using this type of source for the observations of quantum effects with x-rays. This is important since to date there are only a few demonstrations of quantum optics at x-ray wavelengths, which were obtained by using Mossbauer nuclei [27-30], but no demonstration of x-ray quantum optics with PDC has been reported. The use of PDC for quantum optics is expected to open many new possibilities similar to the optical regime. We note that our experiment is fundamentally different from the recent observations of classical GI at x-ray wavelengths where the source for the correlations was diffraction from speckles [21-25]. However, since the sources for the correlations in those observations are classical they cannot be used for the demonstration of quantum physics phenomena.

In contrast to most experiments in the optical regime our experimental scheme relies on the angular spread of the k-vectors of the generated pairs, which is broader than the angular width of the object as we illustrate in Fig. 1(b). The reason for the large angular spread is the momentum conservation of the PDC process (phase matching), which uses the reciprocal lattice vector [8,9]. The non-collinear phase-matching condition, which we depict in Fig. 1(b), can be written as $\vec{k}_p + \vec{G} = \vec{k}_s + \vec{k}_i$, where \vec{k}_p , \vec{k}_s , and \vec{k}_i are the k-vectors of the pump, the signal, and the idler respectively. \vec{G} is the reciprocal lattice vector orthogonal

to the atomic planes. We denote θ_p , θ_s , and θ_i as the angles with respect to the atomic planes of the pump, the signal, and the idler, respectively. The energy conservation implies that $\omega_p = \omega_s + \omega_i$, where we denote ω_p , ω_s , and ω_i as the angular frequencies of the pump, the signal, and the idler, respectively. An important consequence of the phase matching and the energy conservation is the one-to-one relation between the k-vectors and the photon energies of the signal and idler photons. We use this property for the reconstruction of the ghost images.

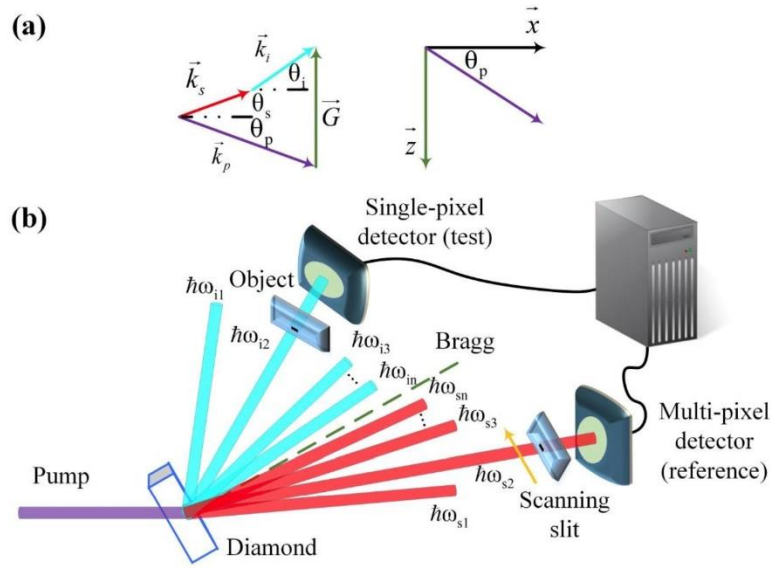


FIG 1. (a) Phase-matching scheme. The indices p, s, and i correspond to the pump, the signal, and the idler, respectively. \vec{G} is the reciprocal lattice vector, and the angles θ_p , θ_s , and θ_i are the angles with respect to the atomic planes of the pump, the signal, and the idler, respectively. (b) Schematic of the experimental setup. The spatial resolution of the reference detector is implemented by using a scanning slit (the scanning direction is denoted by the yellow arrow). The object is mounted close to the single-pixel detector and the distance between the two detectors and the nonlinear crystal is 1050 mm. The angular spread of the down-converted signals represents the one-to-one relation between the k-vectors and the photon energies of the signal and the idler photons, denoted as $h\omega_s$ and $h\omega_i$, respectively. The dashed line represents the direction of Bragg diffraction.

We conducted the experiments described below at the RIKEN SR physics beamline (BL19LXU) of SPring-8 [31-33]. The schematic of the experimental system is shown in Fig. 1(b). The dimensions of the input beam are 0.5 mm (horizontal) x 0.7 mm (vertical). To suppress the noise from Compton and Bragg scattering, we use a geometry where the angles between the emerging photon pairs, which are nearly collinear, and the input beam is close to 90 degrees and the pump polarization is in the scattering plane [9]. We implement this geometry by working with a pump beam at 22.3 keV and by using the reciprocal lattice vector normal to the C(660) atomic planes at Laue geometry for phase-matching. The Bragg angle in this geometry is 41.5° . The pump deviation from the Bragg angle at the phase matching condition is 10 mdeg. The degenerate photon energies of the signal and idler are 11.15 keV, where the angular separation between the detectors is $\sim 2.1^\circ$ ¹. One of the beams emerging from the nonlinear crystal passes through the object and is collected by a silicon drift detector (SDD), which is located behind the object and that we denote as the test detector. The second beam is collected by a 0.5 ± 0.025 mm slit and a second SDD that we denote as the reference detector. We resolve the angular dependence of the coincidence count rates by moving the 0.5 mm slit and reference detector together across the horizontal direction with a scanning resolution of 0.5 mm (the corresponding angular resolution is $\sim 0.029^\circ$). We measured the coincidence count rate of the x-ray pairs by using coincidence electronics that records only photons that hit the two detectors within a time window of about 120 ns. We filter out false coincidences by registering only events where the sum of the energies from the two detectors is equal to the pump energy within an energy window of 1 keV.

Since our GI procedure relies on the anti-correlations between the k-vectors of the signal and idler photons and on the one-to-one correspondence between the k-vectors and the photon energies of the pairs, we begin by verifying these properties. In Figs. 2 and 3 we present the coincidence spectra for the reference detector (left column) and the test detector (right column) measured with 4 mm and 2 mm slits, respectively. The first row shows the three-dimensional plots of the coincidence count rates as a function of the photon energy and of the position of the reference slit² measured at the reference and test detectors, respectively. In the second to the fourth rows of Fig. 2 and the second and third rows of Fig. 3 we show the

¹ The errors are determined by the size of the largest slit and are 0.11° and 0.23° for the 2 and 4 mm slits, respectively.

² Which is equivalent to the angular difference for the small angular ranges.

spectra at a specific position of the reference slit. The blue bars are the experimental results and the solid red lines are calculated from theory and scaled to the peak of the spectra of the reference detector³.

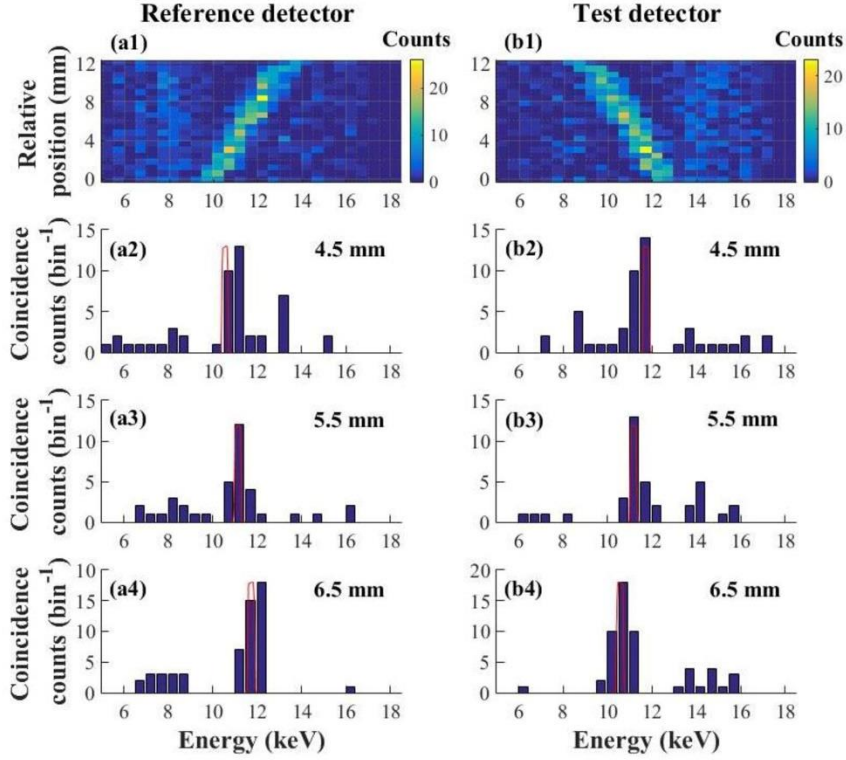


FIG 2. Energy spectra of the coincidence counts for the 4 mm slit: reference detector (left column) and the test detector (right column). (a1) and (b1) Coincidence counts as a function of the photon energy and of the position of the reference slit. (a2)-(a4) and (b2)-(b4) Spectra of the coincidence counts at various positions of the reference slit. The blue bars are the experimental results and the solid red lines are calculated from theory and scaled to the peak of the spectra of the reference detector.

The bright diagonal areas near the center of the spectra in panels (a1) and (a2) of Figs. 2 and 3 correspond to the x-ray pairs that are generated by the PDC process. As we

³ The description of our theoretical calculation has been described in previous papers [8,9] and is also described in detail in the supplementary section [31,32].

expect, the PDC coincidence spectra shift with the position of the reference slit due to the one-to-one relation between the photon energies and the emission angles. Of importance, our analysis of the raw data confirms that the PDC spectra are independent on the bandwidth of the energy filter. It is clear from the spectra at the various positions of the reference slit in panels (a2)-(a4) and (b2)-(b4) of Fig. 2 and in panels (a2)-(a3) and (b2)-(b3) of Fig. 3 that the measured central photon energies of the PDC process agree with the theory within the energy resolution of the detection system (we expect a spectral shift as a result of the position of the reference slit of ~ 0.5 keV/mm and measure a spectral shift of 0.4 ± 0.125 keV/mm for the 4 mm slit and 0.4 ± 0.25 keV/mm for the 2 mm slit). It is also clear that the PDC spectra are well separated from the background.

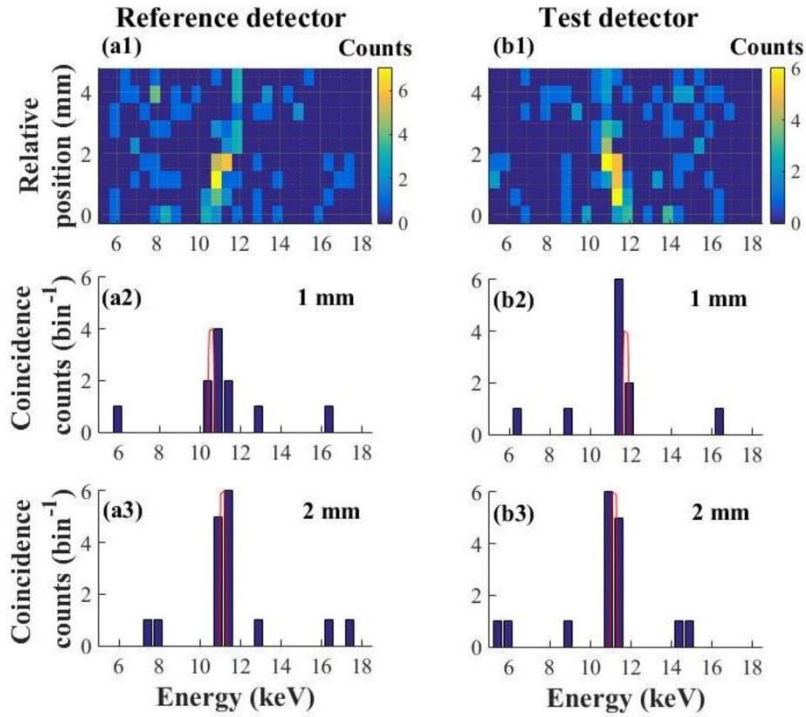


FIG 3. Energy spectra of the coincidence counts for the 2 mm slit: reference detector (left column) and the test detector (right column). (a1) and (b1) Coincidence counts as a function of the photon energy and of the position of the reference slit. (a2)-(a3) and (b2)-(b3) Spectra of the coincidence count rates at various positions of the reference slit. The blue bars are the experimental results and the solid red lines are calculated from theory and scaled to the peak of the spectra of the reference detector.

By comparing panels (a1) and (b1) of Figs. 2 and 3, we conclude that the energy range of the PDC process in Fig. 3 is smaller than in Fig. 2. This is due to the smaller acceptance angle of the 2 mm slit, which restricts the number of PDC modes. The dependence of the spectrum on the 0.5 mm slit position in Figs. 2 and 3 suggests that the energy resolution of our system is sufficient for the reconstruction of the images of the slits.

We note that since the width of the measured PDC spectrum is proportional to the width of the narrowest used slit [8,31,32], it is possible to resolve the widths of slits without using any direct spatial measurement. This can be done by simply measuring the coincidence spectrum and by using the one-to-one relation between the photon energies and the k-vectors of the photon pairs. The widths of the spectra that we obtain by summing up the data at the different positions of the reference slit for the 4 and 2 mm slits are 2 ± 0.25 keV and 1 ± 0.25 keV, respectively, and ~ 2.2 keV and ~ 1 keV for our numerical simulations and are in agreement with within the energy bandwidth of our system [31,32].

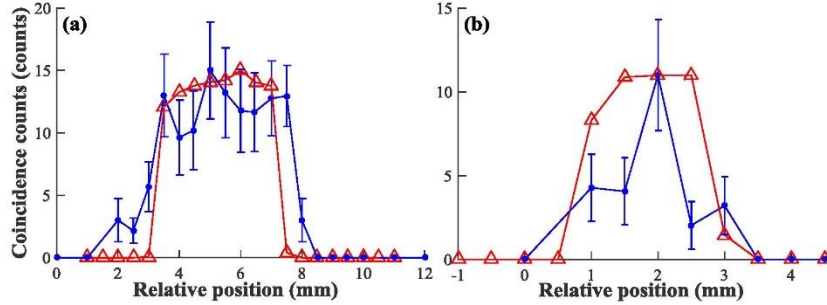


FIG 4. Ghost imaging of (a) 4 mm and (b) 2 mm slits. The blue circles are the data that constitute the ghost imaging and the red triangles are direct imaging measurements by using a scanning slit behind the object. The coincidence counts in the ghost imaging plots are scaled to the geometry of the detector (see text for more details). The direct imaging measurements are taken with $\sim 10^6$ counts per slit position and scaled to the peaks of the ghost images. The solid lines are guides for the eye. The error bars are estimated by assuming a Poisson distribution.

After verifying that the spectrum shifts with the position of the reference detector, we show that this property can be used to demonstrate GI. We use the coincidence

measurements of the spectra in Figs. 2 and 3 to reconstruct the ghost images of the slits by counting the photon pairs with photon energies of the reference detector in a bandwidth between 11 keV and 11.5 keV at each of the positions of the scanning slit. We corrected the reconstructed images to account for the round shape of the detectors. GI and direct imaging of the 4 mm slit are shown in panel (a) and of the 2 mm slit are shown in panel (b) of Fig. 4. The measured slit widths at the full-width at half-maximum by GI and by direct imaging are in agreement within the width of the pump beam (4.75 ± 0.5 mm and 4 ± 0.25 mm for the GI and direct imaging of the 4 ± 0.5 mm slit, respectively, and 2 mm and 2 ± 0.25 mm for the GI and direct imaging of the 2 mm slit, respectively). Due to the narrow energy bandwidth the average coincidence count rate in our measurements is only ~ 7 photon pairs per hour. It is clear from the results that the background level is nominally zero. It is also clear from the results that our scheme is well suited to measurements with extremely low count rates, which can be advantageous for a variety of quantum optics experiments. This is due to the extremely low noise of x-ray detectors and the use of coincidences and the energy resolution of our detection system. We note that even with the low statistics of up to 10 photons per slit position in the GI results in panel (b) of Fig. 4, the width of the slit is already discernable.

In summary, we reported the observation of GI by utilizing x-ray photon pairs. This is the first demonstration of an application of x-ray pairs that are generated by the process of PDC.

The strong and clear anti-correlations between the k-vectors we have shown suggest that it would be possible to use our procedure to observe quantum optics effects at x-ray wavelengths. For example, by using a smaller scanning slit or a 2D detector [34] with a small pixel size, it would be possible to measure the near-field correlations and the far-field correlations simultaneously [26]. Further suppression of the fluorescence background will allow the measurement of the signal and idler photons without coincidences, which will likely lead to sub-shot noise measurements [12]. The quality of the ghost imaging can be further improved by using new emerging high-repetition rate free-electron lasers such as the European XFEL [35] and LCLS-II-HE [36]. Finally, in this work we demonstrated the ability to measure x-ray photon pairs with a negligible background level, which opens the possibilities to observe quantum optics with x-ray photon pairs. As a consequence, we expect that the extension of our procedure can be used for the observation of single heralded photons, which can be used for experiments in quantum x-ray optics [37,38]. Another

promising extension of the scheme we present is the demonstration of two-photon x-ray diffraction [39].

We acknowledge the SPring8 Facility for provision of synchrotron radiation facilities. This work was supported by the Israel Science Foundation (ISF), grant number 1038/13. This research was supported by a Marie Curie FP7 Integration Grant within the 7th European Union Framework Programme under grant agreement No. PCIG13-GA-2013-618118. D.B. gratefully acknowledges support by the Ministry of Aliyah and Immigrant Absorption of Israel.

References

- [1] M. O. Scully and M. S. Zubairy, *Quantum Optics* (Cambridge university press, Cambridge, 1997).
- [2] D. F. Walls and G. J. Milburn, *Quantum Optics* (Springer, New York, 2008).
- [3] C. C. Knight and P. L. Gerry, *Introductory Quantum Optics* (NY: Cambridge University Press, New York, 2007).
- [4] M. I. Kolobov, *Quantum Imaging* (Springer, New York, 2007).
- [5] P. M. Eisenberger and S. L. McCall, Phys. Rev. Lett. **26**, 684 (1971).
- [6] Y. Yoda, T. Suzuki, X. W. Zhang, K. Hirano, and S. Kikuta, J. Synchrotron Rad. **5**, 980 (1998).
- [7] B.W. Adams, *Nonlinear Optics, Quantum Optics, and Ultrafast Phenomena with X-Rays* (Kluwer Academic Publisher, Norwell, MA, 2008).
- [8] S. Shwartz, R. N. Coffee, J. M. Feldkamp, Y. Feng, J. B. Hastings, G. Y. Yin, and S. E. Harris, Phys. Rev. Lett. **109**, 013602 (2012).
- [9] D. Borodin, A. Schori, F. Zontone, and S. Shwartz, Phys. Rev. A **94**, 013843 (2016).
- [10] S. Shwartz and S. E. Harris, Phys. Rev. Lett. **106**, 080501 (2011).
- [11] G. B. Lemos, V. Borish, G. D. Cole, S. Ramelow, R. Lapkiewicz, and A. Zeilinger, Nature **512**, 409 (2014).
- [12] G. Brida, M. Genovese, and I. R. Berchera, Nat. Photonics **4**, 227 (2010).
- [13] T. B. Pittman, Y.H. Shih, D.V. Strekalov, and A.V. Sergienko, Phys. Rev. A **52**, R3429 (1995).
- [14] P. A. Morris, R. S. Aspden, J. E. Bell, R. W. Boyd, and M. J. Padgett, Nature Comm. **6** (2015).
- [15] R. S. Aspden, Nathan R. Gemmell, P. A. Morris, D. S. Tasca, L. Mertens, M. G. Tanner, R. A. Kirkwood, A. Ruggeri, A. Tosi, R. W. Boyd, G. S. Buller, R. H. Hadfield, and M. J. Padgett, Optica **2**, 1049 (2015).

- [16] F. Kaneda, B. G. Christensen, J. J. Wong, H. S. Park, K. T. McCusker, and P. G. Kwiat, *Optica* **2**, 1010 (2015).
- [17] M. N. O’Sullivan, K. W. C. Chan, and R. W. Boyd, *Phys. Rev. A* **82**, 053803 (2010).
- [18] F. Ferri, D. Magatti, V.G. Sala and A. Gatti, *App. Phys. Lett.* **92**, 261109 (2008).
- [19] F. Ferri, D. Magatti, A. Gatti, M. Bache, E. Brambilla, and L. A. Lugiato, *Phys. Rev. Lett.* **94**, 183602 (2005)
- [20] R. S. Bennink, S. J. Bentley, and R. W. Boyd, *Phys. Rev. Lett.* **89**, 113601 (2002).
- [21] D. Pelliccia, A. Rack, M. Scheel, V. Cantelli, and D. M. Paganin, *Phys. Rev. Lett.* **117**, 113902 (2016).
- [22] H. Yu, R. Lu, S. Han, H. Xie, G. Du, T. Xiao, and D. Zhu, *Phys. Rev. Lett.* **117**, 113901 (2016).
- [23] A. Schori and S. Shwartz, *Opt. Express* **25**, 14822 (2017).
- [24] D. Pelliccia, M. P. Olbinado, A. Rack, and D. M. Paganin, *Arxiv:1710.00727*.
- [25] A. Zhang, Y. He, L. Wu, L. Chen, B. Wang, *Arxiv:1709.01016*.
- [26] J. C. Howell, R. S. Bennink, S. J. Bentley, and R.W. Boyd, *Phys. Rev. Lett.* **92**, 210403 (2004).
- [27] R. Röhlsberger, HC Wille, K. Schlage, and B. Sahoo, *Nature* **482**, 199 (2012).
- [28] R. Röhlsberger, K. Schlage, B. Sahoo, S. Couet, and R. Ruffer, *Science* **328**, 1248 (2010).
- [29] F. Vagizov, V. Antonov, Y. V. Radeonychev, R. N. Shakhmuratov, and O. Kocharovskaya, *Nature* **508**, 80 (2014).
- [30] J. Haber, X. Kong, C. Strohm, S. Willing, J. Gollwitzer, L. Bocklage, R. Ruffer, A. Pálffy, and R. Röhlsberger, *Nat. Photonics* **11**, 720, (2017).
- [31] See Supplemental Material at (URL) for a more detailed overview of the theory, the numerical simulations, and the experimental setup.
- [32] Additional experimental and theoretical details are given in Ref. [31].

- [33] M. Yabashi, T. Mochizuki, H. Yamazaki, S. Goto, H. Ohashi, K. Takeshita, T. Ohata, T. Matsushita, K. Tamasaku, Y. Tanaka, and T. Ishikawa, Design of a beamline for the SPring-8 long undulator source 1, *Nucl. Instrum. Methods Phys. Res., Sect. A* **467**, 678 (2001).
- [34] B. M. Jost, A. V. Sergienko, A. F. Abouraddy, B. E. Saleh, and M. C. Teich, *Opt. Express* **3**, 81 (1998).
- [35] S. Serkez, G. Geloni, S. Tomin, G. Feng, E. V. Gryzlova, A. N. Grum-Grzhimailo, and M. Meyer, *J. Opt* **20**, 024005 (2018).
- [36] R. W. Schoenlei, S. Boutet, M. P. Minitti and A.M. Dunne, *Appl. Sci.* **7**, 850 (2017).
- [37] S.A. Castelletto and R.E. Scholten, *Eur. Phys. J. Appl. Phys.* **41**, 181 (2008).
- [38] M. D. Eisaman, J. Fan, A. Migdall, and S. V. Polyakov, *Rev. Sci. Instrum.* **82**, 071101 (2011).
- [39] J. Stöhr, *Phys. Rev. Lett.* **118**, 024801 (2017).

Supplementary Material for "Ghost Imaging with Paired X-ray Photons"

A. Schori^{1,2}, D. Borodin^{1,2}, K. Tamasaku², S. Shwartz^{1,2}

¹Physics Department and Institute of Nanotechnology, Bar Ilan University, Ramat Gan, 52900 Israel

²RIKEN SPring-8 Center, 1-1-1 Koto, Sayo-cho, Sayo-gun, Hyogo 679-5148 Japan

Experimental details

We provide further details on the experimental setup and on the procedures that we describe in the main text.

First, we elaborate on the experimental setup. The average input power is $\sim 5 \times 10^{13}$ photons/s and its polarization is in the scattering plane. The input beam is monochromatic at 22.3 keV. The nonlinear crystal is a 4 mm x 4 mm x 0.8 mm diamond crystal. The Bragg angle is 41.5° . The pump deviation from the Bragg angle at the phase matching condition is 10 mdeg. The degenerate photon energies of the signal and idler are 11.15 keV, where the angular separation between the detectors is $\sim 2.1^\circ$. We use Helium ducts, which are mounted between the nonlinear crystal and the detectors to reduce the air absorption of the PDC photon pairs.

Next, we describe the coincidence electronics as shown in Fig. 1. Each of the detectors provides a logical output signal that is used as an input to an AND gate. The output of the AND gate is used to trigger the digitizer and determines the width of the time window of each coincidence event. The width of the time window in our setup is 120 nsec. For each event that is within the time window, the analog signals of the two detectors, which are proportional to the detected photon energies, are recorded with a digitizer (PICOSCOPE 6000). The values of the photon energies of the two detectors are calibrated according to the incident pump energy. The raw data of the digitizer trace of the analog signals are corrected by using DC subtraction according to the voltage levels at the tail of the pulses of the analog signals.

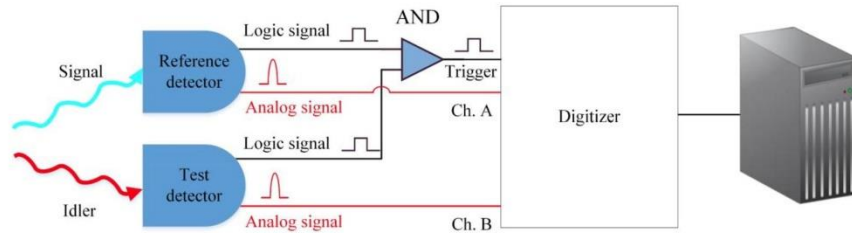


FIG 1. Schematic of the electronic setup.

Resolving the slit size from the spectra

We show that it is possible to use the measured coincidence spectra to resolve the widths of slits without using any direct spatial measurement. For this purpose, we utilize the one-to-one correspondence between the photon energies and the k-vector directions of the photon pairs as is illustrated in Fig. 1(b) of the Letter. Panels (a) and (b) of Fig. 2 show the total coincidence spectra of 4 mm and 2 mm slits, respectively. The blue bars are the experimental results and the solid red lines are calculated from theory and scaled to the peak of the spectra. Since we sum over the different positions of the reference slit, each spectrum in Fig. 2 is equivalent to a measurement with a large area reference detector. Hence, the bandwidth of each spectrum is determined by the size of the test slit due to the one-to-one correspondence between the photon energies and the k-vector directions of the photon pairs. The experimental results in panels (a) and (b) of Fig. 2 are in agreement with the numerical simulations. The PDC spectra can therefore be used to measure the support of objects even without using the spatial resolution of the reference detector. The spectra in Fig. 2 are generated by summing up over the counts of the energy histograms at the reference detector positions of 3 to 6.5 mm in panel (a) and 1 to 3 mm in panel (b).

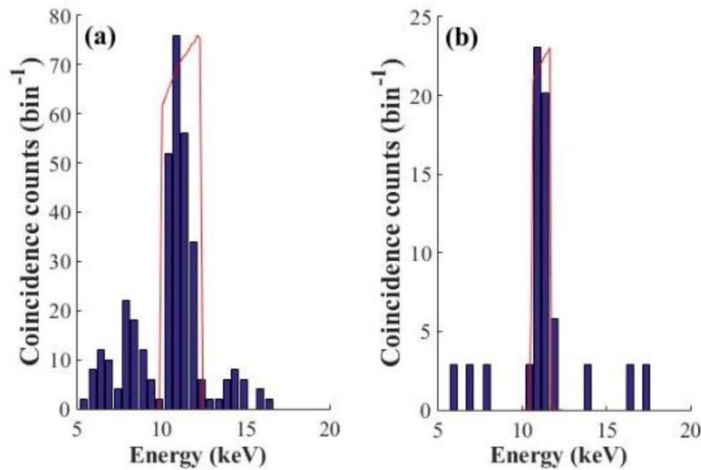


FIG 2. Slits size from spectra: Reference detector photon energy spectra of the coincidence counts of (a) 4 mm slit and (b) 2 mm slit. The histograms are constructed by summing up the data at the different positions of the reference slit. The blue bars are the experimental results and the solid red lines are calculated from theory and scaled to the peak of each of the spectrum. The accidental coincidences on the right and left of the coincidence spectra are a consequence of summing over the entire spectra and the different positions of the reference slit.

Details of the theoretical calculations

We provide a further mathematical description of the wave equation model that we use for the comparison with the experimental results.

The nonlinear current density at a geometry where the angles between the signal and the idler with respect to the pump are close to 90° , which we use in our numerical simulations, can be expressed as follows [9]

$$\mathbf{J}_s^{\text{NL}}(\omega_s = \omega_p - \omega_i) = -\frac{e\rho_g E_p E_i^*}{4m_e^2 \omega_p^2 \omega_i} (\vec{G} \cdot \hat{e}_p)(\hat{e}_i \cdot \hat{e}_s), \quad (\text{A1})$$

where m_e and e are the electron mass and charge, respectively; \vec{G} is the reciprocal lattice vector orthogonal to the atomic planes, and E_i and E_p are the electric fields of the idler and the pump, respectively; \hat{e}_p , \hat{e}_s , and \hat{e}_i are the polarizations of the pump, the signal and the idler, respectively; ω_p , ω_s , and ω_i , are the angular frequencies of the pump, the signal and the idler, respectively; $\rho_0 = \rho_g \exp(i\vec{G} \cdot \vec{r})$ is the charge density in the absence of the pump.

Under the assumptions of undepleted pump approximation and slowly varying envelope approximation (SVEA), the coupled wave equations describing the PDC process in the frequency domain can be described as [8,9]

$$\begin{aligned} \frac{\partial a_s}{\partial z} + \frac{\alpha_s}{\cos \theta_s} a_s &= -\kappa' a_i^+ \exp[i\Delta k_z z] + \sqrt{\frac{2\alpha_s}{\cos \theta_s}} f_s, \\ \frac{\partial a_i^+}{\partial z} + \frac{\alpha_i}{\cos \theta_i} a_i^+ &= -\kappa'^* a_s \exp[-i\Delta k_z z] + \sqrt{\frac{2\alpha_i}{\cos \theta_i}} f_i^+, \end{aligned} \quad (\text{A2})$$

where α_s and α_i are the absorption coefficients at the signal and idler wavelengths, respectively, θ_s and θ_i are the signal and idler angles angle with respect to the atomic planes, respectively, and Δk_z is the phase mismatch along the z axis; $f_s(z, \mathbf{q}, \omega)$ and $f_i^+(z, \mathbf{q}, \omega)$ are the Langevin noise operators; $\kappa' = \frac{i\kappa}{\sqrt{\cos \theta_s \cos \theta_i}}$, where

$$\kappa = \frac{(2\hbar\eta_p\eta_s\eta_i\omega_p\omega_s\omega_i)^{\frac{1}{2}} J_s^{\text{NL}}}{2\omega_s E_i^*}$$

is the nonlinear coupling coefficient.

The time-space signal and idler operators are related to their frequency domain counterparts by

$$\begin{aligned} a_s(z, \mathbf{r}, t) &= \int \int_{0-\infty}^{\infty} a_s(z, \mathbf{q}, \omega) [-i(\mathbf{q} \cdot \mathbf{r} - \omega t)] d\mathbf{q} d\omega, \\ a_i(z, \mathbf{r}, t) &= \int \int_{0-\infty}^{\infty} a_i(z, \mathbf{q}, \omega) [-i(\mathbf{q} \cdot \mathbf{r} - \omega t)] d\mathbf{q} d\omega, \end{aligned} \quad (\text{A3})$$

where $\mathbf{r} = (x, y)$. The commutation relations for the signal and idler operators are

$$\left[a_j(z_1, \mathbf{q}_1, \omega_1), a_k^\dagger(z_2, \mathbf{q}_2, \omega_2) \right] = \frac{1}{(2\pi)^3} \delta(z_1 - z_2) \delta(\mathbf{q}_1 - \mathbf{q}_2) \delta(\omega_1 - \omega_2). \quad (\text{A4})$$

Here $\mathbf{q}_j = (k_{jx}, k_{jy})$, where k_{jx} and k_{jy} represent the k wave-vector components parallel to the surfaces of the crystal. The signal count rate is given by $\langle a_s^\dagger(z, \mathbf{r}_2, t_2) a_s(z, \mathbf{r}_1, t_1) \rangle$.

The coincidence count rate for ghost imaging can be considered as follows:

$$R_c = A(2\pi)^6 \iiint \langle a_i^+(\omega_1, k_{x1}, k_{y1}) a_s^+(\omega_2, k_{x2}, k_{y2}) a_s(\omega_2, k_{x2}, k_{y2}) a_i(\omega_1, k_{x1}, k_{y1}) \rangle x |H(\omega_1)|^2 |H(\omega_2)|^2 |H(k_{x1})|^2 |H(k_{x2})|^2 |H(k_{y1})|^2 |H(k_{y2})|^2 d\omega_1 d\omega_2 dk_{x1} dk_{x2} dk_{y1} dk_{y2}, \quad (\text{A5})$$

where A is the effective spot size of the pump, 1 and 2 are the indices the two detectors, respectively, and H is the window function of the object.

Simulation details

The parameters of the simulations that lead to the theoretical results corresponding to Figs. 2 and 3 of the Letter are the horizontal and vertical reference detector acceptance angles of 0.48 and 5.4 mrad, respectively.

The offset values of the detector angles from the phase-matching solutions at the degeneracy in Figs. 2 and 3 of the Letter are determined according to the different positions of the reference detector with respect to the center of the GI image, which we define as the phase-matching condition at the degeneracy.

The parameters of the simulations that lead to the theoretical results corresponding to Fig. 2(a) of the supplementary section are the horizontal and vertical test detector acceptance angles of 3.8 and 5.4 mrad, respectively. The parameters of the simulations that lead to the theoretical results corresponding to Fig. 2(b) of the supplementary section are the horizontal and vertical test detector acceptance angles of 1.9 and 5.4 mrad, respectively.

6. X-ray Thermal Ghost Diffraction with a Laboratory Source

Aviad Schori and Sharon Shwartz,

Provisional patent, January 2018

The results described here have been presented in the FRISNO 14 and in the PQE-2017 conferences

X-ray Ghost Diffraction with a Laboratory Source

Abstract

I describe an experiment demonstrating preliminary results of ghost diffraction with an incoherent low brightness X-ray tube source for the first time. I measure the diffraction pattern of a Si micropores mesh on top of a 20 μm slit with a spatial resolution of about 1 μm . My results advance the possibilities that the high-resolution method of ghost diffraction will be utilized with tabletop X-ray sources.

Introduction

Ghost imaging (GI) and Ghost diffraction (GD) are imaging techniques, in which the reconstruction of objects is achieved by using the spatial intensity correlations between two beams. In many schemes, this is done by introducing spatial intensity fluctuations into the input beam, which is split into two beams with identical intensity fluctuations. One of the beams propagates through the object and it is collected by a single-pixel detector while the second beam does not interact with the object and it is collected by a multi-pixel detector. The image is reconstructed from the instantaneous spatial-second-order intensity correlation function that is measured for various realizations of the intensity fluctuations at the input [1].

The thermal light sources at X-ray wavelengths are implemented either by using a moving diffuser [1,3,4] or the intensity fluctuations of the X-ray source [30]. The advantages of the former approach are the ability to control the resolution and the contrast of the apparatus by choosing the speckle size and their variation rate [3,4] and their independence of the measurement time at each position of the diffuser.

Since the use of X-ray lenses for imaging is very limited because of their small magnification and aperture size, lensless techniques are widely used in this regime [25–27]. However, despite that nanometer scale resolution has been achieved with coherent X-ray radiation, which is generated by X-ray free-

electron lasers [298], X-ray imaging with low brightness incoherent sources utilize mainly direct absorption measurements and no magnification or small magnification is used. Consequently, although the phase information of objects could enhance the contrast of images, this quantity is almost never measured in systems based on incoherent sources, and the resolution of those systems is not smaller than the pixel size of the camera. Both GI and GD are promising for X-ray imaging since they require neither coherent bright sources nor lenses. GI of X-rays has been recently demonstrated with a laboratory source with a copy paper diffuser by imaging one dimensional slits [see publication reference 1]. However, the best spatial resolution of the images that was achieved in that experiment was 2 μm . This is since the spatial resolution in GI is limited not only by the speckle size of the diffuser but also by the scanning resolution. The demonstration of GD with a laboratory source that utilizes a diffuser with a nanoscale speckle size can lead to high-resolution and high-contrast imaging techniques that can be implemented with low-cost X-ray sources [see publication reference 1].

Here I make another step in the direction of utilizing tabletop sources for high-resolution X-ray imaging and demonstrate experimentally thermal GD with an X-ray tube source. I describe experiments that show the possibility to reconstruct the image of a micropores mesh by using incoherent X-ray sources. Although the source is incoherent, I implement the thermal source by using a rotating Fe_2O_3 with copy paper. This is because the intensity fluctuations of the source are weak and fast. I note that this scheme works since the divergence of X-ray beams is much weaker than the divergence of optical beams due to the very short wavelength. The Fe_2O_3 compound was manufactured by Eitan Edri (Hagay Shpaisman group, chemistry department, Bar-Ilan University).

Experimental system and procedure

The experiments are conducted by using the Rigaku Smartlab X-ray diffraction system with a 9 kW rotating Cu anode system, which radiates at 8.05 keV (1.54 \AA). The schematic of the experimental setup of the GD experiments is shown in **Fig. 6.1**. The beam is collimated and monochromatized by parabolic multilayer mirror and a Ge(220) channel-cut monochromator. The estimated divergence angle is about 0.1 mrad. The relative spectral bandwidth $\Delta E / E$ is about 10^{-4} .

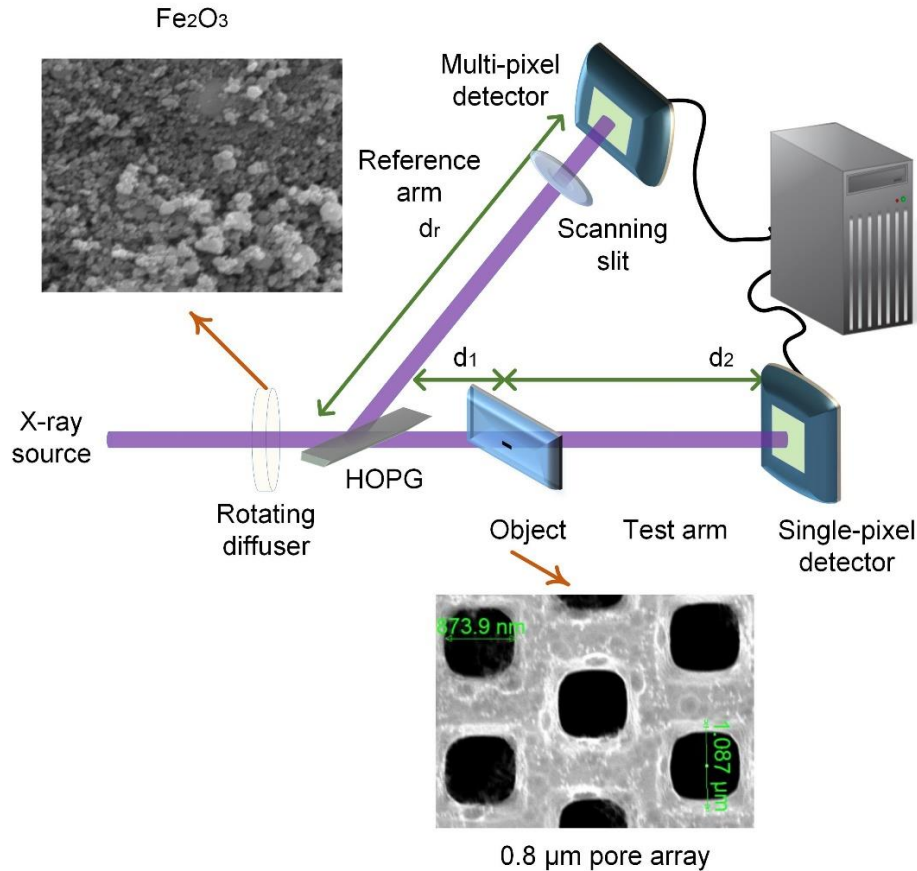


Figure 6.1 - Schematic of the ghost diffraction experimental setup. A Fe_2O_3 with a copy paper diffuser (see the scanning electron microscope image) is mounted on a rotation stage. A highly oriented pyrolytic graphite crystal splits the beam into a transmitted beam (test arm) and a reflected beam (reference arm). The spatial resolution of the reference arm is realized via a scanning slit. The object (see the scanning electron microscope image of the micropores mesh object) is mounted very close to the beam splitter. The distances between the two detectors and the highly oriented pyrolytic graphite are equal, such that $d_1+d_2=d$.

I introduce the intensity fluctuations by using a diffuser made from Fe_2O_3 nanoparticles and copy paper, where the average size of the Fe_2O_3 nanoparticles is about 50 nm. I split the beam into two beams by using a highly ordered pyrolytic graphite (HOPG) crystal in Bragg geometry, where I choose the (004) reflection and the corresponding Bragg angle is 27.5° . I choose to implement the beam splitter with the HOPG because its rocking curve is much broader than the width of the angular distribution of the intensity fluctuations and because its reflection efficiency is nearly 50% [see publication reference 1]. The HOPG is mounted 100 mm from the diffuser.

For detectors, I use two avalanche photo-diodes (APD). The transmitted beam propagates through the object and it is collected by one of the detectors, which I denote as the test detector. The reflected beam propagates directly into the detection system, which includes a scanning slit and a second detector that I denote as the reference detector. The input average flux before the diffuser is $\sim 2 \times 10^8$ photons/s. The diffracted average flux and the transmitted average flux are $\sim 1 \times 10^7$ photons/s and $\sim 3 \times 10^7$ photons/s, respectively (about 1.6×10^8 photons/s are absorbed in the HOPG crystal). The scanning slit is mounted very close to the detector and centered with respect to the center of the beam. The object is positioned at a distance ~ 50 mm from the beamsplitter and at a distance of ~ 500 mm from the detector and centered with respect to the center of the beam. The distance of the object from the diffuser is ~ 100 mm.

The object I test in this work is comprised of a micropores Si mesh and a $20 \mu\text{m}$ gold slit. The resolution of the scan is $5 \mu\text{m}$. The scanning slit is a $5 \mu\text{m}$ gold slit. The Si micropres mesh has an average inter-pore distance of $1.5 \mu\text{m}$, pore diameters in the range of $0.8\text{-}1 \mu\text{m}$, and an average pore thickness of $200 \mu\text{m}$. For each position of the scanning slit I rotate the diffuser continuously at a constant velocity of 0.2 deg/s . I summarize the parameters of the measurement in **Table 6.1**. I denote the distances between the detectors and the beam splitter as d_r .

Object type	d_r [mm]	Reference counts [C.P.S.]	Test counts [C.P.S.]	Coincidence photons per realization	Number of realizations
Si micropres+ $20 \mu\text{m}$ slit	550	10,000	20,000	7,000	30,000

Table 6.1 - Parameters of the GD measurement

Denoting x_{ref} and x_{test} as the coordinates across the reference and the test detectors, respectively, we write the normalized second-order intensity correlation function as [3]:

$$(6.1) \quad G^{(2,2)}(x_{\text{ref}}, x_{\text{test}}) = \frac{\langle I_{\text{ref}}(x_{\text{ref}}) I_{\text{test}}(x_{\text{test}}) \rangle - \langle I_{\text{ref}}(x_{\text{ref}}) \rangle \langle I_{\text{test}}(x_{\text{test}}) \rangle}{\langle I_{\text{ref}}(x_{\text{ref}}) \rangle \langle I_{\text{test}}(x_{\text{test}}) \rangle},$$

where the indices I_{ref} , I_{test} are the average intensities (the count rate divided by the effective area of the detector) at the reference and test detectors, respectively. The $\langle \cdot \rangle$ indicates an ensemble average over the

realizations, where each of the realizations refers to a different position on the diffuser and therefore represents different intensity fluctuations.

To reconstruct the diffraction patterns of the objects I calculate the normalized second-order intensity correlation function from the measurements of the intensities of both detectors at various positions of the scanning slit before the reference detector. For each position of the scanning slit I rotate the diffuser and measure the intensities of both detectors at the different positions of the diffuser. The parameters of the measurement are summarized in **Table 6.1**. I apply a minimal threshold to the coincidence counts of each realization to enhance the visibility of the image [18]. I position the object close to the diffuser in order to minimize the average speckle size on the object plane and consequently obtain a high spatial resolution. I obtain the average intensities of the two detectors by averaging over the intensities of all the realizations.

Theory

The coincidence count rate for a reference (which is denoted as ref in the equations) and a test detector is [29]¹:

$$(6.2) \quad \begin{aligned} \text{Coincidence count rate} &= \langle E_{\text{ref}}^*(x_{\text{ref}}) E_i^*(x_{\text{test}}) E_{\text{test}}(x_{\text{test}}) E_{\text{ref}}(x_{\text{ref}}) \rangle = \\ &= \langle I_{\text{test}}(x_{\text{test}}) \rangle \langle I_{\text{ref}}(x_{\text{ref}}) \rangle + |rt| \left| \iint G^{(1,1)}(x_1, x_2) h_{\text{ref}}(x_1, x_{\text{ref}}) h_{\text{test}}^*(x_2, x_{\text{test}}) dx_1 dx_2 \right|^2, \end{aligned}$$

where $\langle \dots \rangle$ represents a time average, $I_{\text{ref, test}}$, $E_{\text{ref, test}}$, and $h_{\text{ref, test}}$ are respectively the intensities, the field amplitudes, and the impulse responses at the reference and test detectors, and r and t are the respective reflection and transmission amplitudes of the beam splitter. $G^{(1,1)}(r_1, r_2)$ is the first order spatial

¹ Valid under the following assumptions:

- The source is monochromatic and therefore there is no time dependency.
- The source cross-section is much larger than the object and all optical elements and therefore there is translational invariance in the transverse plane.

correlation function between the reference and test beams, which I define^m as $G^{(1,1)}(\mathbf{r}_1, \mathbf{r}_2) = I(\mathbf{r}_1) e^{-0.5 \left(\frac{\mathbf{r}_1 - \mathbf{r}_2}{r_{\text{coh}}} \right)^2}$

. Here, r_{coh} denotes the spatial correlation of the source.

The impulse responses at the reference and test detectors can be described by taking into account Fresnel free space propagation and the transmission of the object [29]:

$$(6.3) \quad \begin{aligned} h_{\text{ref}}(x_1, x_{\text{ref}}) &= \frac{e^{-jk d_r}}{i \lambda d_r} e^{-\frac{i\pi}{\lambda d_r} (x_1 - x_{\text{ref}})^2} \\ h_{\text{test}}(x_2', x_{\text{test}}) &= \int dx' \frac{e^{-ik d_1}}{i \lambda d_1} e^{-\frac{i\pi}{\lambda d_1} (x_2' - x')^2} t(x') \frac{e^{-ik d_2}}{i \lambda d_2} e^{-\frac{i\pi}{\lambda d_2} (x_{\text{test}} - x')^2} \end{aligned}$$

where k and λ are the wave vector and the wavelength of the source, respectively and $t(x')$ is the transmission of the object. The distances d_1 , d_2 , and d_r , are the distance of the object from the beam splitter, the distance of the object from the test detector, and the distance of the reference detector from the beam splitter, as shown in **Fig. 6.1.1**. I assume that the reference and test detectors are equidistant from the beam splitter so that $d_1 + d_2 = d_r$.

Results and discussion

Fig. 6.2 shows the results for GD and the comparison with numerical simulations of the micropores Si mesh on top of a 20 μm gold slit. I note that the slit is used similarly to focusing in coherent diffraction imaging, since the diffraction pattern of a large area will be smeared due to the averaging over the many diffraction of the micropores elements. The numerical simulations were performed according to **Eqs. 6.2** and **6.3**. The measured GD and the numerical simulations are in agreement within the scanning resolution.

The resolution of the diffraction pattern is determined according to $\frac{\lambda d_2}{\text{F.S.}}$ [75], where λ is the wavelength

^m For a fully spatially incoherent beam the correlation can be described as a delta function. I assume that the input beam is uniform.

and F.S. is the total width of the diffraction pattern. The calculated spatial resolution of the measurement is $0.97 \mu\text{m}$ and is therefore smaller than the scanning resolution.

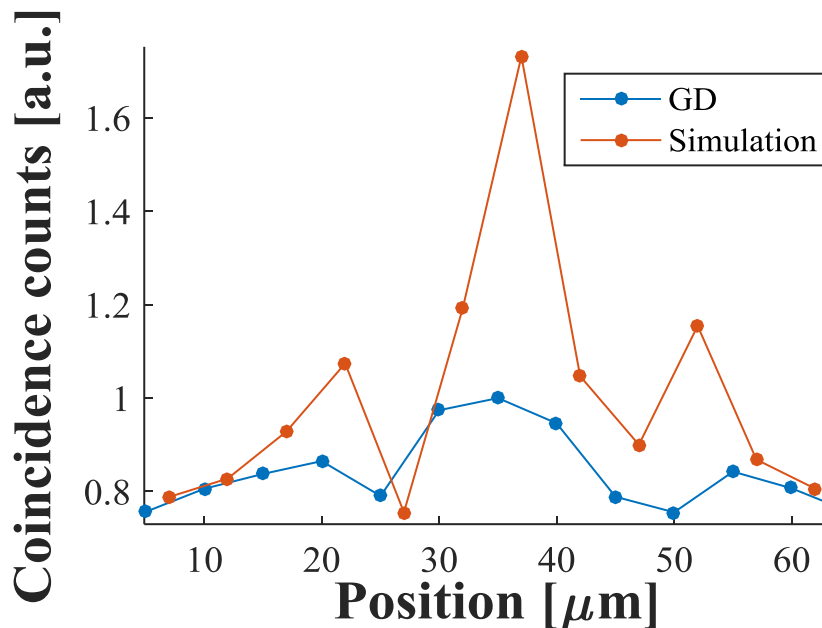


Figure 6.2 – Ghost diffraction results. Ghost diffraction (blue dots) and numerical simulations (solid red line) measurements of a Si micropores mesh on top of a $20 \mu\text{m}$ slit with a scanning resolution of $5 \mu\text{m}$. The solid lines are guides for the eye.

Next, the normalized spatial correlations of the system are measured. This is done by measuring the spatial correlation function of the system similarly to the ghost imaging experimental scheme (see **Fig. 1 of Chapter 4**) with the exception that two identical slits are used. The measurement is done with two $5 \mu\text{m}$ slits and with a scanning resolution of $10 \mu\text{m}$. The distance of the two detectors from the diffuser was $\sim 550 \text{ mm}$. The distances of the two detectors from the beam splitter is $\sim 460 \text{ mm}$. The calculated spatial resolution of the measurement is $\sim 300 \text{ nm}$. Hence, I conclude that the angular acceptance angles of the diffuser and the beam splitter are sufficient to obtain the spatial resolution of the GD measurement of **Fig. 6.2**. It should also be noted that the spatial properties of the HOPG beam splitter have been previously discussed in **Chapter 4**. Two-dimensional measurements of the spatial correlations of the system that were performed with synchrotron radiation are described in the supplementary material.

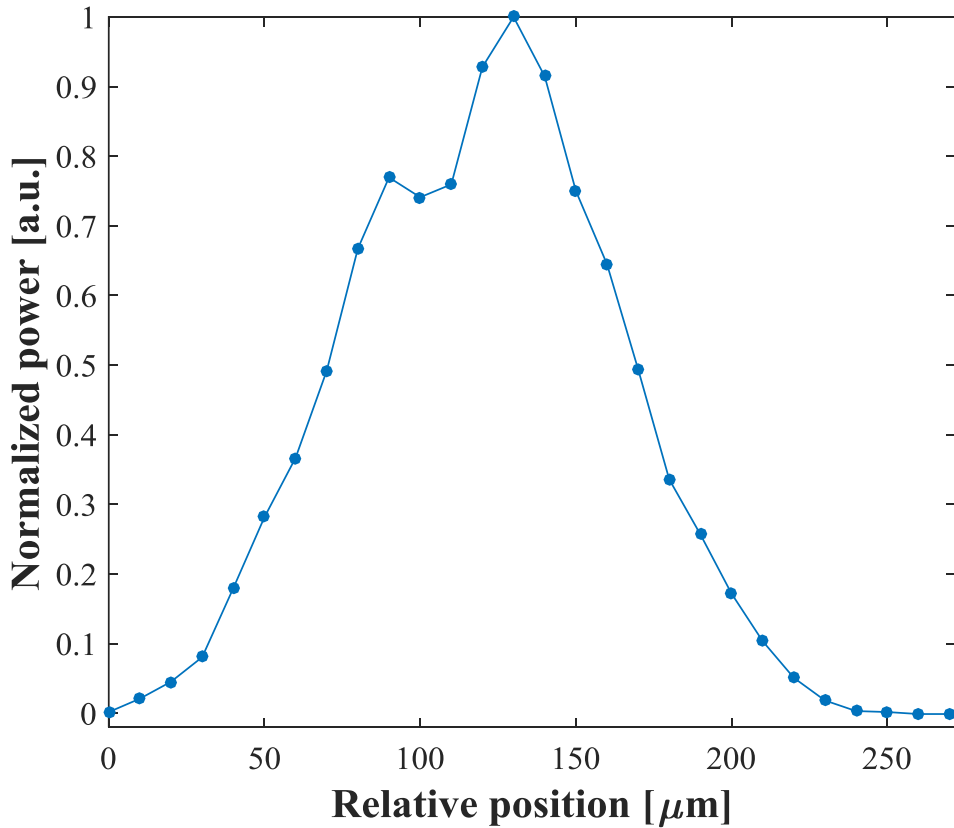


Figure 6.3 - Normalized spatial correlation of the intensity fluctuations as introduced by the Fe_2O_3 and copy paper diffuser. The distances of the two detectors from the beam splitter is ~ 460 mm. The solid line is a guide for the eye.

Conclusion

I report the observation of ghost diffraction in the X-ray regime with an incoherent low-brightness laboratory system. I demonstrated the ghost diffraction effect by using an object comprised of a micropores Si mesh and a $20 \mu\text{m}$ gold slit with a spatial resolution of $0.97 \mu\text{m}$.

The spatial resolution I obtained is smaller than the scanning resolution of the measurements and is better than the spatial resolution of the state-of-the-art cameras. Hence, this approach can lead to the development of high-resolution incoherent X-ray imaging techniques with laboratory sources. Moreover, since the diffraction pattern depends on variations of the refractive index of the object and not just on its

absorption, the approach can lead also to high-contrast imaging techniques, since the phase inhomogeneity that is introduced by objects is in many cases is much stronger than the amplitude variations [28].

The spatial resolution and the contrast of the measurements can be improved by using a two-dimensional detector. The contrast is improved since the relative intensity fluctuations introduced by the diffuser are increased when the pixel size is smaller and the resolution is expected to improve since large areas average over many speckles. The resolution can also be improved by using a diffuser that contains sub-nanoparticles [63] or by using atoms as the diffusing element [24].

Supplementary Material

I describe the measurement of the far-field spatial correlations with a diffuser that is comprised of Fe_2O_3 nanoparticles and of copy paper that were performed with synchrotron radiation. The measurement is performed by measuring the spatial correlation function of the system similarly to the ghost imaging experimental scheme (see **Fig. 1** of **Chapter 4**) with the exceptions that the reference detector is a charge-coupled device (CCD) with a pixel size of 6.5 μm . We conducted the measurement at beam line B16 of Diamond Light Source. The results of the normalized spatial correlations are shown in **Fig. 6.4(a)**. The photon energy was 10.5 keV ($\lambda=0.118$ nm). The test beam was generated using reflection geometry for the (002) atomic planes of the HOPG crystal. The distances of the two detectors from the beam splitter and from the diffuser were 1,500 mm and 1,575 mm respectively. The calculated spatial resolution of the systemⁿ at the vertical axis is ~ 180 nm. Hence, the angular acceptance of the diffuser and the beam splitter are sufficient to obtain the spatial resolution of the GD measurement of **Fig. 6.2**. We note that while the measurements in **Figs. 6.4(a)** and **6.1.2** were performed with different X-ray sources^o the spatial resolutions that we calculate from the spatial correlation measurements are roughly the same. The indices x (horizontal) and y (vertical) are two orthogonal directions across the diffuser. **Figure 6.4(b)** shows an example of a CCD image of the reference beam at one of the positions of the diffuser. The differences in the intensities of the image that are originated the beam splitter are easily visible by eye.

ⁿ Calculated similarly to the resolution calculation of the measurement in Fig. 6.1.3.

^o The results may be influenced by the divergence of the X-ray sources.

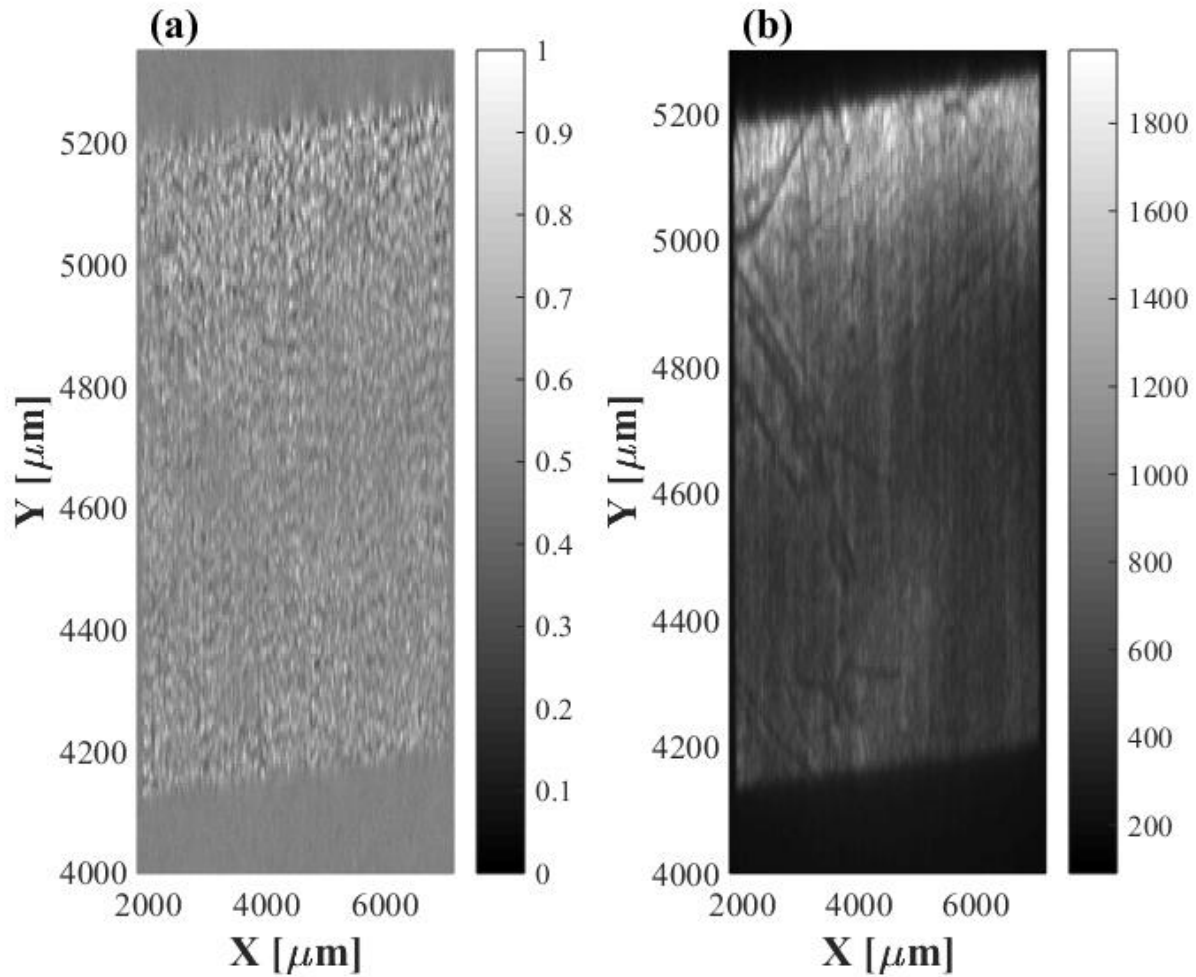


Figure 6.4 - Spatial properties of the far-field intensity fluctuations as introduced by the diffuser and the beam splitter. (a) Normalized spatial correlation of the intensity fluctuations as introduced by the Fe_2O_3 and copy paper diffuser. (b) A CCD image of the transmitted beam after the beam splitter. The indices x and y are two orthogonal directions across the diffuser. The distances of the two detectors from the diffuser and from the beam splitter were 1,575 mm and 1,500 mm, respectively.

7. Article: Parametric Down-Conversion of X rays into the Optical Regime

Aviad Schori, Christina Bömer, Denis Borodin, Steve Collins, Blanka Detlefs, Marco Moretti Sala, Shimon Yudovich, and Sharon Shwartz

Physical Review Letters

Volume 119, 253902, December 2017

Parametric Down-Conversion of X Rays into the Optical Regime

A. Schori,¹ C. Bömer,² D. Borodin,¹ S. P. Collins,³ B. Detlefs,⁴ M. Moretti Sala,⁴ S. Yudovich,¹ and S. Shwartz^{1,*}

¹*Physics Department and Institute of Nanotechnology, Bar Ilan University, Ramat Gan, 52900 Israel*

²*European XFEL, Holzkoppel 4, 22869 Schenefeld, Germany*

³*Diamond Light Source, Harwell Science and Innovation Campus, Didcot OX11 0DE, United Kingdom*

⁴*European Synchrotron Radiation Facility, BP 220, F-38043 Grenoble Cedex, France*

(Received 21 August 2017; published 21 December 2017)

We report the observation of parametrically down-converted x-ray signal photons at photon energies that correspond to idler photons at optical wavelengths. The count-rate dependence on the angles of the input beam and of the detector and on the slit sizes agrees with theory within the experimental uncertainties. The nonlinear susceptibility, which we calculated from the measured efficiencies, is comparable to the nonlinear susceptibility evaluated from the measurements of x-ray and optical wave mixing. The results of the present Letter advance the development of a spectroscopy method for probing valence-electron charges and the microscopic optical response of crystals with atomic-scale resolution.

DOI: 10.1103/PhysRevLett.119.253902

Nonlinear interactions of x rays and optical radiation can provide insight into the microscopic structure of chemical bonds, the valence electron density of crystals, and light-matter interactions at the atomic-scale resolution [1–11]. The high resolution stems from the short wavelengths of x rays, whereas the optical fields interact with the valence electrons. This probe has great potential in the study of microscopic optical properties of materials. Unfortunately, the experimental realization of these ideas is very challenging, and only a few experiments in this direction have been reported [3–10] since they were proposed almost 50 years ago [1]. The experimental observation of parametric down-conversion (PDC) of x rays to optical wavelengths has never been reported.

In processes such as x-ray and optical sum-frequency generation (SFG) and difference-frequency generation (DFG), x rays and optical waves are mixed to generate an x-ray wave at a frequency that is equal to the sum or difference of the two input frequencies, respectively. The physical mechanism that supports the wave-mixing effect can be viewed as an inelastic scattering of the input x rays from an optically modulated charge density [2,5,11,12]. Glover and colleagues reported the first observation of x-ray and optical wave mixing in a diamond crystal by using an x-ray free-electron laser and a Ti-Sapphire laser [5]. The main challenge in observing SFG in other materials is the low efficiency, which depends linearly on the intensity of the optical laser. Consequently, the observation of the effect requires optical intensities that are larger than the radiation damage threshold of most materials. It is also clear that SFG can be observed only in optically transparent materials; thus, it is not applicable for a large class of materials such as metals and superconductors.

It is possible to overcome these challenges by using PDC of x rays to optical wavelengths. This nonlinear process is

similar to x-ray and optical DFG, but in x-ray to optical PDC, the pump photons interact with vacuum fluctuations to generate correlated x-ray and optical photon pairs [1].

It should be noted that the pertinent effect of x rays into extreme ultraviolet (EUV) PDC has been applied already to investigate the optical properties of crystals [3,4,6–10]. By using this approach, the microscopic linear susceptibility of a diamond crystal with a resolution of 0.54 Å has been extracted from the measurements of the PDC for several atomic planes [4]. The extension of that method to PDC of x rays to optical wavelengths could lead to a more powerful probe. For example, it could be utilized for the investigation of phenomena that are associated with energies near the Fermi energy of metals or near the band gap of semiconductors. However, the observation of this effect is even more challenging. This is because the photon energies of the generated x-ray signal differ by only a few eV from the photon energies of the pump and because the Bragg condition is very close to the phase-matching requirement of the PDC process. Since Bragg scattering is many orders of magnitude stronger than the PDC process, the tail of the Bragg scattering has to be filtered out stringently. This requires a highly collimated and monochromatic input beam and a careful design of the experimental setup.

In this Letter, we describe measurements of the x-ray signal generated during the process of PDC for idler photons at optical wavelengths. We use a highly collimated monochromatic beam and a high-resolution multibounce crystal analyzer to measure PDC at energies that correspond to various optical wavelengths in the range of 280–650 nm for several phase-matching conditions. We evaluate the nonlinear susceptibility from the measured efficiencies and find a reasonable agreement with the theory and with the results of SFG [5].

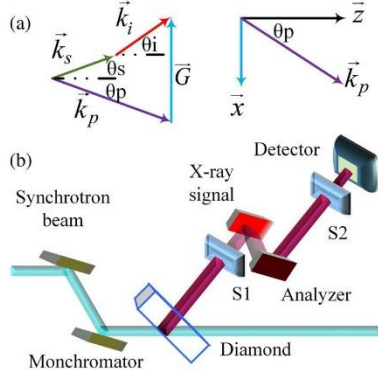


FIG. 1. (a) Phase-matching scheme. The indices p , s , and i represent the pump, signal, and idler, respectively; \vec{G} is the reciprocal lattice vector; and the angles θ_p , θ_s , and θ_i are the angles with respect to the atomic planes of the pump, the signal, and the idler, respectively. (b) Schematic of the experimental setup. The scattering plane of the analyzer is normal to the scattering plane of the diamond. S_1 and S_2 are the slits before the analyzer and before the detector, respectively.

Since x-ray wavelengths are comparable to the distance between the atomic planes, we use the reciprocal lattice vector for phase matching [12,13], as we depict in Fig. 1(a). In this Letter, we refer to the x-ray photons as the signal photons and to the optical photons as the idler photons. We denote θ_p , θ_s , and θ_i as the angles with respect to the atomic planes of the pump, the signal, and the idler, respectively. The k vectors of the pump, the signal, and the idler are \vec{k}_p , \vec{k}_s , and \vec{k}_i , respectively. Note that \vec{G} is the reciprocal lattice vector orthogonal to the atomic planes. The energy conservation implies that $\omega_p = \omega_s + \omega_i$, where we denote ω_p , ω_s , and ω_i as the angular frequencies of the pump, the signal, and the idler, respectively. The phase-matching condition can be written as $\vec{k}_p + \vec{G} = \vec{k}_s + \vec{k}_i$. Since the idler k vector is much smaller than the k vectors of the pump and the signal, the phase-matching angles of the PDC x-ray signal are very close to the Bragg angle. Consequently, the tail of the elastic scattering is not negligible, and the separation of the PDC x-ray signal from the elastic requires narrow filters for energy resolution and slits for angular resolution.

Under the assumptions of undepleted pump approximation, lossless medium, and slowly varying envelope approximation (SVEA), the coupled wave equations describing the PDC process in the frequency domain can be described as [13–15]

$$\begin{aligned} \frac{\partial a_s}{\partial z} &= -\kappa a_i^\dagger \exp[i\Delta k_z z], \\ \frac{\partial a_i^\dagger}{\partial z} &= -\kappa^* a_s \exp[-i\Delta k_z z]. \end{aligned} \quad (1)$$

Here, a_s , a_i are signal and idler annihilation operators, $\Delta k_z = k_p \cos \theta_p - k_s \cos \theta_s - k_i \cos \theta_i$ is the phase mismatch, and $\kappa = [(2\hbar\eta_p\eta_s\eta_i\omega_p\omega_s\omega_i)^{\frac{1}{2}} J_s^{NL} / 2\omega_s E_i^* \sqrt{\cos \theta_s \cos \theta_i}]$ is the nonlinear interaction coefficient. We denote η_p , η_s , and η_i as the impedances at the pump, the signal, and the idler frequencies, respectively; \hbar is the reduced Planck constant; E_i is the electric field of the idler; and J_s^{NL} is the nonlinear current density.

The signal count rate is given by

$$R = \iint \kappa^2 \frac{\cos \theta_s \omega_s^2 \sin^2(\frac{1}{2}\Delta k_z z)}{(2\pi)^3 c^2 (\frac{1}{2}\Delta k_z z)^2} d\Omega d\omega_s, \quad (2)$$

where c is the speed of light in vacuum. The signal count rate is calculated numerically, where the integration is taken over the solid angle of the detector and the bandwidth of the analyzer. We note that the acceptance angle of the detector restricts the bandwidth due to the one-to-one relation between the angle of propagation and the wavelength of the generated x-ray signal, which is imposed by the requirement for exact phase matching in the directions parallel to the surface of the crystal.

We conducted the experiments described below at beam line ID-20 of the European Synchrotron Radiation Facility and at beam line I16 of Diamond Light Source [16]. The schematic of the experimental system is shown in Fig 1(b). The average input power is $\sim 1 \times 10^{13}$ photons/s and its polarization is horizontal. The nonlinear crystal is a diamond crystal with dimensions 4 mm \times 4 mm \times 0.8 mm, and the scattering plane is horizontal. We use the reciprocal lattice vector normal to the C(220) atomic planes in a Laue geometry to achieve the phase-matching condition. We use a multibounce Si crystal analyzer and two variable slits in front of and behind the analyzer, which we denote as S_1 and S_2 , to filter out the tail of the elastic diffraction. The analyzer scattering plane is in the vertical direction, which is normal to the scattering plane of the diamond crystal. We measure the PDC x-ray signal with an avalanche photo-diode. All experimental data are corrected for relative intensity fluctuations via measurements from a reference detector positioned upstream from the nonlinear medium.

The first step in the investigation of PDC of x rays into optical radiation is to measure the spectrum of the x-ray signal by scanning the angle of the analyzer crystal. This measurement is used to characterize the dependence of the spectrum of the x-ray signal at a specific offset of the pump angle from the Bragg angle and to explore the possible range of photon energies that can be measured. As an example, Fig. 2 shows the spectrum for a pumping beam at 11 keV, where the phase-matching deviation from the Bragg angle is 43 mdeg and the deviation of the detector angle from the Bragg diffraction is -37 mdeg. The sharp peak on the left corresponds to the elastic scattering, and

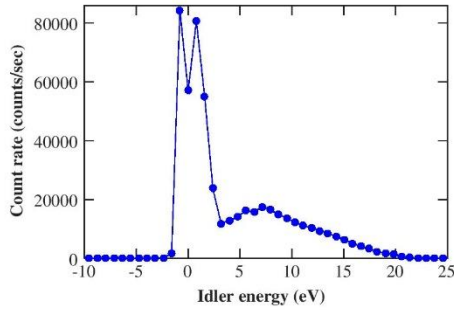


FIG. 2. X-ray signal count rate as a function of the analyzer detuning from the photon energy of the input beam. The sharp peak on the left corresponds to the elastic scattering, and the broad peak is the PDC signal (see text for further details). The solid line is a guide for the eye.

the broad peak is the PDC signal. We observe the broad PDC peak only near the phase-matching condition. The PDC peak position shifts when we vary the angles and vanishes when the angles are off the phase-matching angles. Since we measure the hard x-ray signal (at about 11 keV), and since the deepest electronic level of carbon is at ~ 280 eV, our observation cannot be attributed to x-ray fluorescence. The measured PDC spectrum corresponds to idler wavelengths (energies) in the range of about 60–400 nm (3–21 eV). Since the separation between the elastic signal and the PDC signal is pronounced, we conclude that the background reduction that the analyzer provides is adequate for the measurement of the x-ray signal of PDC into optical wavelengths. The peak is observed at 7.1 eV, where the efficiency of the PDC is the largest. This corresponds to a photon energy above the band gap of the diamond crystal, where the density of states of the valence electrons is probably the highest.

Next, to further support the evidence, we measure the dependence of the x-ray signal of the PDC process on the angular deviation from phase matching. The importance of this measurement is the ability to calculate the Fourier component of the nonlinear susceptibility from the peak of the rocking curve. Figure 3 shows the signal count rate as a function of the pump-deviation angle from the phase-matching angle. The zero of the horizontal axis corresponds to a pump deviation from the Bragg angle of 12 mdeg, which corresponds to the phase-matching angle. The photon energy is 9 keV, and the offset of the detector angle from the Bragg diffraction is 41 mdeg. The small peak on the left is the residual elastic, and the peak centered at 15 mdeg is the PDC signal. This observation of a peak, which is broader than the elastic peak but much narrower than inelastic effects, near the phase-matching condition strongly supports that the effect we observe is indeed PDC of x rays to optical wavelengths. The theoretical curve is obtained from numerical simulations based on Eq. (2), and

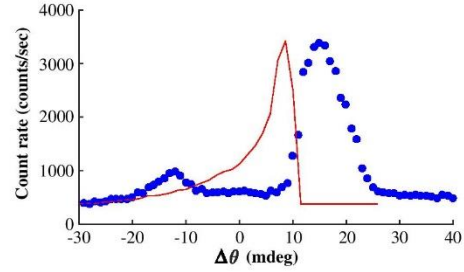


FIG. 3. X-ray signal count rate as a function of the pump-deviation angle from the phase-matching angle. The idler central wavelength is ~ 550 nm (~ 2.2 eV). The blue dots are the experimental results, and the solid red line is calculated from theory and scaled to the peak of the rocking curve.

it is normalized with respect to the experimental PDC peak by a factor of 1.24. The difference between the positions of the calculated and the measured peak, which is only 6 mdeg, is mainly because of the acceptance angle of the detector and the analyzer bandwidth (~ 1 eV), which introduce uncertainties into the values we use in our calculations. These results, together with the dependence of the density of states of the vacuum modes on the angles and frequencies, are the reasons for the deviation of the theoretical peak from the phase-matching value.

Finally, the phase-matching equations have two possible solutions for the angle of the detector, and we expect to be able to observe them experimentally. Indeed, the two solutions are clearly seen in Fig. 4, which shows the signal count rate as a function of the deviation of the angle of the detector with regards to the normal to the crystal surface from the Bragg angle (blue dots). The solid red lines are the simulations, which are obtained by using Eq. (2). The two peaks on the left and on the right of the central peak correspond to the PDC signal. The central peak is the residual elastic scattering. The deviation of the angle of the pump from the Bragg angle is 21 mdeg. The photon energy is 9 keV. The idler central energies in Figs. 4(a)–4(c) are ~ 2.2 , 3.3, and 4.4 eV, respectively. The results of the numerical simulations are scaled to the heights of the peaks of the experimental rocking curves. The ratio between the count rates of the first and the second PDC solution is smaller for higher idler energies in both the experiment and the numerical simulation, and it is a consequence of the product of the nonlinear current density and the density of states. The measured angular separation between the two solutions in panels (a) and (b) agrees remarkably with the simulations. The small difference in the angular separation between the experimental results and the simulations in panel (c) can be attributed to the bandwidth of the analyzer crystal (~ 1 eV) and to the proximity to the band gap of diamond (~ 5.5 eV), which is not considered in our theory.

The measured efficiency is proportional to the absolute square of the Fourier component of the nonlinear

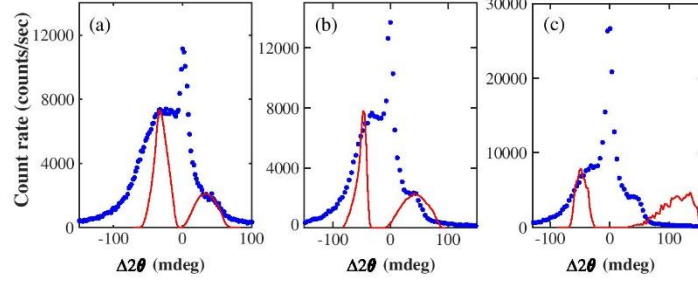


FIG. 4. X-ray signal count rate as a function of the deviation of the detector angle from the residual elastic wave for various idler center photon energies: (a) 2.2-eV idler (~ 550 nm), (b) 3.3-eV idler (~ 400 nm), and (c) 4.4-eV idler (~ 300 nm). The blue dots are the experimental results. The narrow peaks at the center in each of the panels correspond to the residual elastic wave. The peaks to the left and right correspond to the x-ray signal of the PDC for the two solutions of the phase-matching equations. The zero is the angle of the residual elastic wave. The solid red lines are calculated from theory and scaled to the peaks of the rocking curves.

susceptibility, which corresponds to the selected reciprocal lattice vector. We estimate the Fourier component corresponding to the reciprocal lattice vector normal to the C(220) atomic planes of the nonlinear susceptibility by fitting the results of the numerical simulations to the heights of the peaks of the curves in Figs. 3 and 4(a). After subtracting the DC component of the PDC rocking curve, we find that the nonlinear susceptibility for an idler energy of ~ 2.2 eV (~ 550 nm) is $\chi_{(220)}^{(2)} = 2 \times 10^{-17}$ m/V. The nonlinear susceptibility is calculated using the relation $\chi^{(2)} = -0.5ik/\epsilon_0 \sqrt{[\cos\theta_s \cos\theta_i (c\epsilon_0)^3 n_i / 2\hbar\omega_p \omega_s \omega_i]}$, where n_i is the refractive index at the idler wavelength. We note that this result is comparable to the nonlinear susceptibility $\chi_{(111)}^{(2)} = 8 \times 10^{-18}$ m/V, which was obtained in the x-ray and optical mixing experiment [with an x-ray beam at 8 keV and an optical beam at 1.55 eV (800 nm)] [6]. Since the susceptibility is proportional to the Fourier component of the charge density of the valence electrons, the measurements of the efficiencies for various reciprocal lattice vectors can be used for the reconstruction of the charge density of the valence electrons [4].

Before concluding, we discuss several important experimental aspects. We note that, while the full measurement of PDC of x rays into the optical regime should include the measurement of the optical radiation, the measurement of the x-ray photons is sufficient for retrieving microscopic information on the valence electron charge density in a manner similar to PDC of x rays into EUV [4]. In fact, for materials that are opaque at optical wavelengths, the visible radiation is not measureable. Moreover, the numerical simulations that agree with the observations of the x-ray signal predict that the PDC optical idler count rate is 2 orders of magnitude weaker than the optical fluorescence we measured in the experiment (there is no x-ray fluorescence since the deepest electronic binding energy in carbon is ~ 280 eV). The expected idler count rate is much weaker

than the signal count rate because of the large ratio between the x-ray and optical wavelengths, which leads to a high ratio between the density of states of the x-ray and the density of states of the optical wavelengths. In addition, the optical radiation is highly suppressed by internal reflection.

Since the photon energy of the pump can be chosen to be high above the electronic resonances and since the generation and absorption rates of the optical photons are very small, the perturbation of the measured state by x rays into optical PDC is expected to be negligible. This property is essential for measurements of ground states of systems where even small quanta of absorbed light can excite or change the properties of the sample.

In conclusion, we report the observation of the x-ray signal of phase-matched PDC corresponding to optical idler photons at several wavelengths in the range of 280–650 nm. The PDC signal is well above the background, and the separation from the elastic is pronounced. The widths of the rocking curves and the absolute count rates are in agreement with theory. The deviations between the calculated and measured peak positions of the PDC x-ray signal rocking curves are within the uncertainties due to the precision of the motors and the analyzer bandwidth. Our results advance the possibility to use x rays into optical PDC as a new tool to probe microscopic valence charge densities and optical properties of materials on the atomic scale. This novel tool can be used to test and improve the understanding of condensed-matter physics.

We acknowledge the European Synchrotron Radiation Facility for provision of synchrotron radiation facilities. We thank Diamond Light Source for access to Beamline I16 (Proposal No. MT14646), which contributed to the results presented here. This work was supported by the Israel Science Foundation (ISF), Grant No. 1038/13. This research was supported by a Marie Curie FP7 Integration Grant within the 7th European Union Framework Programme under Grant Agreement

No. PCIG13-GA-2013-618118. D. B. gratefully acknowledges support from the Ministry of Aliyah and Immigrant Absorption of Israel. C. B. is supported by the Deutsche Forschungsgemeinschaft (DFG) via SFB925 (Teilprojekt A4), and is thankful for travel support by the Centre for Ultrafast Imaging (CUI) and Partnership for Innovation, Education and Research (PIER) to the ESRF and Diamond Light Sources.

*sharon.shwartz@biu.ac.il

- [1] I. Freund and B. F. Levine, *Phys. Rev. Lett.* **25**, 1241 (1970).
- [2] P. M. Eisenberger and S. L. McCall, *Phys. Rev. A* **3**, 1145 (1971).
- [3] H. Danino and I. Freund, *Phys. Rev. Lett.* **46**, 1127 (1981).
- [4] K. Tamasaku, K. Sawada, E. Nishibori, and T. Ishikawa, *Nat. Phys.* **7**, 705 (2011).
- [5] T. E. Glover, D. M. Fritz, M. Cammarata, T. K. Allison, Sinisa Coh, J. M. Feldkamp, H. Lemke, D. Zhu, Y. Feng, R. N. Coffee, M. Fuchs, S. Ghimire, J. Chen, S. Shwartz, D. A. Reis, S. E. Harris, and J. B. Hastings, *Nature (London)* **488**, 603 (2012).
- [6] K. Tamasaku and T. Ishikawa, *Phys. Rev. Lett.* **98**, 244801 (2007).
- [7] K. Tamasaku and T. Ishikawa, *Acta Crystallogr. Sect. A* **63**, 437 (2007).
- [8] K. Tamasaku, K. Sawada, and T. Ishikawa, *Phys. Rev. Lett.* **103**, 254801 (2009).
- [9] B. Barbiellini, Y. Joly, and K. Tamasaku, *Phys. Rev. B* **92**, 155119 (2015).
- [10] D. Borodin, S. Levy, and S. Shwartz, *Appl. Phys. Lett.* **110**, 131101 (2017).
- [11] E. Shwartz and S. Shwartz, *Opt. Express* **23**, 7471 (2015).
- [12] I. Freund and B. F. Levine, *Phys. Rev. Lett.* **23**, 854 (1969).
- [13] S. Shwartz, R. N. Coffee, J. M. Feldkamp, Y. Feng, J. B. Hastings, G. Y. Yin, and S. E. Harris, *Phys. Rev. Lett.* **109**, 013602 (2012).
- [14] See Supplemental Material at <http://link.aps.org/supplemental/10.1103/PhysRevLett.119.253902> for a more detailed overview of the theory, the numerical simulations, and the experimental setup.
- [15] Additional experimental and theoretical details are given in Ref. [14].
- [16] S. P. Collins, A. Bombardi, A. R. Marshall, J. H. Williams, G. Barlow, A. G. Day, M. R. Pearson, R. J. Woolliscroft, R. D. Walton, G. Beutier, and G. Nisbet, *AIP Conf. Proc.* **1234**, 303 (2010).

Supplementary Material for "Parametric Down Conversion of X-rays into the Optical Regime"

A. Schori¹, C. Bömer², D. Borodin¹, S. P. Collins³, B. Detlefs⁴, M. Moretti Sala⁴, S. Yudovich¹ and S. Shwartz¹

¹Physics Department and Institute of Nanotechnology, Bar Ilan University, Ramat Gan, 52900 Israel

²European XFEL, Holzkoppel 4, 22869 Schenefeld, Germany

³Diamond Light Source, Harwell Science and Innovation Campus, Didcot OX11 0DE, United Kingdom

⁴European Synchrotron Radiation Facility, BP 220, F-38043 Grenoble Cedex, France

Experimental details

We provide further details of the experimental setup and on the procedures that we describe in the main text.

First, we summarize the properties of the experimental systems we use to obtain the results for the various figures of the main text in Table I.

TABLE I. Properties of the experimental systems.

Figure #	S ₁ horizontal, vertical aperture (mm)	S ₂ horizontal, vertical aperture (mm)	d ₁ (mm)	d ₂ (mm)	Acquisition time (sec)
2	1, 0.5	1.2, 10	810	1180	1
3	0.1, 0.5	1.25, 2	615	990	0.5
4(a)	0.1, 0.5	1.25, 2	615	990	0.5
4(b)	0.1, 0.5	1.25, 2	615	990	0.5
4(c)	0.1, 0.5	1.25, 2	615	990	0.5

S₁ is the slit between nonlinear crystal and the analyzer and S₂ is the slit between the analyzer and the detector and the respective distances from the nonlinear crystal are d₁ and d₂.

The monochromator and the analyzer that we used for the results presented in Fig. 2 of the Letter are two-bounce Si(311) and two-bounce Si(440), respectively. The

monochromator and the analyzer that we used for the results presented in Figs. 3 and 4 of the Letter are two-bounce Si(111) and three-bounce Si(111), respectively.

We note that due to the correlation between energies and k-vectors in PDC, which is imposed by the phase matching conditions, the energy resolution of the detection system is determined not only by the energy resolution provided by the analyzer, but also by the angular acceptance of S_1 . We calculate the energy resolution determined by the slit by solving the phase matching equation for different idler energies and determining the energy range of the idler that corresponds to the acceptance angle of the slit. For the calculations, we assume that the center position of the slit corresponds to the central photon energy of the analyzer.

In the measurements described in Fig. 2 of the Letter, the resolution provided by the detection system is determined by the analyzer crystal. In the measurements described in Figs. 3 and 4 of the Letter, the resolution provided by the detection system is determined by the aperture of the S_1 slit. Based on the aperture of the S_1 slit, we estimate the energy resolution of the system in the measurements in Figs. 3 and 4 to be about 0.6 eV.

The experimental and theoretical angular separation ($\Delta 2\theta$) between the two signal solutions in Fig. 4 of the Letter

are summarized in Table II.

TABLE II. Angular separation between the detector angles ($\Delta 2\theta$) of the two solutions of the x-ray signal at various idler photon energies. The pump deviation angle from the Bragg angle is 21 mdeg.

Photon energy (eV)	Experimental $\Delta 2\theta$ (mdeg)	Theoretical $\Delta 2\theta$ (mdeg)
2	76	69
3	88	89
4	96	142

Details of the theoretical calculations

We provide further mathematical description of the wave equation model that we use in our theoretical model.

The nonlinear current density, which we use in our numerical simulations, can be expressed as follows [6]

$$J_s^{\text{NL}}(\omega_p = \omega_s + \omega_i) = \frac{j e E_p E_i^* \chi_G^{(1)}(\omega_i) G \varepsilon_0 \sin \theta_i \cos 2\theta_B}{2 m_e \omega_s}, \quad (\text{A1})$$

where m_e and e are the electron mass and charge, respectively, $\chi_G^{(1)}$ is the linear susceptibility, G is the reciprocal lattice vector orthogonal to the atomic planes, θ_i is the idler angle with respect to the atomic planes, ω_p , ω_s , and ω_i , are the angular frequencies of the pump, the signal and the idler, respectively, θ_B is the Bragg angle, ε_0 is the vacuum permittivity, and E_p and E_i are the electrical fields of the pump and idler, respectively.

The time-space signal and idler operators are related to their frequency domain counterparts by

$$\begin{aligned} a_s(z, \mathbf{r}, t) &= \int_0^\infty \int_{-\infty}^\infty a_s(z, \mathbf{q}, \omega) [-i(\mathbf{q} \cdot \mathbf{r} - \omega t)] d\mathbf{q} d\omega \\ a_i(z, \mathbf{r}, t) &= \int_0^\infty \int_{-\infty}^\infty a_i(z, \mathbf{q}, \omega) [-i(\mathbf{q} \cdot \mathbf{r} - \omega t)] d\mathbf{q} d\omega \end{aligned}, \quad (\text{A2})$$

where $\mathbf{r} = (x, y)$. The commutation relations for the signal and idler operators are

$$[a_j(z_1, \mathbf{q}_1, \omega_1), a_k^\dagger(z_2, \mathbf{q}_2, \omega_2)] = \frac{1}{(2\pi)^3} \delta(z_1 - z_2) \delta(\mathbf{q}_1 - \mathbf{q}_2) \delta(\omega_1 - \omega_2), \quad (\text{A3})$$

Here $\mathbf{q}_j = (k_{jx}, k_{jy})$, where k_{jx} and k_{jy} represent the k wave-vector components parallel to the surfaces of the crystal. The signal count rate is given by $\langle a_s^\dagger(z, \mathbf{r}_2, t_2) a_s(z, \mathbf{r}_1, t_1) \rangle$.

Simulation details

The parameters of the simulations that lead to the theoretical results corresponding to Figs. 3 and 4 of the Letter are the horizontal and vertical detector acceptance angles of 0.16 and 2 mrad, respectively, and an analyzer width of 1.98 eV. We note that the analyzer acceptance angle is taken to be larger than the full-width at half maximum (FWHM).

8. Conclusions and outlook

This work described the observations of several promising imaging and spectroscopy methods at X-ray wavelengths. These methods have been demonstrated several decades ago at optical wavelengths. The extension to the X ray regime offers clear advantages that stem from the inherent properties of X rays, such as spatial resolution at the atomic scale, high penetration depth, very low beam divergence, and commercially available detectors with low noise and with photon-number-resolving capabilities.

The first experiment described in **chapter 4** is my observation of classical (thermal) ghost imaging with a low brightness laboratory source. The effect was demonstrated by imaging slits with a scanning resolution as fine as 2- μm and with high contrast. The high contrast results and the potential of this method to observe phase information [64] suggest that this method may be applied to the fields of medical imaging similar to computed tomography and to security scanners similar to the systems that are used in airports. More recent works at the X-ray regime have observed this effect with two-dimensional complex objects [65,66] and even computational ghost imaging was demonstrated [67]. An extension of the ghost imaging to high order ghost imaging and the application of image processing algorithms, such as sparsity constraint, can be applied to improve the spatial resolution and to decrease the radiation dose [10]. Of particular interest is the possibility to perform ghost diffraction measurements with X-ray laboratory sources and image at a spatial resolution that is much higher than the spatial resolution of the state-of-the-art cameras.

Next, I described my observation of ghost imaging with paired X-ray photons in **chapter 5**. The results are the first demonstration of an application of X-ray pairs that are generated by the process of PDC since the observation of the process about half a century ago [51]. The results of my experiment demonstrate imaging of slits with a negligible background and with a few photons. The results are fundamentally different from classical ghost imaging in the sense that the source of the correlations of ghost imaging with paired X-ray photons stems from quantum entanglement between the photon pairs [68]. The anti-correlations properties that are demonstrated suggest that this scheme can be used for the observation of a large variety of quantum optics effects, such as single heralded photons [22] and two-photon X-ray diffraction [37]. The measurement of the signal and idler photons without coincidences may lead to sub-shot noise measurements as has been demonstrated at optical wavelengths [35]. The

consequence of sub-shot noise measurements that require very few photons is an extremely low radiation dose of X-rays.

The third experiment that I described in **chapter 7** is a new nonlinear spectroscopic method for probing the microscopic valence charge densities and the optical properties of materials with the atomic scale resolution. I demonstrated the method by measuring the X-ray signal of phase matched parametric down-conversion corresponding to optical idler photons at several wavelengths in the range of 280-650 nm. The nonlinear susceptibility that I calculated from the X-ray signal for an idler energy of ~ 2.2 eV (~ 550 nm) demonstrates the potential of this method as a nonlinear spectroscopic method. I obtained the results by using synchrotron radiation and with a diamond crystal. The method has since been reproduced in several other crystals such as Silicon, LiNbO₃, and GaAs and has even been observed for idler energies of a few eV with a laboratory source by our group [57,69,70]. Hence, the method presented in this work is reproducible, applicable to a variety of materials, and is readily available. This is in contrast to optical mixing with sum-frequency generation that requires an X-ray free electron laser and cannot be applied to materials that are opaque, such as metals and superconductors, or to materials with a low optical damage threshold. Of importance, since the photon energy of the pump is well above the electronic resonances and since the generation and absorption rates of the optical photons are very small, the perturbation of the measured state by X-ray into optical PDC is expected to be negligible. Hence, it may be possible to probe the ground states of samples that are sensitive to excitation. The results can lead to the measurement of the X-ray and optical photons coincidences, and hence to radiation-free X-ray ghost imaging with highly non-degenerate entangled photon pairs [71]. The method I presented has the potential to probe the optical properties of valence electrons of a large range of materials, for example compounds, biological samples, such as proteins, the bond charges of molecules, and the investigation of phenomena that are associated with energies near the Fermi energy of metals or near the band gap of semiconductors.

Finally, I described the experiment of ghost diffraction with a low brightness laboratory source in **chapter 6**. This is the first demonstration of the diffraction of non-periodical objects with an X-ray laboratory source. While the results presented in this section are preliminary and the resolution of the object that was imaged is about 1 μm , an extension of this method can lead to nanoscale-resolution imaging with laboratory sources that could be advantageous to a variety of fields of research and industry. This important goal can be achieved by using a two-dimensional detector, the design of more suitable

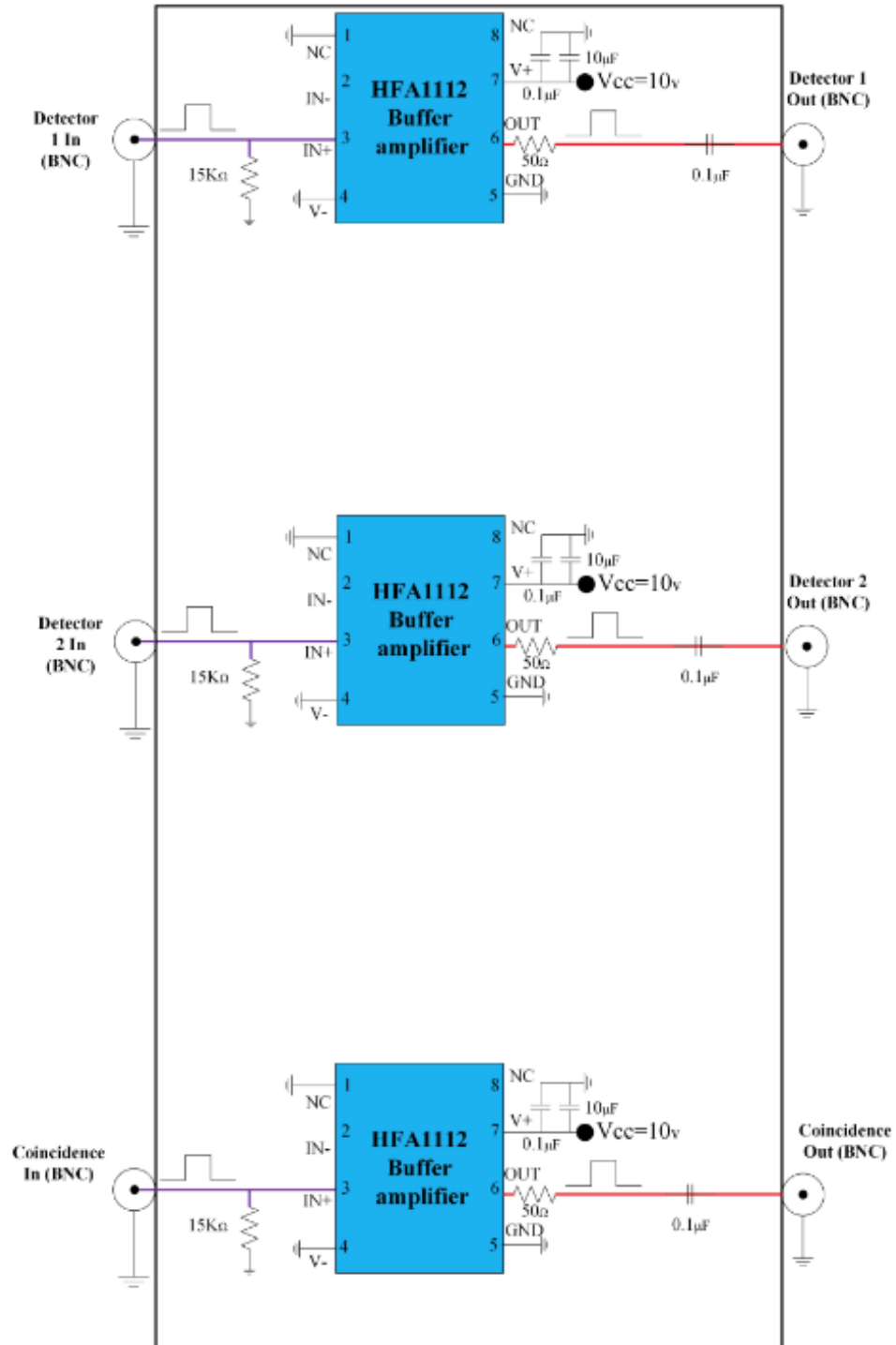
diffusers in terms of effective speckle size and modulation, and focusing the beam with a multi-layer mirror to reduce the measurement times.

In conclusion, I presented the observation of imaging and nonlinear spectroscopy methods with X-rays. I described the first observations of incoherent X-ray ghost imaging with a laboratory source. I then described the first the experimental observations of ghost imaging with paired X-ray photons, which are generated by parametric down-conversion. I continued to describe the first observations of incoherent X-ray ghost diffraction with a laboratory source. Finally, I described the first demonstrations of parametrically down-converted X-ray into optical wavelengths.

I note that in addition to the results presented in this thesis I participated in several synchrotron experiments led by other members of our group [48,67,72].

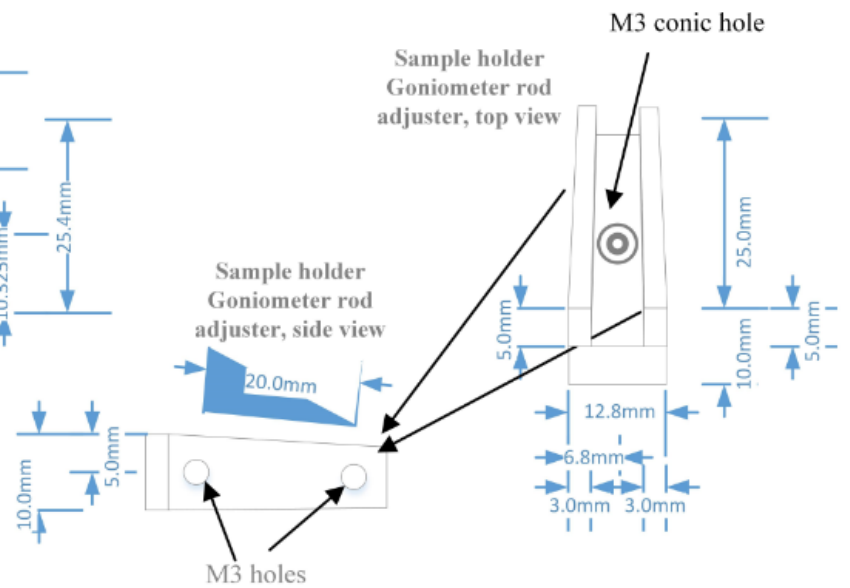
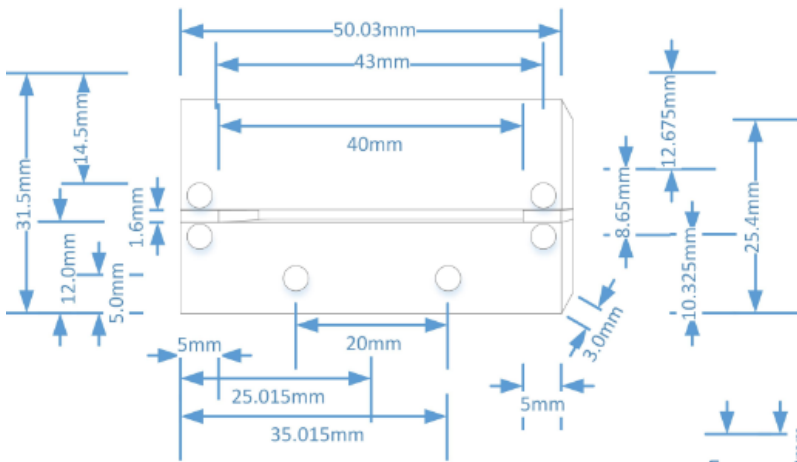
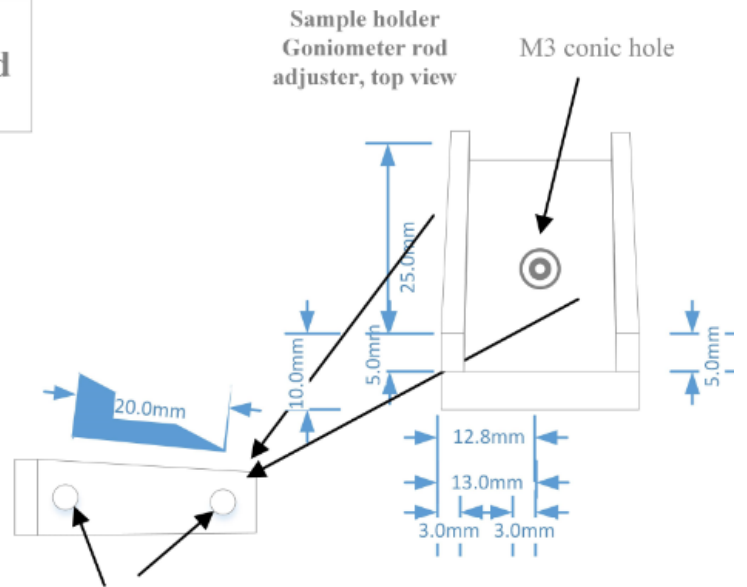
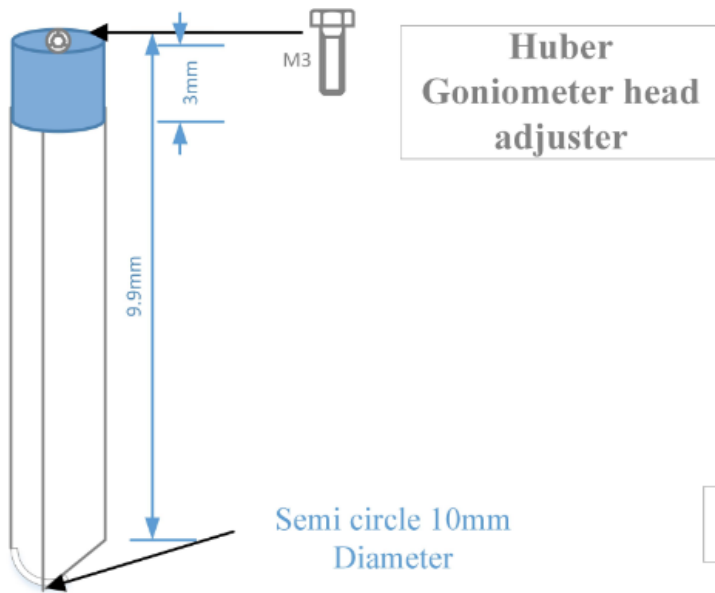
Coincidence buffer-amplifiers circuit

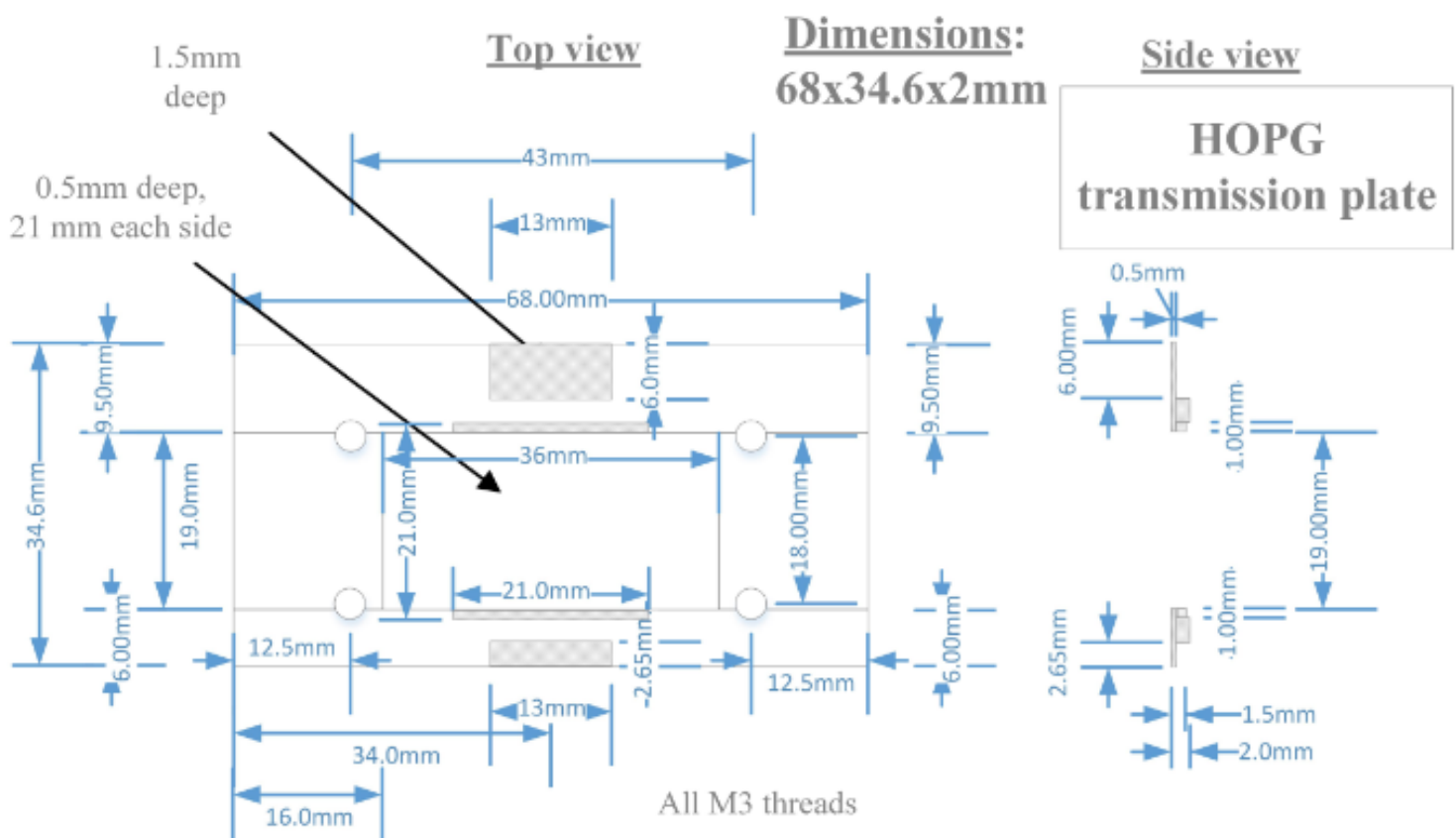
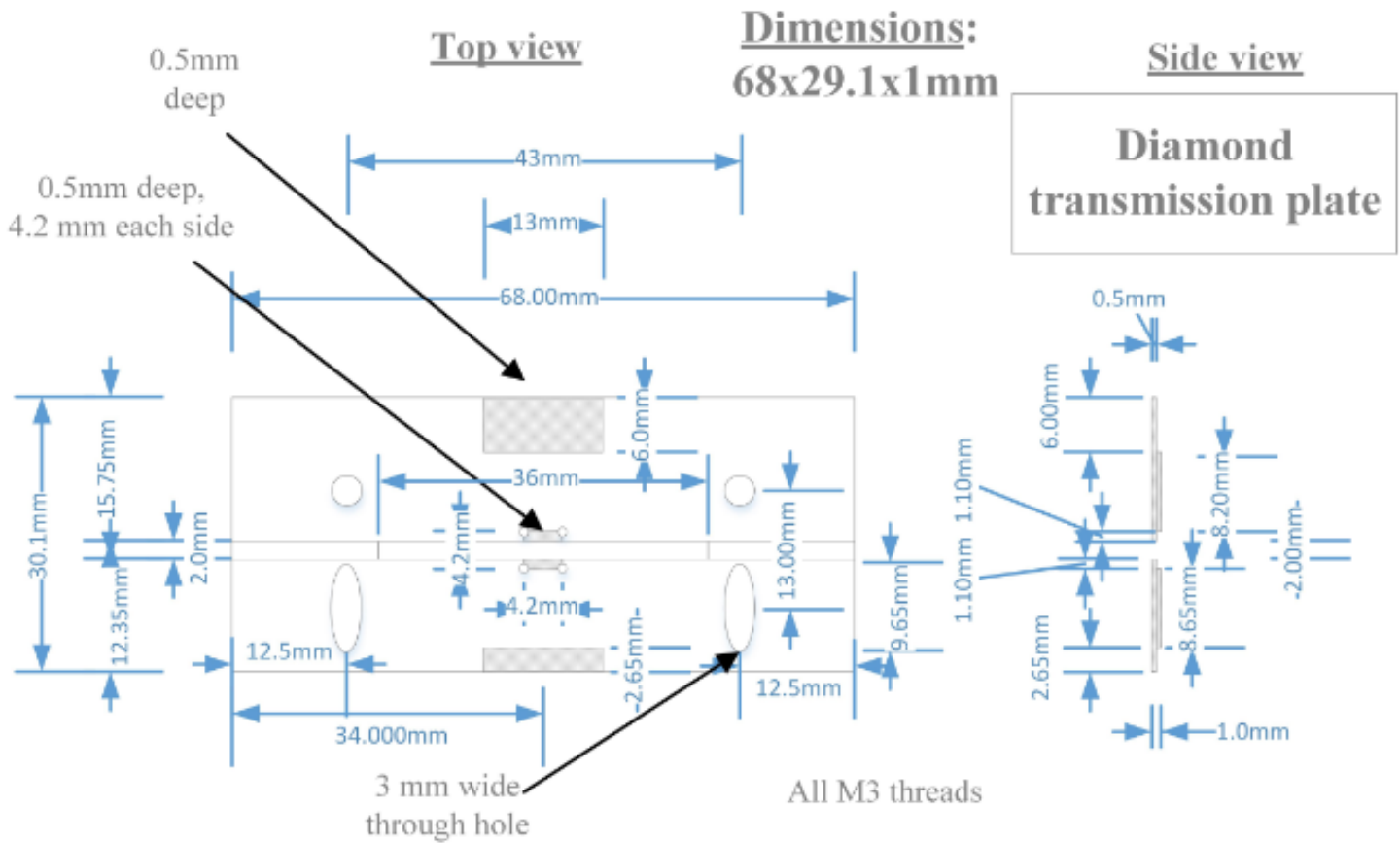
From
Coincidence
circuit



To
NI
USB-6341
DAQ

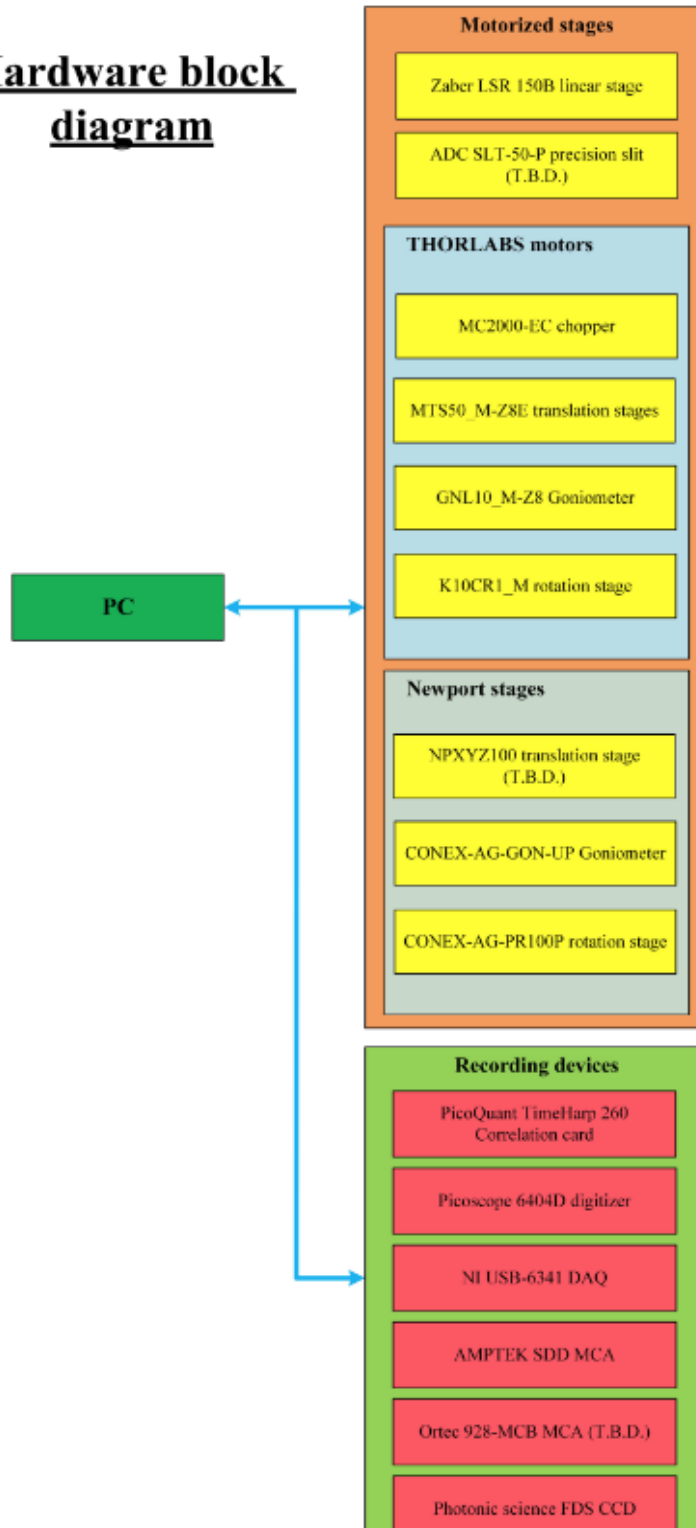
Appendix B – Mechanical schematics – Sample holders





Appendix C – Software description
Appendix C1 – Experiment control software

Hardware block diagram

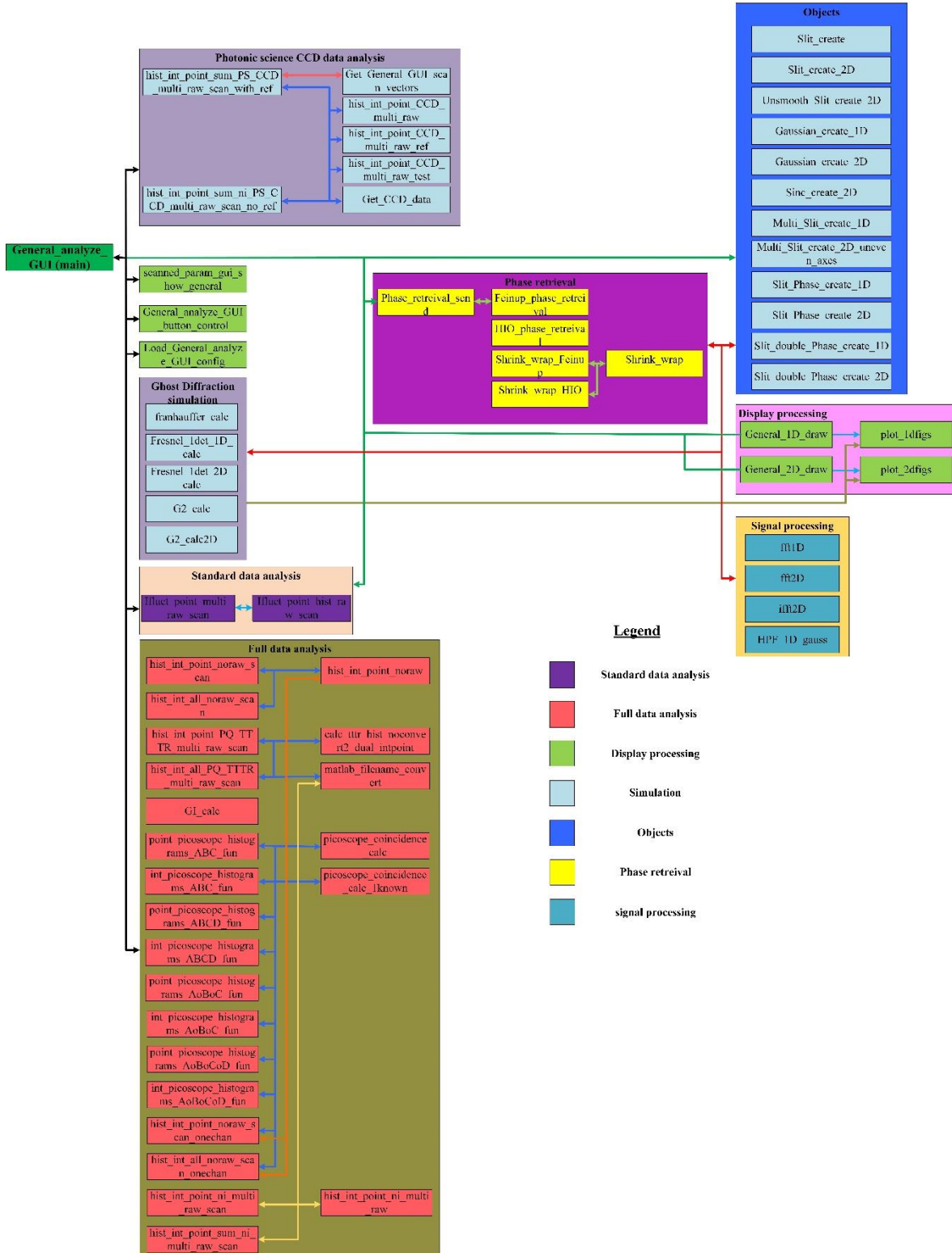


Software block diagram



Appendix C2 – Analysis software

Software block diagram



Bibliography

1. F. Ferri, D. Magatti, V. G. Sala, and A. Gatti, "*Longitudinal coherence in thermal ghost imaging*", Appl. Phys. Lett. **92**, 261109 (2008).
2. P. Ryczkowski, M. Barbier, A. T. Friberg, J. M. Dudley, and G. Genty, "*Ghost imaging in the time domain*", Nat. Photonics **10**, 167–170 (2016).
3. M. I. Kolobov, *Quantum Imaging* (Springer Science + Business Media, 2007).
4. F. Ferri, D. Magatti, A. Gatti, M. Bache, E. Brambilla, and L. A. Lugiato, "*High-resolution ghost image and ghost diffraction experiments with thermal light*", Phys. Rev. Lett. **94**, 183602 (2005).
5. X. F. Liu, X. H. Chen, X. R. Yao, W. K. Yu, G. J. Zhai, and L. A. Wu, "*Lensless ghost imaging with sunlight*", Opt. Lett. **39**, 2314–2317 (2014).
6. T. B. Pittman, Y. H. Shih, D. V. Strekalov, and A. V. Sergienko, "*Optical imaging by means of two-photon quantum entanglement*", Phys. Rev. A **52**, R3429–R3432 (1995).
7. P. A. Morris, R. S. Aspden, J. E. Bell, R. W. Boyd, and M. J. Padgett, "*Imaging with a small number of photons*", Nat. Commun. **6**, 5913 (2015).
8. R. S. Bennink, S. J. Bentley, and R. W. Boyd, "*“Two-Photon” coincidence imaging with a classical source*", Phys. Rev. Lett. **89**, 113601 (2002).
9. B. Sun, M. P. Edgar, R. Bowman, L. E. Vittert, S. Welsh, A. Bowman, and M. J. Padgett, "*3D computational imaging with single-pixel detectors*", Science **340**, 844–847 (2013).
10. W. Gong and S. Han, "*High-resolution far-field ghost imaging via sparsity constraint*", Sci. Rep. **5**, 9280 (2015).
11. F. Ferri, D. Magatti, L. A. Lugiato, and A. Gatti, "*Differential ghost imaging*", Phys. Rev. Lett. **104**, 253603 (2010).
12. K. W. C. Chan, M. N. O’Sullivan, and R. W. Boyd, "*High-order thermal ghost imaging*", Opt. Lett. **34**, 3343–3345 (2009).
13. M. Bina, D. Magatti, M. Molteni, A. Gatti, L. A. Lugiato, and F. Ferri, "*Backscattering differential ghost imaging in turbid media*", Phys. Rev. Lett. **110**, 083901 (2013).
14. P. Zerom, Z. Shi, M. N. O’Sullivan, K. W. C. Chan, M. Krogstad, J. H. Shapiro, and R. W. Boyd, "*Thermal ghost imaging with averaged speckle patterns*", Phys. Rev. A **86**, 063817 (2012).
15. J. H. Shapiro, *Computational ghost imaging*", Phys. Rev. A **78**, 061802 (2008).

16. S. Oppel, R. Wiegner, G. S. Agarwal, and J. von Zanthier, "*Directional superradiant emission from statistically independent incoherent nonclassical and classical sources*", Phys. Rev. Lett. **113**, 263606 (2014).
17. C. Thiel, T. Bastin, J. Martin, E. Solano, J. von Zanthier, and G. S. Agarwal, "*Quantum imaging with incoherent photons*", Phys. Rev. Lett. **99**, 133603 (2007).
18. L. Basano and P. Ottonello, "*Ghost imaging: open secrets and puzzles for undergraduates*", Am. J. Phys. **75**, 343–351 (2007).
19. Y. Bromberg, O. Katz, and Y. Silberberg, "*Ghost imaging with a single detector*", Phys. Rev. A **79**, 053840 (2009).
20. H. Liu, X. Shen, D. Zhu, and S. Han, "*Fourier-transform ghost imaging with pure far-field correlated thermal light*", Phys. Rev. A **76**, 053808 (2007).
21. R. S. Aspden, Nathan R. Gemmell, P. A. Morris, D. S. Tasca, L. Mertens, M. G. Tanner, R. A. Kirkwood, A. Ruggeri, A. Tosi, R. W. Boyd, G. S. Buller, R. H. Hadfield, and M. J. Padgett, Optica **2**, "*Photon-sparse microscopy: visible light imaging using infrared illumination*" ,1049 (2015).
22. F. Kaneda, B. G. Christensen, J. J. Wong, H. S. Park, K. T. McCusker, and P. G. Kwiat, "*Time-multiplexed heralded single-photon source*" ,Optica **2**, 1010 (2015).
23. M. N. O’Sullivan, K. W. C. Chan, and R. W. Boyd, "*Comparison of the signal-to-noise characteristics of quantum versus thermal ghost imaging*" ,Phys. Rev. A **82**, 053803 (2010).
24. R. I. Khakimov, B. M. Henson, D. K. Shin, S. S. Hodgman, R. G. Dall, K. G. H. Baldwin, and A. G. Truscott, "*Ghost imaging with atoms*", Nature **540**, 100–103 (2016).
25. H. N. Chapman and K. A. Nugent, "*Coherent lenseless X-ray imaging*", Nat. Photonics, **4**, 833–839 (2010).
26. J. Miao, P. Charalambous, J. Kirz, and D. Sayre, "*Extending the methodology of X-ray crystallography to allow imaging of micrometre-sized non-crystalline specimens*", Nature **400**, 342–344 (1999).
27. I. McNulty, J. Kirz, C. Jacobsen, E. H. Anderson, M. R. Howells, and D. P. Kern, "*High-resolution imaging by Fourier transform X-ray holography*", Science **256**, 1009–1012 (1992).
28. F. Pfeiffer, T. Weitkamp, O. Bunk, and C. David, "*Phase retrieval and differential phase-contrast imaging with low-brilliance X-ray sources*", Nat. Phys. **2**, 258–261 (2006).

29. J. Cheng and S. Han, "*Incoherent coincidence imaging and its applicability in X-ray diffraction*", Phys. Rev. Lett., **92**, 093903 (2004).
30. D. Pelliccia, A. Rack, M. Scheel, V. Cantelli, and D. M. Paganin, "*Experimental X-ray ghost imaging*", Phys. Rev. Lett. **117**, 113902 (2016).
31. H. Yu, R. Lu, S. Han, H. Xie, G. Du, T. Xiao, and D. Zhu, "*Fourier-transform ghost imaging with hard X rays*", Phys. Rev. Lett. **117**, 113901 (2016).
32. G. B. Lemos, V. Borish, G. D. Cole, S. Ramelow, R. Lapkiewicz, and A. Zeilinger, "*Quantum imaging with undetected photons*", Nature **512**, 409 (2014).
33. G. Brida, M. Genovese, and I. R. Berchera, "*Experimental realization of sub-shot-noise quantum imaging*", Nat. Photonics **4**, 227 (2010).
34. J. C. Howell, R. S. Bennink, S. J. Bentley, and R.W. Boyd, "*Realization of the Einstein-Podolsky-Rosen Paradox Using Momentum- and Position-Entangled Photons from Spontaneous Parametric Down Conversion*", Phys. Rev. Lett. **92**, 210403 (2004).
35. S.A. Castelletto and R.E. Scholten, "*Heralded single photon sources: a route towards quantum communication technology and photon standards*", Eur. Phys. J. Appl. Phys. **41**, 181-194 (2008).
36. M. D. Eisaman, J. Fan, A. Migdall, and S. V. Polyakov, "*Invited Review Article: Single-photon sources and detectors*", Rev. Sci. Instrum. **82**, 071101 (2011).
37. J. Stöhr, "*Two-Photon X-Ray Diffraction*", Phys. Rev. Lett. **118**, 024801 (2017).
38. I. Freund and B. F. Levine, "*Optically modulated X-ray diffraction*", Phys. Rev. Lett. **25**, 1241-1245 (1970).
39. P. M. Eisenberger and S. L. McCall, "*Mixing of X-ray and optical photons*", Phys. Rev. A **3**, 1145-1151 (1971).
40. H. Danino and I. Freund, "*Parametric down conversion of X rays into the extreme ultraviolet*", Phys. Rev. Lett. **46**, 1127-1130 (1981).
41. K. Tamasaku, K. Sawada, E. Nishibori, and T. Ishikawa, "*Visualizing the local optical response to extreme-ultraviolet radiation with a resolution of $\lambda/380$* ", Nat. Phys. **7**, 705-708 (2011).
42. B. Barbiellini, Y. Joly, and K. Tamasaku, "*Explaining the X-ray nonlinear susceptibility of diamond and silicon near absorption edges*", Phys. Rev. B **92**, 155119 (2015).
43. D. Borodin, S. Levy, and S. Shwartz, "*High energy-resolution measurements of X-ray into ultraviolet parametric down-conversion with an X-ray tube source*", App. Phys. Lett. **110**, 131101 (2017).

44. K. Tamasaku and T. Ishikawa, "*Interference between Compton scattering and X-ray parametric down-conversion*", Phys. Rev. Lett. **98**, 244801 (2007).
45. K. Tamasaku, K. Sawada, and T. Ishikawa, "*Determining X-ray nonlinear susceptibility of diamond by the optical Fano effect*", Phys. Rev. Lett. **103**, 254801 (2009).
46. T. E. Glover, D. M. Fritz, M. Cammarata, T. K. Allison, Sinisa Coh, J. M. Feldkamp, H. Lemke, D. Zhu, Y. Feng, R. N. Coffee, M. Fuchs, S. Ghimire, J. Chen, S. Schwartz, D. A. Reis, S. E. Harris, and J. B. Hastings, "*X-ray and optical wave mixing*", Nature **488**, 603–607 (2012).
47. S. Schwartz, M. Fuchs, J. B. Hastings, Y. Inubushi, T. Ishikawa, T. Katayama, D. A. Reis, T. Sato, K. Tono, M. Yabashi, S. Yudovich, and S. E. Harris, "*X-Ray Second Harmonic Generation*", Physical Review Letters **112**, 163901 (2014).
48. D. Borodin, A. Schori, F. Zontone, and S. Schwartz, "*X-ray photon pairs with highly suppressed background*", Phys. Rev. A **94**, 013843 (2016).
49. S. Schwartz, R. N. Coffee, J. M. Feldkamp, Y. Feng, J. B. Hastings, G. Y. Yin, and S. E. Harris, "*X-ray Parametric down-conversion in the Langevin regime*", Phys. Rev. Lett. **109**, 013602 (2012).
50. E. Schwartz and S. Schwartz, "*Difference-frequency generation of optical radiation from two-color X-ray pulses*", Opt. express **23**, 226995 (2015).
51. P. Eisenberger and S. L. McCall, "*X-ray parametric conversion*", Phys. Rev. Lett. **26**, 684–688 (1971).
52. Y. Yoda, T. Suzuki, X. W. Zhang, K. Hirano, and S. Kikuta, "*X-ray parametric scattering by a diamond crystal*", J. Synchrotron Rad. **5**, 980 (1998).
53. B.W. Adams, Nonlinear Optics, Quantum Optics, and Ultrafast Phenomena with X-Rays (Kluwer Academic Publisher, Norwell, MA, 2008).
54. S. Schwartz and S. E. Harris, "*Polarization Entangled Photons at X-Ray Energies*", Phys. Rev. Lett. **106**, 080501 (2011).
55. I. Freund and B. F. Levine, "*Parametric conversion of X rays*", Phys. Rev. Lett. **23**, 854-857 (1969).
56. Y. R. Shen, "*The principles of nonlinear optics*" (Third edition, Wiley-Interscience, Hoboken 2003).
57. Edward Strizhevsky, Ms.c thesis, in preparation (2018).
58. Sharon Schwartz, ESRF ID20 beamtime proposal #HC-3473 (2017).
59. Sharon Schwartz, Diamond Light source I16 beamtime proposal #MT17527-1 (2017).

60. Sason Sofer, Msc. thesis proposal (2018).
61. Aviad Schori, General scan program Software Design Description rev. 0.3 (2018).
62. Aviad Schori, General analyze program Software Design Description rev. 0.2 (2018).
63. M. Tamura, T. Kitanaka, Y. Nakagawa, and K. Tomishige, "*Cu Sub-Nanoparticles on Cu/CeO₂ as an Effective Catalyst for Methanol Synthesis from Organic Carbonate by Hydrogenation*", ACS Catalysis **6**, 376-380 (2016).
64. T. Shirai, T. Setälä, and Ari T. Friberg, "*Ghost imaging of phase objects with classical incoherent light*", Phys. Rev. A **84**, 041801(R) (2011).
65. A. Zhang, Y. He, L. Wu, L. Chen, and B. Wang, "Tabletop x-ray ghost imaging with ultra-low radiation", Optica **5**, 374-377 (2018).
66. D. Pelliccia, M. P. Olbinado, A. Rack, and D. M. Paganin, "*Practical x-ray ghost imaging with synchrotron light*", Arxiv:1710.00727.
67. Y. Klein, A. Schori, I. Dolbnya, K. Sawhney, and S. Shwartz, "*Computational ghost imaging with X-rays*", Opt. Exp., In preparation (2018).
68. M. O. Scully and M. S. Zubairy, *Quantum Optics* (Cambridge university press, Cambridge, 1997).
69. O. Sefi, PDC LiNbO₃ Beamtime report, 09.17.
70. S. Sofer, PDC GaAs Beamtime report, 01.17.
71. Z. Li, N. Medvedev, H. N. Chapman, and Y. Shih, "*Radiation damage free ghost diffraction with atomic resolution*", J. Phys. B: At. Mol. Opt. Phys. **51**, 025503 (2018).
72. S. Shwartz, ESRF ID20 beamtime report #HC-3181 (2017).
73. J. Miao, D. Sayre, and H. N. Chapman, "*Phase retrieval from the magnitude of the Fourier transforms of nonperiodic objects*", J. Opt. Soc. Am. **15**, 1662-1669 (1998).
74. S. Marchesini, H. He, H. N. Chapman, S. P. Hau-Riege, A. Noy, M.R. Howells, U. Weierstall, and J. C. H. Spence, "*X-ray image reconstruction from a diffraction pattern alone*", Phys. Rev. B **68**, 140101 (2003).
75. L. Mandel and E. Wolf, *Optical Coherence* (Cambridge University Press, 2013).

תוכן העניינים

i.....	תקציר אנגלי.....
1.....	1. הקדמה
1.....	1.1 מבנה העבודה
1.....	1.2 מוטיבציה ומטרות
4.....	1.3 רקע
9.....	2. מודלים תיאורטיים
10.....	2.1 המרת תדר פרמטרית
19.....	2.2 הדמית רפאים ועקיפת רפאים
27.....	3. שיטות מחקר
27.....	3.1 המערכת הנסיונית
30.....	3.2 תוכנות בקרה וניתוח נתונים
31.....	4. מאמר: הדמיית רפאים תרמית עם מקור מעבדתי של קרינת רנטגן
41.....	5. הדמית רפאים עם זוגות פוטונים מתואמים של קרינת רנטגן
61.....	6. עקיפת רפאים תרמית עם מקור מעבדתי של קרינת רנטגן
73.....	7. מאמר: המרת תדר פרמטרית של קרינת רנטגן לתדרים אופטיים
85.....	8. סיכום ומסקנות
89.....	9. נספחים
97.....	ביבליוגרפיה
א.....	תקציר

תקציר

בעבודת המחקר של הדוקטורט אני מציג גישות חדשניות בתחומי ההדמיה וספקטרוסופיה לא ליניארית באמצעות קרינת רנטגן. (1) אני מתאר את ההדגמה הראשונה של המרת תדר פרמטרית של קרינת רנטגן לתדרים אופטיים. שיטה זו יכולה לאפשר חקירה של מטעני ערכיות ברזולוציה אטומית. (2) אני מתאר את ההדגמה הראשונה של הדמיית רפאים לא קוהרנטית באמצעות מקור מעבדתי של קרינת רנטגן, שיכולה לקדם את האפשרות למדידות ברזולוציות גבוהות של עקיפת רפאים עם מקורות קרינת רנטגן שולחניים. (3) אני מתאר את ההדגמה הראשונה של עקיפת רפאים עם מקור מעבדתי. ההרחבה של ההליך שלנו יכולה להוביל להדמיה ברזולוציה נאנו-מטרית עם מקורות מעבדתיים ואי לכך היא שימושית למגוון תחומים במחקר ובתעשייה. (4) אני מתאר את ההדגמה הראשונה של הדמיית רפאים עם זוגות פוטונים של קרינת רנטגן, שנוצרים באמצעות התהליך של המרת תדר פרמטרית. ההרחבה של ההליך המוצג יכולה לשמש להבחנה בתופעות קוונטיות של קרינת רנטגן ולהדמיה ללא קרינה מייננת.

החלק הראשון של עבודת הדוקטורט שלי מפרט עבודה נסיונית ליישום שיטות הדמית רפאים ועקיפת רפאים באמצעות קרינת רנטגן. הדמית רפאים ועקיפת רפאים הינן שיטות הדמיה, שבהן בניית דמות העצם מתקבלת על ידי שימוש במתאם העוצמות המרחבי בין שתי אלומות. אחת האלומות עוברת דרך העצם ונאספת על-ידי גלאי עם פיקסל יחיד ואילו האלומה השנייה נאספת על-ידי גלאי רב-פיקסלים. ישנם שני מקורות עיקריים למתאם המרחבי. המקור הראשון ידוע כהדמיית רפאים לא קוהרנטית (או קלאסית) ומקורה בהוספת תנודות בעוצמה למקור ובפיצול אלומת המקור לשתי אלומות עם תנודות עוצמה זהות. המקור השני נודע כהדמיית רפאים קוונטית ומבוסס על מתאם של זוגות פוטונים. שיטת הדמיית הרפאים מבוססת על גילוי בשדה קרוב ועל שחזור דמות העצם מהמתאם המרחבי. הגילוי של עקיפת רפאים מבוצע בשדה הרחוק ותבנית ההתאבכות של העצם היא שנמדדת.

השימוש של עדשות להדמיה באמצעות קרינת רנטגן מוגבל מאוד עקב ההגדלה והמפתח הקטנים שלהן ואי לכך ובהתאם נעשה שימוש מקיף בשיטות הדמיה ללא עדשות [25-25]. אף על פי כן, הודגמה הדמיה ברזולוציה נאנו-מטרית באמצעות קרינת רנטגן קוהרנטית, שנוצרת באמצעות מתקני לייזרי אלקטרוניים חופשיים של קרינת רנטגן וסינכרוטרוניים [25]. הדמית רנטגן באמצעות מקורות לא קוהרנטיים עם בהירות נמוכה נעשית לרוב על-ידי מדידות ישירות של הבליעה ועם הגדלה נמוכה או ללא הגדלה בכלל. לכן, למרות

שהמידע על הפאזות של עצמים יכול לשפר את הניגודיות של עצמים, מידה זו נמדדת לעיתים רחוקות במערכות, המבוססות על מקורות לא קוהרנטיים, והרזולוציה של מערכות אילו אינה קטנה מגודל הפיקסל של המצלמה. הדמיית רפאים ועקיפת רפאים הינן שיטות מבטיחות להדמיה באמצעות קרינת רנטגן היות ואינן דורשות מקורות קוהרנטיים בהירים או עדשות ולכן יכולות להוביל למדידות ברזולוציה ובניגודיות גבוהים, הניתנות ליישום עם מקורות קרינת רנטגן בעלות נמוכה [29].

היות והמקור של הדמית רפאים ועקיפת רפאים לא קוהרנטיים מבוסס על תנודות עוצמה מרחביות, הדמות משוחזרת באמצעות פונקציית המתאם המיידית מסדר שני של העוצמה, הנמדדת עבור ריאליזציות שונות של תנודות העוצמה של המקור [1]. השיטות נחקרו באופן יסודי בתדרים אופטיים [1-23] ולאחרונה הודגמו הדמיית רפאים עם אטומים [24] והדמיית רפאים זמנית [2].

הדמיית רפאים ועקיפת רפאים לא קוהרנטיים של קרינת רנטגן הודגמו נסיונית באמצעות קרינת סינכורטרון, שמקורה במאיצים גדולים [30,31]. למרות שהדגמות אילו מקדמות משמעותית את הרחבת הדמית רפאים ועקיפת רפאים לקרינת רנטגן, המקורות בהם נעשה שימוש אינם מקורות שולחניים. בחלק נוסף של עבודת המחקר שלי, אני מדווח על המדידה הראשונה של הדמיית רפאים תרמית עם מקור מעבדתי של קרינת רנטגן. אני מתאר ניסויים שמדגימים את האפשרות לשחזר את הדמות של סדקים עם ניגודיות גבוהה באמצעות מקורות קרינת רנטגן לא קוהרנטיים. התוצאות מקדמות את האפשרויות, שהשיטה בעלת הרזולוציה הגבוהה של עקיפת רפאים תודגם באמצעות מקורות קרינת רנטגן שולחניים.

היות והגילוי של עקיפת רפאים נעשה בשדה הרחוק [3,4,10,20,29,31] לשיטה זו יתרון מובהק, כיוון שהיא אינה מוגבלת על-ידי הרזולוציה המרחבית של הגלאי. לכן, להדגמת השיטה באמצעות מקור קרינת רנטגן עם בהירות נמוכה פוטנציאל משמעותי כשיטה להדמיה ברזולוציה גבוהה עם מקורות קרינת רנטגן מעבדתיים. בחלק נוסף של עבודת הדוקטורט שלי אני מציג את ההדגמה הראשונה של עקיפת רפאים תרמית עם מקור מעבדתי של קרינת רנטגן. אני מציג תוצאות ראשוניות של ניסויים, שמקדמים את האפשרות לשחזר דמויות ברזולוציות גבוהות באמצעות מקורות קרינת רנטגן לא קוהרנטיים.

עוד מקור חשוב להדמיית רפאים הינו זוגות פוטונים מתואמים. המקור מיושם בהרבה סכימות בתדרים אופטיים באמצעות התהליך הלא-ליניארי של המרת תדר פרמטרית. אפקט זה הינו אחד מהמקורות העיקריים ליצירת מצבים של קלאסיים של אור ומשמש לחקר תופעות קוואנטיות בסיסיות בתדרים אופטיים [32-37]. הזמינות של גלאי קרינת רנטגן מסחריים עם יכולות הבחנה במספר הפוטונים ועם יעילות קוואנטית,

השואפת לאחד, הינה אטרקטיבית לבחינת מושגים של פיסיקת הקוואנטים ובכדי להתגבר על האתגרים הבסיסיים של אופטיקה קוואנטית קונבנציונלית בתדרים אופטיים. כיוון שעד היום טרם הודגם אף יישום של זוגות פוטונים של המרת תדר פרמטרית של קרינת רנטגן וכיוון שהסכימות של מספר רב של ניסויים באופטיקה קוואנטית דומות להדמיית רפאים עם זוגות פוטונים הדגמת האפקט יכולה לקדם משמעותית את התחום של אופטיקה קוואנטית עם קרינת רנטגן. יש לציין, כי תכונות המתאם של זוגות פוטונים ושל גלאי קרינת רנטגן יכולים להוביל להדמיית עצמים עם מעט פוטונים, כפי שהודגים בתדרים אופטיים וכתוצאה להפחתת מנת הקרינה של קרינת רנטגן.

בחלק נוסף של עבודת המחקר של הדוקטורט אני מציג את ההדגמה הראשונה של הדמיית רפאים עם זוגות פוטונים של קרינת רנטגן. התוצאות הינן היישום הראשון של זוגות פוטונים של המרת תדר פרמטרית של קרינת רנטגן. התוצאות עושות שימוש בקשר הישיר בין אנרגיות הפוטונים לבין זוויות הפליטה שלהם ובין המתאם המנוגד בין ווקטורי הגל של פוטוני הסינגל והאיידלר כדי לדמות סדקים ללא רעש רקע. הרחבת ההליך יכולה לשמש להדגמת מגוון תופעות קוואנטיות של קרינת רנטגן.

עבודה זו נעשתה בהנחייתו של

ד"ר שרון שוורץ

המחלקה לפיסיקה

אוניברסיטת בר-אילן

הדמיה וספקטרוסקופיה לא ליניארית באמצעות קרינת רנטגן

חיבור לשם קבלת התואר "דוקטור לפילוסופיה"

מאת:

אביעד שחורי

המחלקה לפיסיקה

הוגש לסנט של אוניברסיטת בר-אילן

ניסן, תשע"ח

רמת גן